



UNIVERSITAT POLITÈCNICA
DE CATALUNYA
BARCELONATECH



Understanding Secondary Emission Processes and Beam Matter interactions for Optimization of Diagnostic Wire Grid System in Particle Accelerators

Thermal modeling for beam power limits calculation

Author:

Araceli Navarro Fernandez

Universitat Politècnica de Catalunya

Doctorat en enginyeria nuclear i de les radiacions ionitzants

Supervisors:

Federico Roncarolo
Francisco Calvino

CERN
UPC



Abstract

Thin targets, in form of foils, stripes or wires, are widely used in beam instrumentation to measure various beam parameters, such as intensity, position and size. All these monitors can differ in geometry and material. Depending on beam parameters such as intensity, energy, transverse and longitudinal size, the detector can suffer thermomechanical stresses. This can potentially perturb the measurement accuracy and degrade the integrity of the detector. The core of this contribution presents the development of a finite-difference model, developed to simulate the particle-detector interactions and predict the detector material heating and damage.

This work has been mainly performed in the context of LINAC4, which is the first accelerator at CERN's accelerator chain. Some other facilities (CERN PS Booster, CERN SPS, GSI facility) will also be mentioned in this document. However, the majority of the studies and conclusions will refer to the energy range (45 keV - 160 MeV) and detector types available at LINAC4 (SEM grids and wire scanners).

To understand the purpose, functionality and limitation of thin target detectors, this document introduces the basic principles of transverse beam dynamics and beam matter interactions, focusing on processes such as: energy deposition, secondary electron emission (SEE), electron backscattering, etc. The thermal model implemented during this work (PyTT) to simulate the thermal evolution of thin target detectors is presented and detailed discussed. To assess the reliability of the simulated results, an experiment performed at LINAC4 is presented. This experiment heavily relied on the theory of thermionic emission to indirectly measure the temperature of the detectors during operation.

The performance of the simulation tool is discussed, in terms of results sensitivity to parameter uncertainty. Uncertainties in material parameters, such as the emissivity, yield uncertainties in simulation results. To improve our knowledge of the emissivity values of thin tungsten wires, an experimental setup, based on the calorimetric method, was implemented for this work. The experimental setup, emissivity calculation and results are detailed described.

Some examples of how this work has been useful for CERN operations, and other facilities (like GSI) are presented in these pages. This include, beam power limit calculations for the CERN Linac4 and SPS diagnostics, beam intensity and profile measurements at LINAC4, thin foil detector calibration (H0H- Monitors), SEM grid prototype testing at GSI, etc.

Acknowledgements

If this thesis becomes a reality is because of the kind support and help from many people. I would like to extend my sincere gratitude to all of them.

There are no proper words to convey my deep gratitude and respect for my thesis and research advisor, Dr. Federico Roncarolo. I thank him for giving me the opportunity to do this Ph.D., for his continuous support, for his patience, motivation, and his invaluable advice. I would like to express my sincere gratitude to Prof. Francisco Calvino, who since the moment I appeared in his office many years ago, has provided me with guidance, challenging projects and learning opportunities.

I am also thankful to all the people that collaborated in the realization of this project. First, I would like to thank Dr. Mariusz Sapinski. This work would not have been possible without his previous studies and knowledge. I thank him for being always willing and enthusiastic to assist in any way he could throughout the research project. Thank you to Miguel Martin, a colleague and good friend, without whom I would (genuinely) not have been able to perform the emittance measurements. His incredible technical skills, his kindness, and his well-timed jokes made the working process so much more entertaining.

I would like to thank the ABT group, Chiara Bracco and Elisabeth Renner, for their patience and assistance during the long calibration measurements. I would also like to thank the beam instrumentation team at GSI, as well as the members of the PROACTIVE company, for giving me the opportunity to join them in their measurements campaign. Specially, I would like to thank Peter Forck, for all his help, insightful comments.

I would like to thank the rest of the members of my thesis committee: Guillem Cortes, Alfredo de Blas and Ivan Podadera for helping me in completing this project. Special thanks go to, Dr. Ariel Tarifeno. Who has been a huge influence and without whom I would have never been the scientist I am today.

I would like to thank all the members of the PM section at CERN. I have learned so much from all of you. All those precious moments in corridors, lunchtimes, and various coffee breaks have meant more to me than you know. A special thank you goes to my amazing officemates, Daniele Butti and Luana Parsons, for all those very welcomed distractions. And to my great friends, M. Checchetto, M. Pagin and Jose Carlos, I am not going to say anything, you guys know why your name is here.

Lastly, I guess I could not finish without a chiche thank you to my mother. M'agradaria donar-te les gràcies per tot el teu suport, el teu carinyo, i l'amor que mas donat sempre. M'agradaria agrair-te tots els teus esforços, tot el que has sacrificat per mi. Sé que no ha sigut fàcil, però jo sempre he sigut molt feliç i si he arribat fins aquí es graciés tu. Intento dir-t'ho tant com puc, però t'ho torno a dir, i ara per escrit i tot. Moltes gràcies mare!

Contents

Abstract	3
Acknowledgements	5
Contents	9
List of Figures	16
Overview	17
1 Introduction	21
1.1 CERN accelerators complex	21
1.1.1 Linear Accelerator 4 (LINAC4)	22
1.2 Accelerator Physics Principles	24
1.2.1 Principles of beam dynamics	24
1.2.2 Particle beams and beam profile	25
1.2.3 Transverse phase space	26
1.2.4 Transverse beam emittance	27
1.2.5 Phase Space Evolution	28
1.3 Beam Diagnostics	29
1.3.1 Secondary Emission Grids (SEM Grids)	29
1.3.2 Wire Scanners	31
1.3.3 Beam Current Transformer (BCT)	32
1.3.4 Faraday Cup (FC)	32
2 Particle Interactions with Matter	35
2.0.1 The Bethe Bloch Formula	35
2.0.2 Energy Loss in Mixtures and Compounds.	37
2.0.3 Electrons Energy Loss	37
2.0.4 Multiple scattering and Backscattering	38
2.0.5 Path Length and Range	39
2.0.6 Types of Absorbers	40
2.1 Secondary Electron Theory	40
2.1.1 Delta Rays	43
3 Secondary Emission Monitors Signal Modeling	45
3.1 Signal Generation in SEM	45
3.1.1 Charge Deposition (Q_{dep})	45
3.1.2 Secondary Emission Charge (Q_{SE})	45

3.1.3	Thermionic Emission Charge (Q_{Th})	46
3.2	Signal Generation Studies at LINAC4.	47
3.3	Beam Intensity and Profile Measurements.	49
4	Thermal Modeling of Thin Target Detectors.	53
4.1	Introduction and Motivation	53
4.2	The heat equation	54
4.2.1	Target Heating (Ht)	54
4.2.2	Radiative Cooling (Rd)	55
4.2.3	Conduction Cooling (Cd)	55
4.2.4	Thermionic Cooling (Th)	56
4.2.5	Sublimation Cooling (Sub)	56
4.3	Numerical Approximation to the heat equation.	57
4.3.1	Finite Differences Schemes	58
4.3.2	Initial and Boundary Conditions	61
4.3.3	The Non-Linear Problem	62
4.4	The two-dimensional problem	62
4.5	Importance of Cooling Effects	63
4.6	PyTT	64
4.7	Model uncertainties	65
4.7.1	Beam Parameter Uncertainties	65
4.7.2	Material Parameter Uncertainties.	67
5	Simulation Benchmarking and Applications	69
5.1	Thermionic Measurements at LINAC4	69
5.1.1	Experimental setup and preparation	69
5.1.2	Experimental Results	72
5.1.3	Measurment-Simulation Comparison	73
5.2	Simulation Comparison: Ansys	75
5.2.1	Thin Wire Studies	76
5.2.2	Thin Foil Studies	78
5.3	Beam Power Limit Calculations	79
5.3.1	SEM grid and Slow Wire Stanner at Linac4	79
5.3.2	Fast Wire Scanners at SPS	81
6	Thin Wire Emissivity Measurements	85
6.1	Motivation	85
6.2	Essentials in radiometry	86
6.3	Emissivity Measurement Methods	88
6.4	Calorimetric Method	88
6.5	Temperature Measurement	89
6.6	Numerical Calculation of the Emissivity	90
6.7	Experimental Set Up	92
6.7.1	Acquisition system	92
6.8	Acquisition System Calibration	94
6.9	Experimental Results	95
6.9.1	Steady State Determination and Resistance Measurements	96
6.9.2	Intensity Temperature Curves	98
6.9.3	Boundary Condition Measurements	99

6.9.4	Wire Emissivity	100
6.9.5	Convection Effects	102
7	H0H- Monitor Calibration and Comissioning	105
7.1	CEI to CERN PS Booster	105
7.2	H^0H^- Beam Current Monitors and Dump	107
7.2.1	Expected signal generation	108
7.3	Monitor Electronics, Layout and functionalities	109
7.3.1	Signal Monitoring Circuit	109
7.4	Interlock Circuit	110
7.5	Read Out Signals	111
7.5.1	OASIS signal	111
7.5.2	Plate Signal	112
7.5.3	Interlock Signal	112
7.6	Calibration	113
7.6.1	Objective and Procedure	113
7.6.2	Correction Factor	115
7.6.3	Results	118
7.7	Stripping Inefficiency Calculations	122
7.8	Noise Problems	124
8	SEM Grid Testing at GSI	127
8.1	The FAIR project and UNILAC	127
8.2	Motivation and Experimental Conditions	128
8.3	Experimental Results	130
8.3.1	Bias Voltage Studies	130
8.3.2	Profile Measurement and Time Studies	132
8.3.3	Thermal Studies	135
	Conclusions	141

List of Figures

1.1	CERN Accelerator Complex [3].	21
1.2	LINAC4 accelerating components layout.	23
1.3	LINAC4 Pulse Structure	23
1.4	Frenet-Serret coordinate system.	24
1.5	Example of Particle distribution in the X-Y space, with their corresponding projections.	26
1.6	Particle distribution in the transverse phase space.	26
1.7	Phase Space, geometrical ellipse.	27
1.8	Example of phase space evolution.	28
1.9	Example of a SEM grid installed at CERN accelerator Complex.	30
1.10	Schematic representation of SEM Grid Acquisition system.	30
1.11	Rotational Fast Wire Scanner, used at CERN SPS.	31
1.12	Schema of a current transformer built as a ring-core (torus).	32
1.13	Schematic Representation of Faraday Cup.	33
2.1	Stopping power of protons in thin foils of different materials, as a function of incident particle energy. From [26].	36
2.2	Stopping power of electrons in a thin tungsten foil, as a function of incident particle energy. From [26].	37
2.3	Left: Schematic representation of multiple coulomb scattering. Right: Schematic representation of electron backscattering.	38
2.4	Schematic diagram of charged particle penetration into absorbing medium. Left: Heavy charged particle. Right: Light Charged particle.	39
2.5	Bragg peak of 3 MeV protons in Graphite.	41
2.6	Ion induced secondary electron spectra for a variety of metals. Incident ion: Proton 500 keV. From [40].	42
3.1	Schematic representation of the processes inducing current in the detector material.	46
3.2	Range of particles as a function of incident ion energy.	47
3.3	Secondary Emission Yield as a function of incident proton energy.	48
3.4	Expected transverse beam profile for incident H^- particles. Left: 3 (MeV), Right: 160 (MeV). For these simulations, a 25 mA, 100 μs particle beam was considered.	49
3.5	Schematic representation of Linac4 and the profile monitor locations.	49
3.6	The LOF caption	50
3.7	Average intensity measured by the different BCTs at LINAC4. Transmission along the LBE line.	50

3.8	Horizontal transversal beam profile measured by the different detectors at LINAC4	51
3.9	Vertical transverse profile measured by the second SEM grid and second wire scanner of the L4T line at Linac4.	52
4.1	Carbon fiber wire scanner used at SPS in 2008.	53
4.2	SEM Grid used at Linac4, in L4T Line.	54
4.3	Space discretization of a homogeneous body.	58
4.4	Time discretization of the material rod.	58
4.5	Stencil for the Forward Time, Central Space finite difference method.	59
4.6	Stencil for the Backwards in time, Central in space finite difference method.	61
4.7	Stencil for the Crank-Nicolson finite difference method.	61
4.8	Relative importance of the different cooling mechanisms as a function of the temperature.	63
4.9	Graphical User-Friendly interface of PyTT code.	64
4.10	Example of output visualization GUI.	65
4.11	Effects of beam parameter uncertainties on maximum temperature simulation results.	66
4.12	Effects of material property uncertainties on maximum temperature results.	67
4.13	Material property uncertainties for Graphite and Tungsten.	68
5.1	Thermionic current as a function of the temperature for Tungsten ($40\mu m$) and a Graphite ($33\mu m$) wires.	70
5.2	Schematic representation of Linac4 layout, with locations of the SEM Grid (L4T.BSGH/V.0243) and the BCT (L4T.BCT.0107) used for thermionic measurements.	70
5.3	Schematic representation of wire position at L4T.BSGH/V.0243, as they are mounted on the ceramic support.	71
5.4	Summary of expected maximum current for different beam conditions. Gray Area indicates where thermionic emission is detectable. The beam size is given in (mm) and Beam intensity in (mA).	71
5.5	Evolution of the transverse beam profile along the beam pulse. Top: example of transverse beam profile measurement. Bottom: Calculated beam size from gaussian approximation. Error bars were calculated by measuring different beam pulses.	73
5.6	Evolution of the measured current in different wires as a function of time, for six consecutive beam pulses.	74
5.7	Current registered by several wires during the beam pulse. The units of the signals are (ADC counts).	74
5.8	Example of vertical profile beam measurement. Darker colors indicate measurements at the beginning of the beam shot. Lighter colors indicate measurements at the end of the shot.	75
5.9	Signal generated in the wire intercepting the beam as a function of time. Compared with simulated intensity results.	76
5.10	Examples of the heat flux provided to Ansys and PyTT for three different simulation cases.	77

5.11	Comparison of the evolution of the maximum temperature in the detector as a function of time, for three different beam pulse lengths.	78
5.12	Comparison of the evolution of the maximum temperature in $40\mu m$ graphite foil, as a function of beam pulse length. On the right axis, the relative error between them is represented.	78
5.13	Comparison of the cooling rate between PyTT code and Ansys. For a $40\mu m$ graphite foil after a beam shot.	79
5.14	Comparison between thermal distribution in Graphite foil after one beam shot. In Ansys (top) and PyTT code (bottom). The black lines in Ansys have a separation of 1 mm.	80
5.15	Power limit calculations for a detector at L4C (Left) and a detector at L4T (right) lines. The beam size in both cases was $\sigma_x = \sigma_y = 2.0$ mm.	81
5.16	Power limit calculations for a detector at 160 MeV beam energies.	82
5.17	Comparison of maximum fast wire scanner temperatures reached for different beam conditions. Left: Injection energy. Right: Extraction energy.	82
6.1	Examples of total emissivity measurements for Gold and Tungsten. From [61]	85
6.2	Black body spectrum for different temperatures. Blue line, Wien's displacement law.	87
6.3	Schematic representation of emissivities definitions. Left: Directional Emissivity. Right: Directional emissivity.	88
6.4	Evolution of the $R(T)/R(T_0)$ as a function of the temperature for a tungsten wire. From [74]	90
6.5	Picture of the experimental setup for emissivity measurements.	92
6.6	Schematic representation of the electronics set up.	93
6.7	3D design of the Measuring board.	93
6.8	3D design of the acquisition board.	94
6.9	Calibration curves for the different amplification ranges. Left: Intensity Calibration. Right: Voltage Calibration. The explicit expression of the fitted curves (dashed lines) is provided in the text.	95
6.10	Raw data measurements (before calibration) for a $40\mu m$ gold-coated tungsten wire. Intensity, voltage and resistance as a function of time for an applied current of 50 mA (left) and 190 mA (right). The mean values of the different quantities were calculated in the gray area.	96
6.11	Summary of the measured intensity (left), voltage (center) and resistance(right), on the steady state, for the different samples as a function of the applied intensity.	97
6.12	Calculation of R_0 for a $40\mu m$ Tungsten wire. Only the first 8 points were considered for the fitting.	98
6.13	For the different types of wires, average temperature as a function of the intensity going through the wires.	99
6.14	Measurement of T_{right}, T_{left} as a function of time for different applied currents. The red crosses indicate the point when intensity sopped is being provided to the wire.	99

6.15	Summary of boundary equilibrium temperatures (T_{left} , T_{right}) measured by the thermo-couples at the extremes of the wire for different applied currents	100
6.16	Steady state temperature profile calculated for different intensities.	101
6.17	Measured emissivity for 40 μm tungsten wires as a function of the temperature.	101
6.18	Comparison between measurements taken in and out of vacuum conditions. Left: 10 μm wire diameter. Right: 40 μm wire diameter.	102
6.19	Tungsten wire after the measurements. Clear change of color is appreciated.	102
7.1	Schematic representation of the PSB injection line, featuring the DVTs, DIST and SMV vertical separation scheme.	106
7.2	Possible Linac4 pulse structures and BI.DIS timing. Left: Standard operation with 65 - 100 μs injected turns per ring. Center: Operation with 0 turns injected in ring 3. Right: 3-5 injected turns per ring.	106
7.3	Schematic representation of PSB H^- Charge Exchange Injection system.	107
7.4	Mechanical design of the H^0H^- current monitors (red) and Titanium dump (black).	107
7.5	Integration of the H^0H^- dump (black) and intensity monitor (red plates) in a PSB ring. The purple element is the BSW4 magnet.	108
7.6	Schematic diagram of the signal monitoring electronics.	110
7.7	Time logic of signal monitoring circuit.	110
7.8	Schematic diagram of the electronic circuits for the interlock system.	111
7.9	Example of OASIS signals. Left: Single turn, pulse length 200 ns, focused on H0L plate. Right: 10 turns, pulse length 620 ns, focused on HML plate.	111
7.10	Example of Plate signals for different beam conditions.	112
7.11	Several examples of interlock signals.	113
7.12	Schematic representation of the BCT (in yellow) location on the beam line.	113
7.13	Schema of the order followed during the measurements.	114
7.14	Example of measurement taken during a scan in Ring 2. Shaded area, integration window for the total charge calculation.	114
7.15	Example of background correction. Left: Before correction. Right: After correction	115
7.16	Example of beam displacement effect, for a 4 turn, 200 ns beam.	116
7.17	Example of BCT measurements, number of charges with time.	117
7.18	OSIS (left) and Plate signal (right) for a measurement particle beam centered in HML plate. Non-negligible head/tail effects.	117
7.19	Number of charges measured by BCTs during the plate signal calibration. For 1 injected beam turn and 200 ns beam pulse. Different colors indicate the different plates the beam was focused on.	118
7.20	Number of charges measured by the BCT during Ring1 calibration. Left: for 1 injected beam turn, different beam pulse lengths. Right: For a 200 ns beam pulse length, a different number of turns was injected.	119

7.21	Comparison of calibration factors calculated for different beam conditions. Left: for 1 injected beam turn, different beam pulse lengths. Right: For a 200 ns beam pulse length, a different number of turns was injected.	120
7.22	Comparison calibration factor with and without BSW4 magnetic field.	121
7.23	Summary of the calibration factor measurements.	121
7.24	Calculated stripping inefficiency during striping foil tests.	122
7.25	Stripping foil pictures during degradation studies.	123
7.26	Histogram representation of the calculated stripping inefficiencies during stripping foil tests.	123
7.27	Plate signals measured during normal operating conditions. Left: With beam injection. Right: No beam injection.	124
7.28	Effects of KSW and Distributor in electrical noise signals. Background measurements, no beam. Left: KSW on, Distributor On. Center: KSW off, Distributor Off in the current ring but on in other rings. Right: KSW off, Distributor Off in all rings.	124
7.29	Picture of the ferrites installation for noise mitigation before H^0H^- VEME card.	125
7.30	Effects of the ferrite installation on the H^0H^- signals.	125
8.1	Layout of the GSI + FAIR accelerator facility.	127
8.2	Schematic representation of UNILAC accelerator.	128
8.3	SEM grid by PROACTIVE R&D.	129
8.4	Intensity as a function of time, measured by the BCT, during one beam pulse. For two different beam conditions, 40 μs (left) and 150 μs (right).	130
8.5	Integral of the signal registered by the SEM grids as a function of the applied bias voltage. Top figures: Gold-Coated Tungsten Wires. Bottom Figures: SEM grid with pure tungsten wires.	131
8.6	Effect of Bias voltage on transverse beam profile measurements. Both profiles were measured with Grid2. Left: $\Delta t = 200 \mu s$, $I = 45 \mu A$. Right: $\Delta t = 100 \mu s$, $I = 100 \mu A$	132
8.7	Comparison of transverse beam profile measured by GSI grid and PROACTIVE Grid. In both cases, $\Delta t = 100 \mu s$ and $I = 100 \mu A$. A bias voltage of 40 V was applied to the PROACTIVE grids.	133
8.8	Time dependent transverse beam profile. Each time slice has a record of 5 μs . The beam pulse length and intensity were $\Delta t = 100 \mu s$	133
8.9	Integral of the total number of counts measured by all the grid wires as a function of time. For three different beam conditions. Measured with Grid1, bias voltage 100 V.	134
8.10	Top: Transverse beam profile at different instants of time. Each color represents a time slice. Each time slice has a record of 5 μs . In red the total integral of the counts along the time is represented. Bottom: Vertical beam size as a function of time. Calculated by gaussian approximation of the beam to each time slice. In red, σ_y of the beam is calculated in the integral beam profile.	134
8.11	Beam profile measured with GSI SEM grid with, Gaussian fit for beam size determination.	136

8.12	Left Plots: Evolution of the maximum temperature reached by a gold-coated tungsten wire for 5 beam shots. Right: Maximum temperature reached for different beam intensities.	136
8.13	Signal measured by the different wires as a function of time. For four different beam intensities.	137
8.14	BeamProfile measured with GSI SEM grid for the second study with Gaussian fit for beam size determination.	138
8.15	Left Plots: Evolution of the maximum temperature reached by a pure tungsten wire for 5 beam shots. Right: Maximum temperature reached for different beam intensities.	138
8.16	Fancy beam profile as time measurement for study 2	139
8.17	Current registered by the different wires in the pure tungsten grid as a function of time. For two different beam pulse lengths.	139

Overview

This document has been divided into seven chapters, each one of them trying to cover a distinct topic. This overview is designed to give an insight into the layout of this work and briefly describe the contents of each chapter.

Chapter 1 introduces the context of this work. Given that the majority of the studies presented in this thesis took place at CERN, this first chapter describes with some detail CERN accelerator's chain (Section 1.1). Paying special attention to LINAC4 (Section 1.1.1). Some basic concepts about accelerator physics are also introduced (Section 1.2). Specifically, the concepts of transverse beam physics and transverse beam profiles. The second part of the chapter (Section 1.3) moves onto beam instrumentation used to measure the previously described concepts. Beam Instrumentation is a very broad topic, so only the detectors relevant to this work are described. Those being, SEM grids (Subsection 1.3.1), Wire Scanners (Subsection 1.3.2), Beam Current Transformers (Subsection 1.3.3) and Faraday cups (Subsection 1.3.4).

Chapter 2 introduces the basics of beam matter interactions and current generation in thin target detectors. This chapter does not attempt to provide a thorough, in-depth description of this challenging topic. Its goal is to introduce all the physical topics mentioned in this thesis. Numerous references are given along those pages to allow the reader to delve much deeper into the subject if desired. The first part of the chapter focuses on how charged particles interact with matter (Section ??). The main concepts introduced are: Energy Loss (Subsection 2.0.1), Multiple scattering and backscattering (Subsection 2.0.4), Path and Range (Subsection 2.0.5). Afterward, the concept of Secondary Electron Emission (SEE) is introduced (Section 2.1).

Chapter 3) uses all the concepts explained in the previous chapter to present a semi-empirical model used to describe the signal generation in thin target detectors with applications in beam particle accelerators. This model has been extensively used to predict and interpret the signal generated in various detectors, to showcase its applicability an example of signal generation studies at Linac4 is presented (Section 3.2). The final part of the chapter presents the results obtained in the first profile and current measurements for the LBE run (Section 3.3).

The core part of this thesis consisted of the implementation of a program able to simulate the thermal evolution of thin target detectors for applications in particle accelerators, this program has been called PyTT. Chapter 4 starts with a small explanation about why is it important to implement such a simulation tool (Section 4.1). Simulating the thermal evolution implies solving the heat equation (Section 4.2). In our case the terms that have been considered are: Beam Heating (Section 4.2.1), Radiative Cooling (Section 4.2.2), Conduction Cooling (Section 4.2.3), Thermionic Cooling (Section 4.2.4) and Sublimation Cooling (Section 4.2.5). All

these terms are explained in detail in the chapter. The heat equation has to be solved numerically. In this chapter, the numerical tools employed to solve such an equation are also briefly discussed (Section 4.3). A graphical user interface was implemented to facilitate the usage of this code. This GUI is briefly discussed and presented in Section 4.6. The performance of the simulation tool is then discussed, in terms of results sensitivity to parameter uncertainties (Section 4.7)

There are two very distinct sections in Chapter 5. Two examples of benchmarking the PyTT program are provided in the first section of the chapter. In Section 5.1 an experiment performed in LINAC4 is described. The goal of the experiment was to compare the simulations of SEM grid detector results with experimental measurements. Here we present the whole experimental process: experimental planning obtained data and simulations-measurement comparison. In Section 5.2 thermal simulation results obtained with the PyTT code are compared to results obtained with ANSYS, a commercially available software, commonly used and highly trusted for thermo-mechanical studies.

The second part of Chapter 5 aims to show how the PyTT code has been used at CERN. For that, two application examples are shown. Those are: Beam power limit calculations, in terms of beam intensity, pulse length and beam size, at LINAC4 (Section 5.3.1). Beam power limit calculations, in terms of beam size, charges per pulse and wire speed, for fast wire scanners at the SPS (Section 5.3.2)

When reaching chapter 6 hopefully it will be clear that uncertainties in material parameters, such as the emissivity of the material, yield big uncertainties in the simulated thermal results. Chapter 6 describes an experiment, based on the calorimetric method (Section 6.4), to measure the emissivity of thin tungsten wires. The experimental set-up was designed and implemented from scratch explicitly for this work, and it is described in Section 6.7. In this chapter, the intermediate steps necessary to obtain the final value of the emissivity are presented. These include: Calibration of the electronics (Section 6.8), Temperature Measurements (Section 6.9.2), Boundary condition measurements (Section 6.9.3). The chapter closes with the results of the emissivity measurements for the tungsten wires used at CERN LINAC4 (Section 6.9.4).

Chapter 7 is slightly different from the other chapters of the thesis, and it could almost be taken separately. This chapter describes the calibration of the H^0H^- current monitors. These detectors have as an objective to measure the stripping inefficiency of the newly installed CEI system in the PS Booster. Section 7.1 introduces the concept of CEI and focuses on the injection of LINAC4 into the PS Booster. The H^0H^- current monitors are then introduced (Section 7.2).

To fully grasp the complexity of the data analysis performed for the calibration of the detectors, a brief description of the electronics is provided (Section 7.3). The various signals to analyze are also described (Section 7.5). This is then followed by a detailed description of the process followed for the calibration (Section 7.6), it presents the final results of the calibration of the detectors (Section 7.6.3) and some dependencies are discussed (Section 7.6.3). After the calibration these detectors have been extensively used. Section 7.7 shows an example of measurements taken with these detectors after the calibration. Finally, this chapter finishes presenting some of the current challenges faced by the H^0H^- monitors (Section 7.8).

Chapter 8 presents the results obtained during an experimental campaign at GSI. During these experiments, two SEM grid prototypes, designed and manufactured

by PROACTIVE, were tested. In this chapter, a description of the GSI facility is given (Section 8.1). This is followed by a summary of the motivations and the experimental conditions in which the Grids were tested (Section 8.2). The results of the experiment are divided in three separate sections. First the dependency of the measured current with the applied voltage is presented (Section 8.3.1). This is followed by a study on the transverse beam profile measurements and its time dependency (Section 8.3.2). In parallel to the measurement thermal simulations were done with the PyTT code, predicting the wire temperature at various experimental conditions. The comparison between these predictions and the measured results is presented in Section 8.3.3.

The conclusions succinctly summarize the results obtained in this document and discuss the relevance and impact this study had on the field.

Chapter 1

Introduction

1.1 CERN accelerators complex

The European Organization for Nuclear Research (CERN) was founded in 1954, and it has become the largest particle physics laboratory in the world [1]. It sits astride the Franco-Swiss border near Geneva. It was one of Europe's first joint ventures and now has 23 member states. At CERN, the world's largest and most complex scientific instruments are used to study the basic constituents of matter. However, the physics program at the laboratory is much broader, ranging from nuclear to high-energy physics, from studies of antimatter to the possible effects of cosmic rays on clouds [2]. CERN has also pushed the frontiers of technology with inventions such as the World Wide Web (www), Proton Emission Tomography (PET), etc.

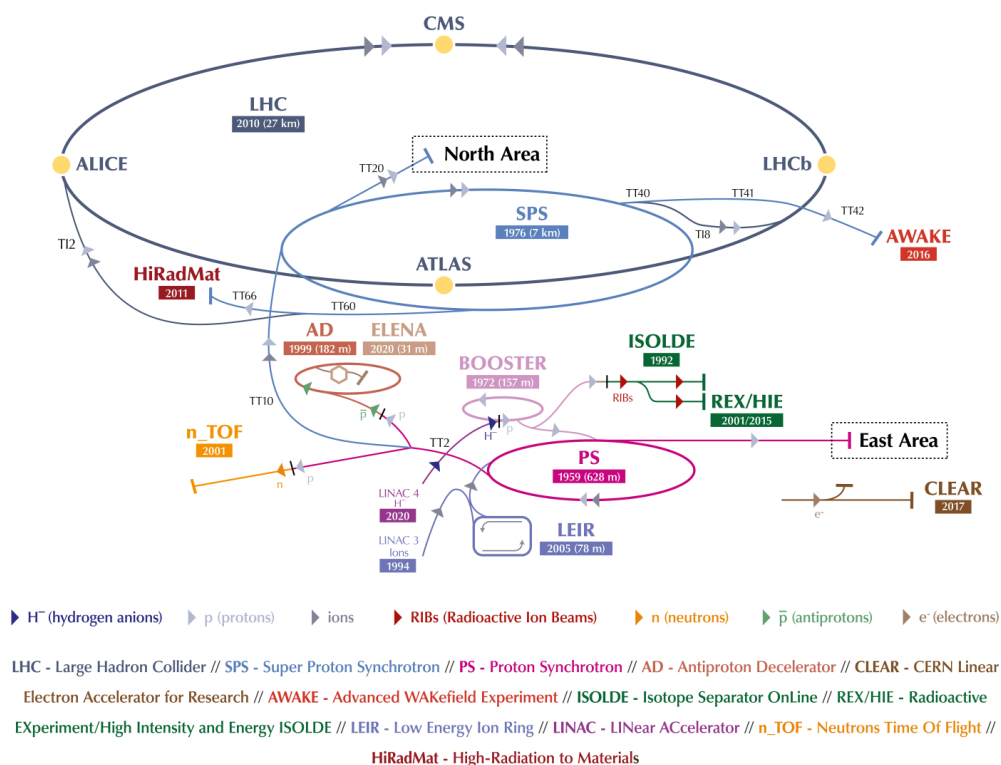


Figure 1.1: CERN Accelerator Complex [3].

CERN's accelerator complex (See 1.1) consists of many different types of linear and circular accelerators and interconnecting transfer lines to gradually accelerate the particles before injection into the Large Hadron Collider (LHC).

Since 2020, Linear accelerator 4 (Linac4) became the source of proton beams for the LHC. Linac4 is an 86 m long machine. It accelerates negative hydrogen ions up to 160 MeV. The ions are then stripped of their two electrons during injection from Linac4 into the Proton Synchrotron Booster (PS Booster or PSB) to leave only protons. The PS Booster is made up of four superimposed synchrotron rings, with an 157 m circumference, which accelerates the injected protons up to 2 GeV for injection into the Proton Synchrotron (PS).

Currently, the PS is the oldest accelerator in the chain, with a circumference of 628 meters, operating up to 26 GeV. The Super Proton Synchrotron (SPS) is the second largest machine in the complex, measuring nearly 7 km in circumference. It takes the particles from the Proton Synchrotron and accelerates them up to 450 GeV. The CERN accelerator complex culminates with the Large Hadron Collider. The LHC consists of a 27 km ring of superconducting magnets, which guide two high-energy particle beam, traveling in opposite directions, in separate beam pipes. The beams collide at four locations around the accelerator ring, corresponding to the positions of four particle detectors ATLAS, CMS, ALICE and LHCb. The High Luminosity Large Hadron Collider (HiLumi LHC) project aims to deliver proton-proton collisions at 14 TeV.

The CERN accelerator complex is not limited to accelerating proton. Linear accelerator 3 (Linac 3) is the starting point for the ions. It usually provides lead ions, but also argon and xenon were used in the past. Experiments with oxygen are planned for the future. The long pulses of lead ions from Linac 3 are transformed into short, dense bunches by the Low Energy Ion Ring (LEIR) before they are injected into the PS.

The injector chain, apart from feeding the LHC, is also used to deliver particles to several other experiments carried out at CERN, including Antimatter research at the Antiproton Decelerator (AD) and Extra Low ENergy Antiproton (ELENA), radioactive ion beam research on ISOLDE, research on neutron-nucleus interactions at the n-TOF facility, research on radiation-induced damage on materials in the HiRadMat facility and even studies on the use of proton-driven plasma wake-fields in AWAKE.

1.1.1 Linear Accelerator 4 (LINAC4)

As part of the LHC injection upgrade (LIU), LINAC4 was introduced to substitute LINAC2 [4]. The main goal for the construction of LINAC4 was to increase the beam brightness. This increase is achieved by combining two effects: Firstly, the increase of the top energy to 60 MeV (compared to the 50 MeV given by LINAC2), which reduces significantly the space charge effect, causing emittance-blow up in the PSB; Secondly, the use of H^- ions instead of protons makes it possible to inject into the PSB via the charge exchange injection scheme (explained in detail in Ch. 7). During the long shutdown (2019-2020), LINAC4 finally replaced LINAC2 as the source of protons for the LHC.

Fig. 1.2 shows a description of the accelerating sequence of LINAC4. This sequence is quite standard for a pulsed LINAC design. The LINAC4 source is a

cesiated molybdenum-surface radio-frequency plasma ion source [5]. This source can produce H^- ion beams of up to 400 μs pulse length, 40 mA, at a maximum repetition frequency of 0.8 Hz

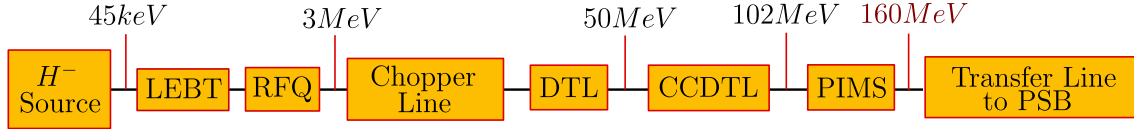


Figure 1.2: LINAC4 accelerating components layout.

The Low Energy Beam Transport (LEBT) line provides the beam matching from the source to the RFQ (Radio Frequency Quadrupoles) and contains the diagnostics to monitor the source. The three-meter RFQ performs the beam capture and bunching and accelerates the particles to an energy of 3 MeV. It is followed by a Medium Energy Beam Transport (MEBT) or "Chopper Line". This system consists of an electrostatic beam deflector followed by a beam dump. The purpose of this line is to avoid losses at higher energies when the induced radiation is higher.

This system serves three purposes. Firstly, losses due to instable LINAC4 pulses. Secondly, it can be used to clean the first few tens of μs of the beam pulse which is generally not stable. Finally, its purpose is to create "holes" in the beam pulse, timed with the rise-time of the PSB distributor, which switches the incoming LINAC4 beam between the four PSB Rings.

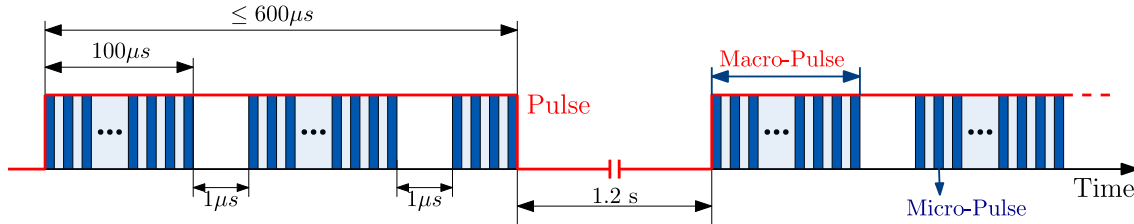


Figure 1.3: LINAC4 Pulse Structure

The chopping line is followed by a series of three accelerating structures. The Drift Tube Linac (DTL) is divided into three tanks and accelerates the beam up to 50 MeV. The Cell-Coupled Drift Tube Linac (CCDTL) is made of 7 accelerating modules for top energy of 102 MeV. Finally, the Pi-Mode Structure (PIMS) brings the energy of the beam to the desired 160 MeV. More information about LINAC4 and its component parts can be found in [6].

In the current operational conditions, the LINAC4 pulse structure, shown in Fig. 1.3, consists of four individual macro pulses, typically 20 - 100 μs long (depending on the required number of injected turns per ring) and separated by a 1 μs particle-free gap. Each macro-pulse consists of a train of ps long micro-bunches that are spaced by intervals of 2.8 ns [7]. To minimize losses at injection, every 1 μs (i.e. 1 PSB turn) of such a train is filled with micro-bunches for 650 ns and is empty for the remaining 350 ns.

1.2 Accelerator Physics Principles

The topic of Accelerator physics is very broad, in this section only an overview of the topics of interest for this document will be introduced. These topics include a quick overview of the basic concepts of beam dynamics, transverse plane, beam size and emittance. For a much more complete introduction to the world of accelerators check [8].

1.2.1 Principles of beam dynamics

To describe the movement of the particles in an accelerator, the Frenet-Serret coordinate system, shown in Fig. 1.4, is commonly used. S defines the longitudinal coordinate and it is always tangent to the reference path. X and Y define the transverse plane (orthogonal to the particle trajectory). $x(s)$ and $y(s)$ describe the particle's deviation from the reference path and $\rho(s)$ commonly defines the curvature of the reference orbit at each point.

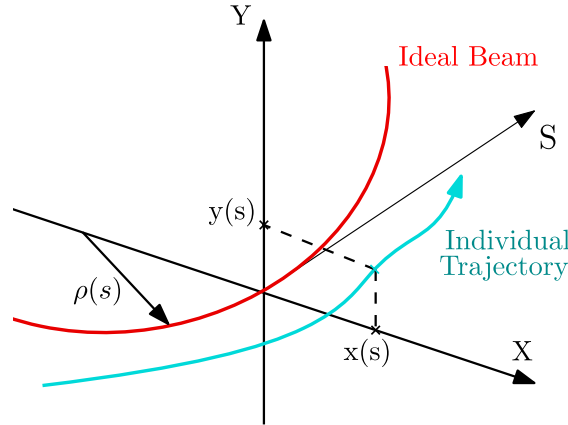


Figure 1.4: Frenet-Serret coordinate system.

The scope of a particle accelerator design is to guide the beam of particles along the reference path and accelerate them to the desired energy. In the simplest case, we consider constant energy and stable beam trajectory. One can guide these particles by applying electromagnetic forces to them. Lorentz's law describes the force acting on a particle of charge "q" traveling in an electromagnetic field:

$$\vec{F} = q \left(\vec{E} + \vec{v} \times \vec{B} \right) \quad (1.1)$$

Where \vec{E} and \vec{B} are the electric and magnetic fields and \vec{v} is the particle velocity. Longitudinal electric fields accelerate the particles, while transverse bending and focusing are provided by transverse magnetic fields.

Particles which at the time t_0 have a non zero transverse coordinate (x_0, y_0) and momentum (x'_0, y'_0) start to perform oscillations in the horizontal and vertical planes, called Betatron oscillations [9]. These oscillations depend on the magnetic fields in the ring. The equation of motion on the transverse space can be derived from Lorentz's equation, and after some approximations, they read [10]:

$$\begin{aligned}
x'' + \left(\frac{1}{\rho^2(s)} + \frac{1}{B\rho} \frac{\partial B_y(s)}{\partial x} \right) x &= 0 \\
y'' - \frac{1}{B\rho} \frac{\partial B_y(s)}{\partial x} y &= 0
\end{aligned} \tag{1.2}$$

The product $B\rho$ is the magnetic rigidity and is equal to the ratio of the momentum to charge p/q . The only difference between the vertical and horizontal coordinates is the term $1/\rho^2(s)$, which is related to the centripetal force in the radial direction. These types of differential equations are often referred to as Hills equations [11], and describe a pseudo harmonic oscillator in which the spring constant depends on the position (s). For each element in the beamline, one can calculate the solution of the equation of motion. This solution can be expressed in a matrix formulation [12]:

$$\begin{bmatrix} u(s) \\ u'(s) \end{bmatrix} = \begin{bmatrix} C(s) & S(s) \\ C'(s) & S'(s) \end{bmatrix} \begin{bmatrix} u_0 \\ u'_0 \end{bmatrix} = M(s) \begin{bmatrix} u_0 \\ u'_0 \end{bmatrix} \tag{1.3}$$

Where $M(s)$ is called the transformation matrix, which can be calculated individually for each type of beamline element. This matrix formalism is very useful, as one can follow a particle trajectory along a complicated beam line by repeated matrix multiplication from element to element [13].

1.2.2 Particle beams and beam profile

A beam or a bunch of particles is a collection of a very large number of particles whose center of gravity moves in a well-defined direction. If we consider the transverse plane X-Y (orthogonal to the beam direction of motion), one can obtain the particle distribution by noting the position of each particle that crosses this plane. If there is no coupling between the motion of the particles in the x and y directions, the distribution of the particles will be somehow elliptical, with the axis of the ellipse parallel to the x and y axes. See Fig. 1.5 for an example of transverse space particle distribution.

A histogram expressing the number of particles in a beam as a function of the transverse position is known as a beam profile. A Horizontal beam profile gives information about the number of particles at different x positions. A Vertical beam profile gives information about the number of particles at different y positions. A typical way of expressing the number of particles at a certain point in space is using a gaussian function:

$$N(x, y) = \frac{N_{Tot}}{2\pi\sigma_x\sigma_y} \cdot \exp \left(-\frac{1}{2} \left(\left(\frac{x-x_0}{\sigma_x} \right)^2 + \left(\frac{y-y_0}{\sigma_y} \right)^2 \right) \right) \tag{1.4}$$

Here x_0, y_0 are the coordinates of the center of the beam. σ_x, σ_y are the standard deviation of the normally distributed beam of particles. N_{Tot} refers to the total number of particles in the beam pulse. However, this expression is no more than an approximation, and one should be careful to understand its limitations. Usually, at the particle source, the beam of particles is far from Gaussian, but after some acceleration, this becomes a good approximation [8].

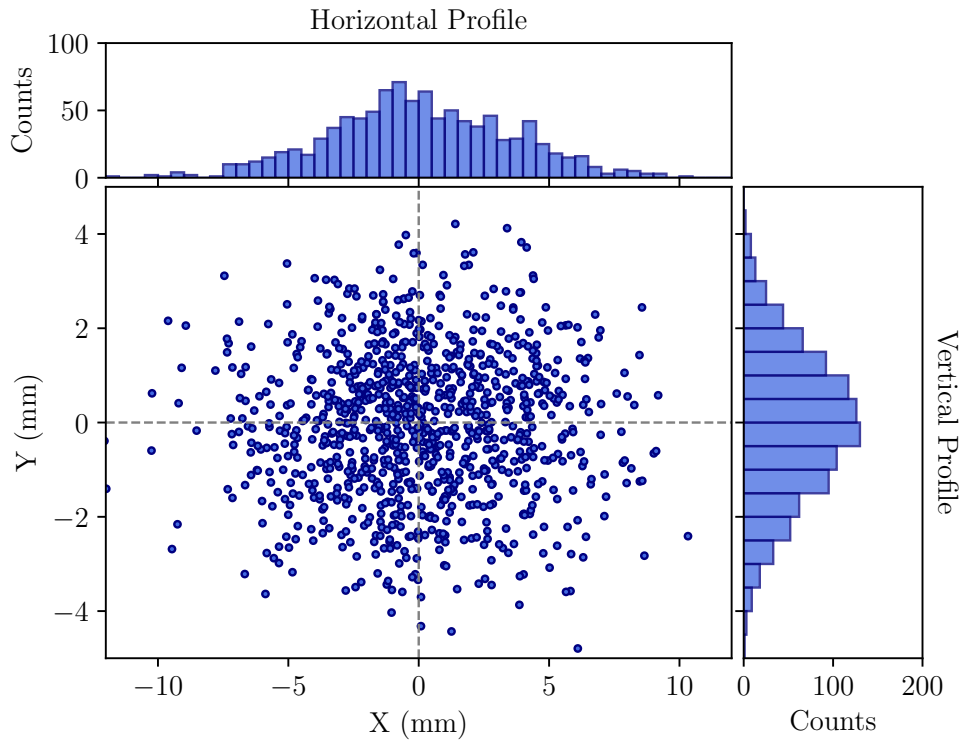


Figure 1.5: Example of Particle distribution in the X-Y space, with their corresponding projections.

1.2.3 Transverse phase space

Each one of the particles in the beam will not only have a different position, but also a different direction of movement. The velocity vector of each particle can be decomposed into two components, one parallel to the beam direction (s) and one orthogonal to it (transverse velocity). The transverse velocity can then be decomposed into its components along the x -axis and y -axis. The phase space has information on both the position and the transverse velocity of each of the particles in the beam.

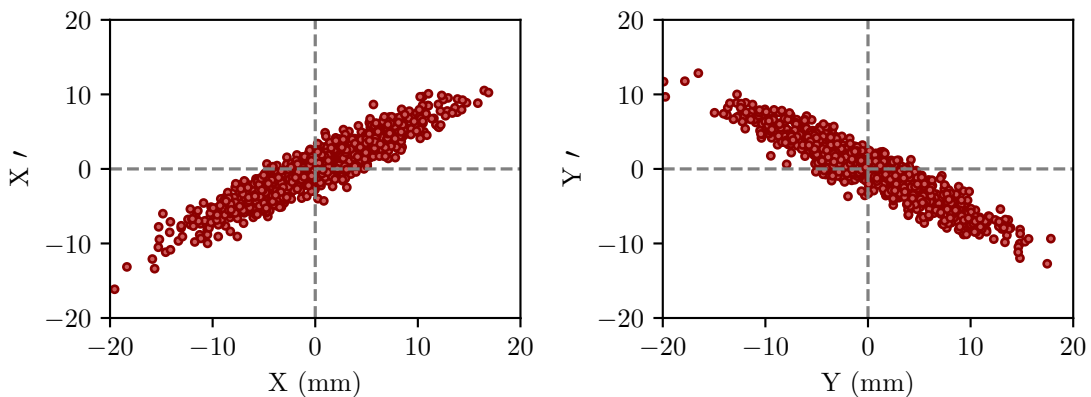


Figure 1.6: Particle distribution in the transverse phase space.

Because the velocity and the momentum of the particles are related, one can express the information of the phase space in terms of the transverse momenta of the particles (p_x, p_y) . For convenience, the phase space is described by the transverse momentum (p_x, p_y) normalized by the longitudinal momentum (p_s) . These quantities are expressed as: $x' = p_x/p_s$ and $y' = p_y/p_s$. For representing the phase space, two charts are needed, one for the vertical plane and one for the horizontal plane.

Fig. 1.6 shows an example of particle distribution in the phase space. From these figures, we can see that the distributions are ellipses, and in this case, they are tilted with respect to the axes. The phase space contains the whole description of the states of all the particles for a particular plane, and it is needed if to calculate the motion of the particles in the electromagnetic fields of the accelerator.

1.2.4 Transverse beam emittance

A formal description of the phase space can be formulated by exploiting its elliptical. The equation of the phase-space ellipse can be described as follows:

$$\epsilon = \gamma x^2 + 2\alpha x x' + \beta x'^2 \quad (1.5)$$

α, β, γ are referred to as the Courant-Snyder parameters [8]. The area of the ellipse is simply $A = \pi\epsilon$. In accelerator and beam physics language, the area in phase space (ϵ) containing the particles is called the emittance, statistical emittance, or more precisely rms-emittance. In the case of Gaussian beams, the concept of rms-emittance can be directly interpreted as the area containing a fraction (f) of ions. For example, it can be proven [9], that the curve of area ϵ should contain a 39% of particles.

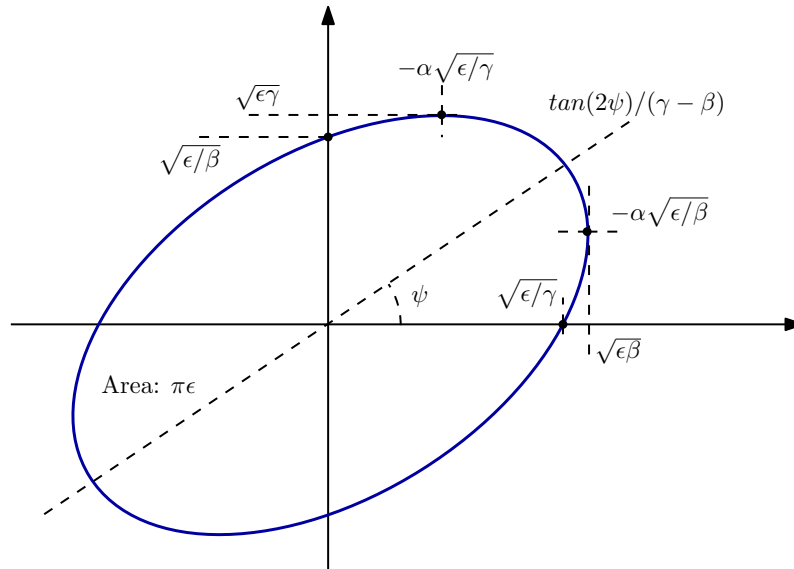


Figure 1.7: Phase Space, geometrical ellipse.

Fig. 1.7 shows a geometrical description of the Courant-Snyder parameters. These parameters (α, β, γ) are not independent, the third parameter is typically defined in terms of the other two:

$$\gamma = \frac{1 + \alpha^2}{\beta} \quad (1.6)$$

Some other quantities, also important for understanding the mathematical formulation of the transverse emittance are:

$$x_{rms}^2 = \langle x^2 \rangle = \frac{1}{N} \sum_{i=1}^N x_i^2 \quad (1.7)$$

$$x'_{rms}{}^2 = \langle x'^2 \rangle = \frac{1}{N} \sum_{i=1}^N x_i'^2 \quad (1.8)$$

$$xx'_{rms} = \langle xx' \rangle = \frac{1}{N} \sum_{i=1}^N x_i x_i' \quad (1.9)$$

With $x_i = X_i - \langle X \rangle$ and $x_i' = X_i' - \langle X' \rangle$. X_i and X_i' being the horizontal position and momentum of the individual particles forming the beam. For convenience these parameters can be expressed in a matrix form as follows:

$$\Sigma = \begin{pmatrix} \langle x^2 \rangle & \langle xx' \rangle \\ \langle xx' \rangle & \langle x'^2 \rangle \end{pmatrix} = \epsilon \begin{pmatrix} \beta & -\alpha \\ -\alpha & \gamma \end{pmatrix} \quad (1.10)$$

The rms-emittance (ϵ) can also be obtained from these parameters:

$$\epsilon = \pi \sqrt{\langle x^2 \rangle \langle x'^2 \rangle - \langle xx' \rangle^2} \quad (1.11)$$

1.2.5 Phase Space Evolution

In a transfer line or a storage ring (i.e. no acceleration), and assuming no energy losses due to radiation, Liouville's theorem establishes that emittance (considering both transverse and longitudinal coordinates) is conserved [14].

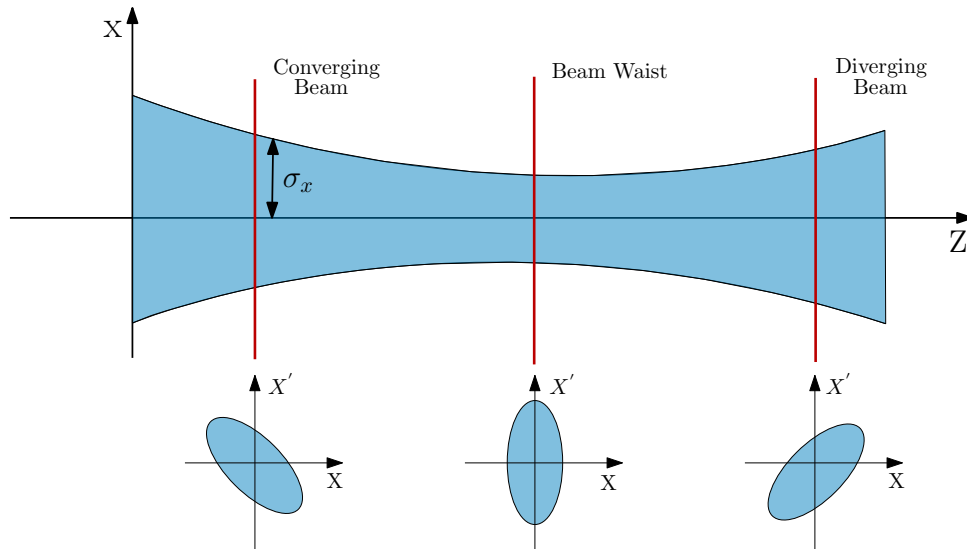


Figure 1.8: Example of phase space evolution.

However, the shape of the ellipse changes along the beam line. Fig. 1.8 illustrates a typical example of phase space evolution. In the previous sections (Sec. 1.2.1) we saw how, in linear systems, points in phase-space could be mapped from one location to the other through matrix multiplications. After some algebraic calculations, one can obtain the following transport matrix for the Twiss parameters [15]:

$$\begin{bmatrix} \beta_1 \\ \alpha_1 \\ \gamma_1 \end{bmatrix} = \begin{bmatrix} c^2 & -cs & s^2 \\ -cc' & cs' + c's & -ss' \\ c'^2 & -2c's' & s'^2 \end{bmatrix} = \begin{bmatrix} \beta_0 \\ \alpha_0 \\ \gamma_0 \end{bmatrix} \quad (1.12)$$

1.3 Beam Diagnostics

Beam diagnostics and instrumentation are essential constituents of any particle accelerator. They allow us to monitor the behavior and properties of the particle beam. Without adequate diagnostics, one would be blindly operating an accelerator and it would be impossible to assess problems and improve performances. Different accelerator types require different diagnostics. Similarly, different beam properties require very different instrumentation systems and techniques. [16], [17] and [18], are very recommendable references, where the topic of beam instrumentation is covered extensively with a very accessible approach.

Here we will only focus on describing the instruments that are relevant for understanding this work. We shall focus on the measurements of two beam properties:

- **Transverse Beam Profile Measurements:** They allow the measurement of the transverse distribution of the particles throughout the accelerator. This measurement is important to control the beam width and position, as well as the transverse matching between different parts of the accelerator facility. In particular, we will focus on devices such as Secondary Emission Grids (SEM Grids) and Wire Scanners.
- **Beam Intensity Measurements:** They allow us to measure the total electrical current of the beam. Current measurements allow, for example, to determine the transfer efficiencies in linacs and transfer lines. In this case, we will talk about Beam Current Transformers (BCT) and Faraday Cups (FC).

1.3.1 Secondary Emission Grids (SEM Grids)

Wire Grids or Secondary Electron Emission grids (SEM Grid) are devices composed of a large number of parallel fixed wires or strips. Fig. 1.9 shows an example of a SEM grid detector. They are interceptive devices, as the wires interact directly with the beam of particles. During this process, a current, proportional to the number of particles, is generated in each wire. By measuring the current in all the wires a beam profile can be reconstructed. More detailed explanations about the current generation process and the profile reconstruction will be given in Ch. 2.

SEM grids allow for a single-shot acquisition, and in some cases, it is possible to observe the evolution of the beam profile in the same pulse. The number of wires and the spacing between them varies from system to system. It is important for the detector to cover the whole range of the beam size and to have enough resolution to properly reconstruct the beam profile. Theoretically, a bigger detector with a larger

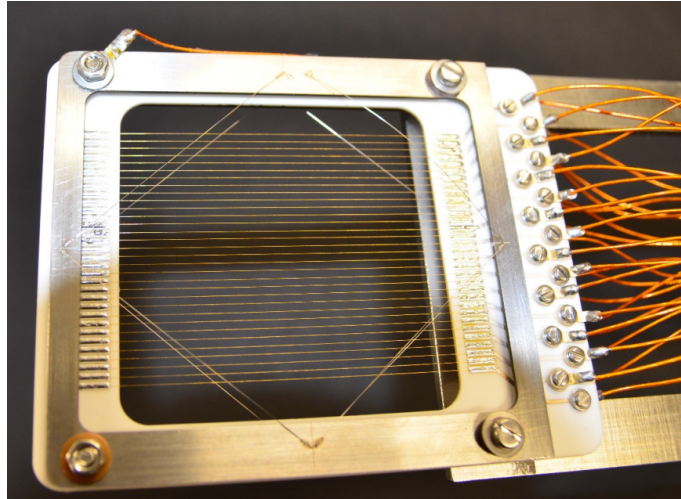


Figure 1.9: Example of a SEM grid installed at CERN accelerator Complex.

number of wires would be more convenient. However, a system with too many wires implies an overly complicated acquisition system, it increases the probability of wire cross-talk and augments the construction costs. A typical number of wires ranges from 16 to 48. In some devices, the wires are spaced unevenly, with a denser distribution in the center.

The diameter-to-spacing of the wires determines the attenuation of the beam current, which becomes an important parameter to consider for particles at low energies, as they are fully stopped in the detector's material. It is common to consider that a 10% of the beam area is covered with wires. The wire materials are selected to optimize signal generation and ensure proper thermal performance. Typical materials used for wire grid designs are Tungsten, Carbon (Graphite, CNT) or Titanium. The motion control of SEM grids is relatively simple, they are either fully inserted or fully retracted, and sometimes they might even be permanently positioned in the beam pipe with no motion control at all.

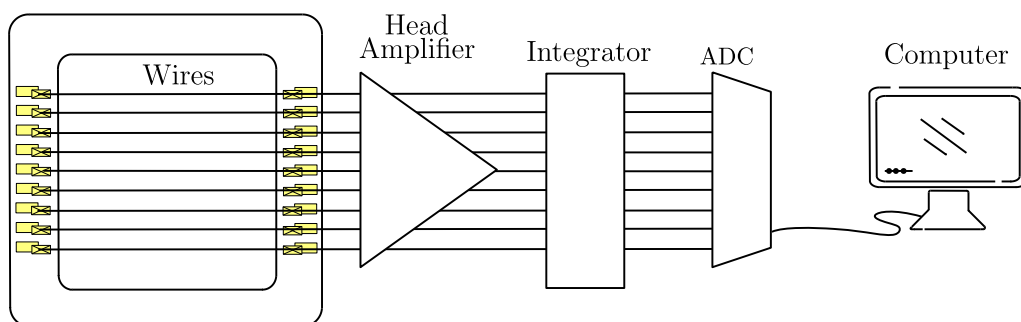


Figure 1.10: Schematic representation of SEM Grid Acquisition system.

Fig.1.10 shows a schematic representation of the sem grid acquisition system. This system is composed of a head amplifier that sits as near as possible to the grid, often in an area with radiation. It is followed by an integrator or signal conditioning circuit that sits away in a safe room. From the integrator, the signal is fed to a computer controller ADC. This scheme requires one signal cable per wire over the distance from the device to the ADC [19]. The main drawbacks of this diagnostics device are the limit on the spatial resolution (which can be hardly reduced to less

than a few hundred micrometers), the small wire signals and the complicated data acquisition system.

1.3.2 Wire Scanners

The Wire Scanners consist of a single wire that can be swept through the beam pipe (see Fig. 1.11). The main advantage of this technique is the high resolution that can be accomplished (sub-mm range). It is often used in accelerators with small beam sizes. These devices also intercept the beam of particles, however, this effect is practically negligible. The electronics and read-out system is simpler than the SEM grids. However, the mechanical design of the mechanism is much more challenging.

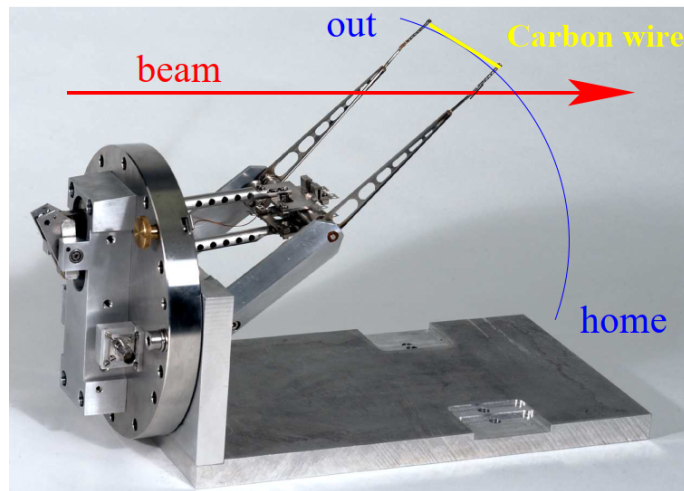


Figure 1.11: Rotational Fast Wire Scanner, used at CERN SPS.

In the context of this thesis, we differentiate between two types of wire scanners:

1. **Slow Wire Scanners:** They are commonly used on LINACs or transfer lines where the beam energy of the particle beam is small and the pulse structure consists of short pulses and low repetition rates. In this case, the profile is reconstructed by using the current generated in the detector from its interaction with the beam of particles. Due to the low repetition rate of the beam in those areas, one sample is taken on each beam pulse.
2. **Fast Wire Scanners:** For high energy and high repetition range beams, the profile is reconstructed by measuring a shower of secondary particles generated during the beam/wire interaction (for proton/heavy ion accelerators). The secondary shower is detected outside the beam pipe, with a photo-multiplier tube. The speed of the wire movement varies can go from 1 m/s up to 20 m/s.

In both cases, the measurement of the wire position is a crucial aspect of the measurement, as the beam profile is reconstructed by correlating the wire position with the generated signal. The precision of the measurements of the wire scanner positions will therefore be a crucial factor in the measurement precision and resolution. In the case of fast wire scanners, the deformations or vibrations in the wire

can also restrict spatial resolution. Beam position and beam size variations during the measurement period can induce additional errors.

For both, slow and fast wire scanners, the dimensions of the wire have a direct impact on the signal strengths and the measurement accuracy. In general wire sizes between 10 μm to 50 μm are used.

1.3.3 Beam Current Transformer (BCT)

An electric current flowing through a conductor gives rise to a magnetic field around the conductor, and passing a conducting loop through a magnetic field induces a current through the loop. These well-known principles of induction are used in the Beam Current Transformer (BCT). In this case, the particle beam is the primary current and can be described as:

$$I_{beam} = \frac{qeN_{part}}{t} \quad (1.13)$$

Where N_{part} is the number of particles of charge q per unit time t . e is the electron charge. A magnetic field is generated as the beam travels through the accelerator. One can measure this magnetic field by placing torus with high permeability around the beam. Some windings are placed around the torus and then connected to an electrical circuit for read-out. Fig. 1.12 shows a schematic representation of a BCT design. Measuring small beam currents becomes very challenging with these devices.

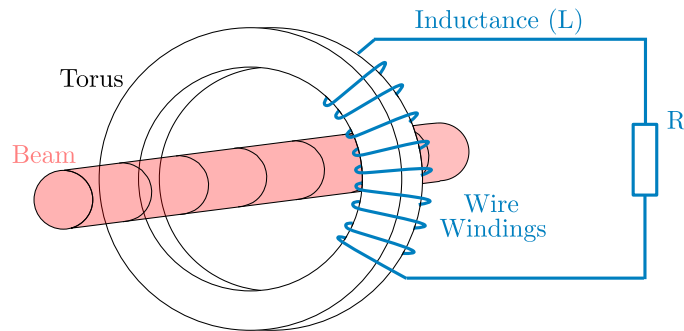


Figure 1.12: Schema of a current transformer built as a ring-core (torus).

1.3.4 Faraday Cup (FC)

A faraday cup (FC) is a beam stopper that measures the electrical current of the beam. A basic cup design is shown in Fig. 1.13. With a Faraday cup, a much lower current can be measured compared to a BCT, in the order of pA for low noise systems. These devices consist of an isolated metal cup connected to a current-sensitive pre amplifier. The current in these detectors is generated by measuring the total charge from the beam of particles deposited in them. Highly energetic particles not depositing all their energy in the detector material can negatively affect the measurement results. Similarly, a Secondary Electron (SE) suppression system has to be included in these devices to avoid errors in the measurements of current. This is done by creating very long cups, putting high voltage suppression close to the entrance, or by using a magnetic field.

Sometimes, Faraday cups are also used for higher beam currents, where measurements with BCTs are also possible, as they are easier to implement. In addition, cups serve as beam dumps. For high beam energies, one must consider the high thermal and structural shocks that these devices might suffer.

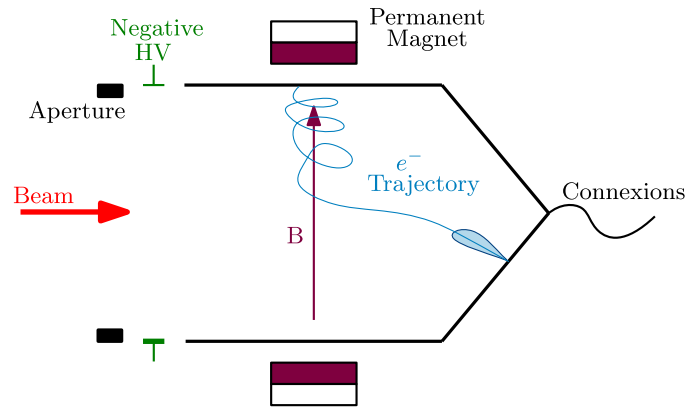


Figure 1.13: Schematic Representation of Faraday Cup.

Chapter 2

Particle Interactions with Matter

While in-depth dissertations about the broad topic of particles interaction with matter can be found in literature [20, 21, 22], this chapter will introduce the basics necessary to introduce the subject and understand later chapters.

The interactions that we will focus on are primarily those related to Coulomb forces between the incident charged particle and the electrons and nuclei of the detector material. During these interactions, the incident charged particle loses its energy and can be deflected from its original path. In the case of heavy charged particles whose rest mass is large compared with that of the atomic electron, inelastic collisions with atomic electrons are usually the predominant interaction mechanism. In such encounters, the electrons in the medium might experience a transition to an excited state (excitation) or to an unbound state (ionization).

2.0.1 The Bethe Bloch Formula

Stopping power is the parameter used to describe the gradual loss of energy of a charged particle as it penetrates into a medium. For a given incident heavy particle and target, this energy loss is highly dependent on the particle velocity. At moderately relativistic energy ranges (10 - 10⁶ MeV/amu), the electrostatic stopping power is well defined by the Bethe Bloch theory [23].

$$-\left\langle \frac{dE}{dx} \right\rangle = K z_e^2 \frac{Z}{A} \frac{1}{\beta^2} \left[\frac{1}{2} \ln \left(\frac{2m_e c^2 \beta^2 \gamma^2 T_{max}}{I^2} \right) - \beta^2 - \frac{\delta(\beta\gamma)}{2} \right] \quad (2.1)$$

With the symbol and parameter definitions given in table 2.1. The mean ionization energy is highly dependent on the material, and it can vary from a few eV for materials with low Z to a hundred of eV for materials with high Z. A good approximation can be formulated as follows [24]:

$$I [eV] = 10 \cdot Z \quad (2.2)$$

The maximum energy that can be transferred to a target electron in a single head-on collision is described by T_{max} , and can be approximated by the following formula [25]:

$$T_{max} = \frac{2m_e c^2 \beta^2 \gamma^2}{1 + \frac{\gamma m_e c^2}{M c^2} + \left(\frac{m_e c^2}{M c^2} \right)^2} \quad (2.3)$$

Finally, $\delta(\beta\gamma)$ is a parametrized density correction factor necessary for highly relativistic particles [23], its units are $MeVcm^2g^{-1}$. It is important to notice that

the energy deposited will very much depend on the characteristics of the incident particle as well as the absorber ($-\langle \frac{dE}{dx} \rangle \propto \frac{Z}{A}$).

Symbol	Definition	Units or Value
N_A	Avogadro's Number	$6.0221415(10) \cdot 10^{23} \text{ mol}^{-1}$
z_e	Charge of incident particle	
Z	Atomic number of absorber	
A	Mass Number of absorber	
I	Mean excitation energy	eV
$\beta\gamma$	Relativistic parameters	
$m_e c^2$	Electron Mass $\cdot c^2$	0.510998918(44) MeV
r_e	Classical Electron Radius	2.8179403250(28) fm
M	Incident Particle Mass	MeV/c^2
K/A	$4\pi N_A r_e^2 m_e c^2 / A$	$0.307075 \text{ MeV g}^{-1} \text{ cm}^2$
α	fine-structure constant	1/137

Table 2.1: Summary of variables used in this section.

Fig. 2.1 shows as an example, a comparison between the energy deposition of protons for different materials, as a function of the incident particle energy. In this particular case, when the material is assumed to be thin, the energy deposition increases until reaching a maximum, after which it starts decreasing. From the image, we can observe that the energy deposited in graphite and copper is larger, due to their smaller mass number. Tungsten, gold and lead present smaller energy deposition values, and are similar to one another, due to their close atomic mass number.

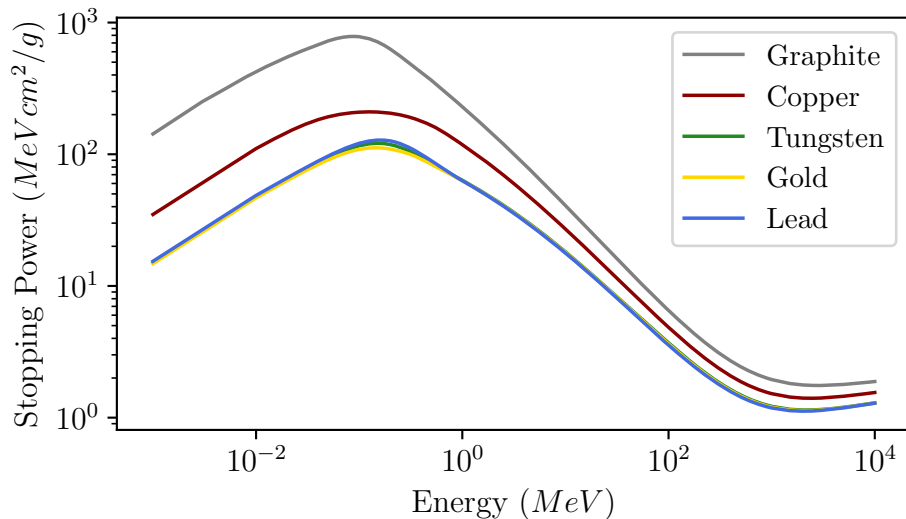


Figure 2.1: Stopping power of protons in thin foils of different materials, as a function of incident particle energy. From [26].

2.0.2 Energy Loss in Mixtures and Compounds.

One can consider a compound to be made up of very thin layers of pure elements in the right proportion. That is:

$$\frac{dE}{dx} = \sum w_j \left. \frac{dE}{dx} \right|_j \quad (2.4)$$

Where $\left. \frac{dE}{dx} \right|_j$ is the energy loss in the j-th component. However, it is important to remember that this is an approximation. The values of I and $\delta(\beta\gamma)$ are not perfectly represented by this addition method. More accurate values can be found in [27] and [28], which include measured coefficients for nearly 200 mixtures and compounds.

2.0.3 Electrons Energy Loss

For light particles such as electrons, bremsstrahlung losses are not negligible and can become dominant for energies above a few tens of MeV. One can define the critical energy (E_c) as the point where the loss rates by Ionization and bremsstrahlung are the same [29].

$$E_c = \frac{800}{Z + 1.2} \quad (2.5)$$

Fig. 2.2 shows the stopping power of electrons in a thin tungsten target, where we can observe the contribution of the radiative and collision interactions to the energy loss. In this case, radiative losses become relevant for incident electron energies $> 10\text{MeV}$. This quantity is in agreement with Eq. 2.5.

Some more information about how to model the energy losses due to this process can be found in [30]. However, in this thesis bremsstrahlung losses will be neglected, as we will always remain under the critical energy.

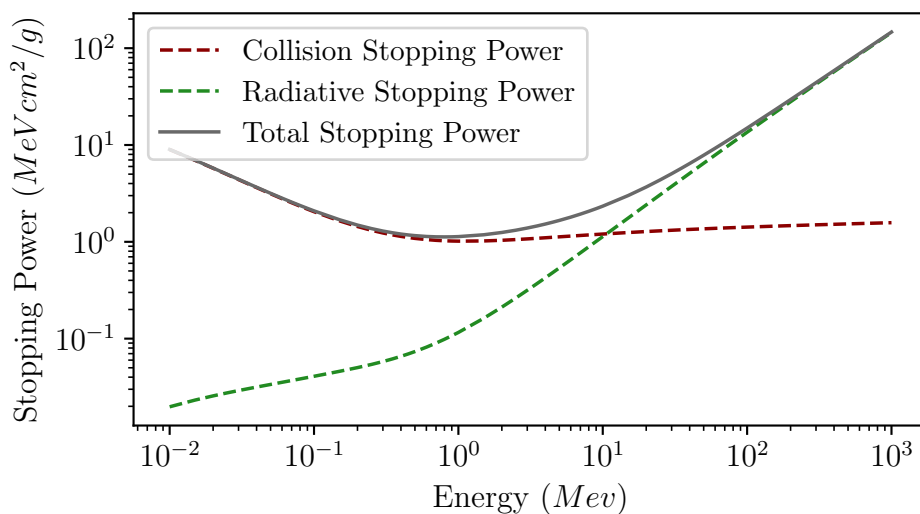


Figure 2.2: Stopping power of electrons in a thin tungsten foil, as a function of incident particle energy. From [26]

2.0.4 Multiple scattering and Backscattering

While traversing the material, the particle can be deflected from its original path. Most of these deflections occur due to Coulomb scattering with the atomic nucleus (Rutherford-type collisions). These collisions result in small angular deflections (if $m_{nucleus} \gg m_{particle}$). Fig. 2.3 (left) shows a schematic representation of this process.

The thicker the absorber and the larger its atomic number Z , the greater the likelihood that the incident particle will suffer multiple scattering events. Generally, 20 collisions are deemed sufficient to consider multiple scattering. Multiple scattering can be treated statistically if the number of successive encounters is high enough. This is well represented by the theory of Moliere [31], which assumes that after a distance L traveled through the material, the angular distribution of the particles with respect to their initial direction is Gaussian in shape and centered around the direction of the incident particles. This assumes that the deflection angle is very small ($\theta \leq 10$ deg). In these conditions, the mean square angle of such a Gaussian distribution can be calculated as follows:

$$\theta_0 = \frac{13.6 MeV}{\beta pc} z \sqrt{\frac{l}{X_0}} \left[1 + 0.038 \ln \left(\frac{l}{X_0} \right) \right] \quad (2.6)$$

l/X_0 is the thickness of the medium, described in terms of the radiation length (X_0), discussed in the next section. p , β and z are the momentum, velocity and charge number of the incident particle. Experimental measurements show excellent agreement with the Gaussian distribution at small angles, and as expected, start differing at larger angles. This divergence can be explained due to the higher probability of close encounters, which result in larger scattering angles.

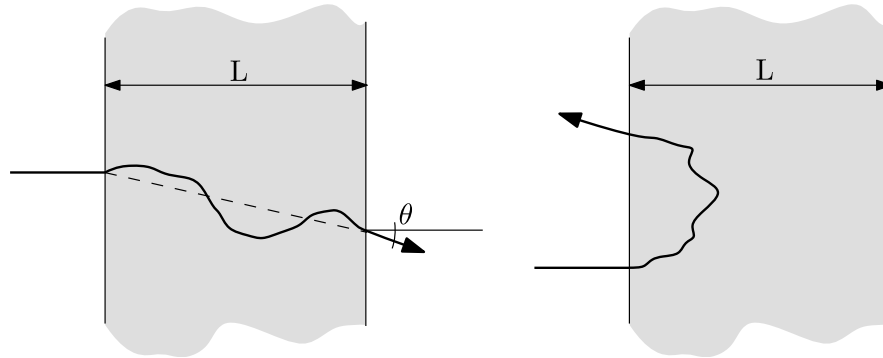


Figure 2.3: Left: Schematic representation of multiple coulomb scattering. Right: Schematic representation of electron backscattering.

It is very difficult to study any theory of multiple scattering for incident light particles such as electrons, due to the large number of scattering processes, not only by the atomic nuclei but also by the other electrons in the medium [32]. Eq. 2.6 is no longer valid in the case of a light particle [33], where large scattering angles are not rare. If an incident particle is scattered back of the material, it is called a backscattered particle. See Fig. 2.3 (right) for a schematic representation of the phenomenon. Experimental information about this phenomenon has been intensively collected and from an empirical point of view, this phenomenon is well

understood. However, attempts at a theoretical interpretation of the data have only limited success [34].

For this document, we will only concern ourselves with the back-scattering electron yield (BS_{el}), which can be defined as the ratio between the number of outgoing primary electrons and the incident electron flux. Back-scattering of heavier particles, such as protons, is also possible. However, for our range of energies and materials, we consider this to be negligible.

2.0.5 Path Length and Range

The distance traveled by a particle inside a target until it loses all its energy can be quantified using the range. The range is an experimental concept, for which there are several definitions, all roughly relating to the same quantity [20]. In this document, the range (R) is defined as the penetration depth in a medium that reduces the number of incident particles to one-half. The maximum penetration depth (R_{max}) is defined as the depth in the absorbing medium beyond which no particles are observed to penetrate. Finally, the total path length describes the distance traveled by the particle measured along the actual path of the particle. Fig. 2.4 illustrates the differences between these definitions.

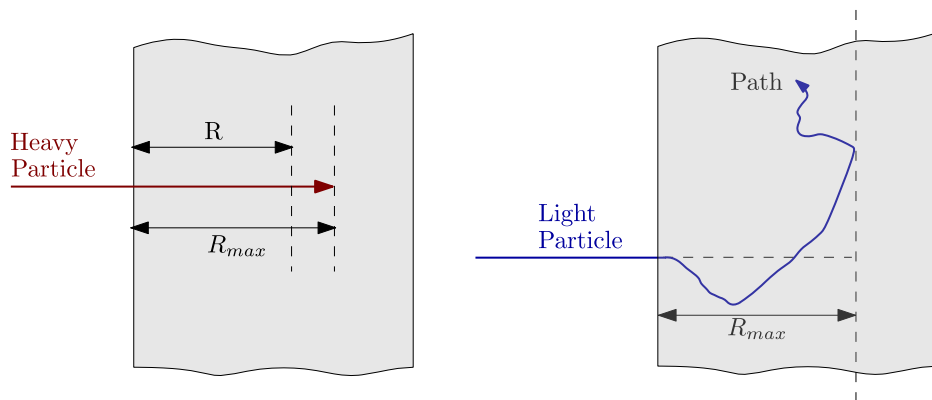


Figure 2.4: Schematic diagram of charged particle penetration into absorbing medium. Left: Heavy charged particle. Right: Light Charged particle.

The range highly depends on the type of particle, its energy and on the material through which it passes through. For a heavy particle that losses energy through ionization and atomic excitation, the range (R) can be calculated through the Continuous Slowing Down Approximation (CSDA):

$$R_{CSDA} = \int_0^{E_0} \left(\frac{dE}{dx} \right)^{-1} dE \quad (2.7)$$

Where E_0 is the initial particle energy. This approximation assumes a smooth path, without hard collisions and large scattering angles. Some examples of analytical derivations of this equation can be found in [35]. The CSDA range for heavy non-relativistic charged particles, of mass M_0 and energy E_k , in a given absorber can be written in terms of the proton CSDA range (R_{CSDA}^p) as follows:

$$R_{CSDA}^{M_0}(E_K) = \frac{1}{Z^2} \left(\frac{M_0}{m_p} \right) R_{CSDA}^p \left[E_K \frac{m_p}{M_0} \right] \quad (2.8)$$

Where M_p is the proton mass and Z is the atomic number of the incident ion. This can be very useful, as the range of protons in a variety of absorbers has been extensively measured. For heavy charged particles, $R_{max} \sim R_{CSDA}$ in all types of absorbing media.

In the case of light particles, this CSDA approximation is not valid due to the very tortuous path that they experience in the absorbing medium. In this case, the CSDA range can be up to twice the average path for high Z absorbers ($R_{max} = 1/2R_{CSDA}$). A useful quantity in the case of light particles is called the radiation length (X_0), usually measured in gcm^2 . This gives us a mean distance over which high-energy particle losses all but $1/e$ of its energy by Bremsstrahlung. Different values for this quantity are available in literature, estimated with varying degrees of approximations. Some of these expressions can be found in [36] and an example of an expression for high energetic electrons in high Z materials:

$$X_0 = \frac{716.405A}{Z(Z+1)\ln(183Z^{-1/3})} \quad (2.9)$$

2.0.6 Types of Absorbers

We will distinguish between thin and thick absorbers. In thin absorbers, only a few collisions of the projectile with the target atoms are likely to happen. Contrarily, in thick absorbers, a projectile experiences many collisions and the projectile energy lost by the incident particle is considerable. One can consider a target to be thin when the range of the incident particles is much larger than the thickness of the material ($R(E_k) \gg L$). For thin absorbers, the energy loss is small and the stopping power doesn't change much along the length of the material. The total energy loss in the absorber can be calculated as:

$$\Delta E = - \left(\frac{dE}{dx} \right)_{avg} \cdot L \quad (2.10)$$

Here, the trajectory of the particle is also assumed to be perfectly linear in the absorber. If the range of the particles in the material is comparable to the thickness or smaller, this approximation is no longer valid, as one would underestimate the real energy deposition in the material. The energy is lost, the probability of interactions with the absorber material increases, since the ionization interaction cross-sections are bigger for smaller energies. A plot representing the specific energy loss along the incident particle track is called the Bragg curve. Fig. 2.5 shows an example of Bragg curve in the case of 3 MeV protons in graphite.

2.1 Secondary Electron Theory

When a particle passes through the interface of a material, it will transfer energy to the electrons in the medium. Depending on the energy these electrons get, they can be excited to a higher energy level, or gain enough energy to be emitted from the material, this emission process is known as Secondary Electron Emission (SEE) [37]. The SEE process can be generally divided into three consecutive steps:

1. Generation Process: The energy required to ionize the atoms in the material is the minimum energy needed to create a secondary electron (SE). If the

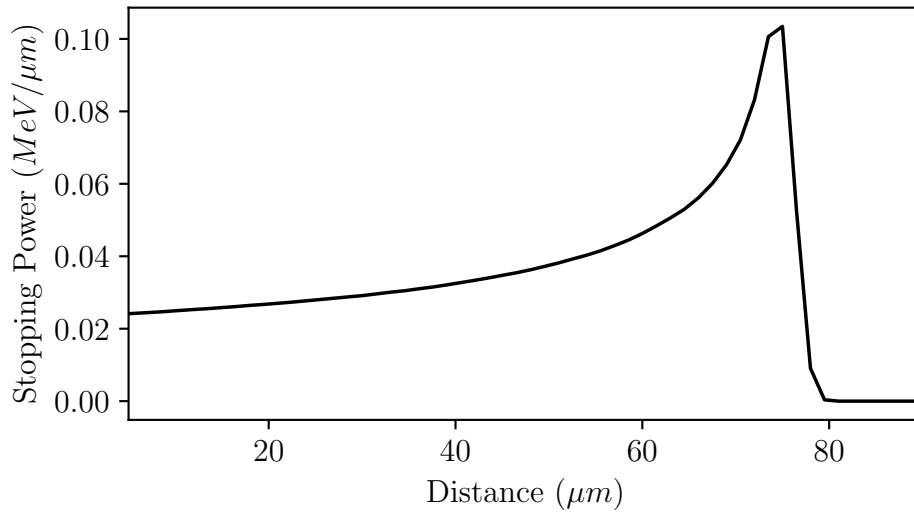


Figure 2.5: Bragg peak of 3 MeV protons in Graphite.

incident projectile is an ion containing electrons, these electrons can also be stripped off and produce further ionization. However, if the electrons from the incident ions are scattered off the material, they cannot be counted as secondary electrons.

2. Diffusion Process: While the SE travel through the material, they lose energy. This energy loss permits only a very shallow penetration depth of the low-energy electrons. For that reason, SE tends to be a surface phenomenon.
3. Emission Process: To be emitted from the surface, the SEs have to overcome the surface barrier potential [38]. The escape process is of particular importance because it determines the final shape of the secondary electron distribution. Moreover, the velocity vector, when reaching the surface, must allow the SE to escape. In the case of metals and semiconductors, a cosine-type angular distribution of SE is observed [39]

Many experimental measurements of secondary electrons have been done since the discovery of this phenomenon in 1902, revealing some commonalities: In the case of SEE from metal surfaces [41], The energy spectra of SE peak at about 1-5 eV; The full width of the peak is around 3-15 eV; It is commonly said that SE, in general, have an energy < 50 eV. Fig. 2.6 shows the spectra of SE emitted from different metals for an incident 500 keV proton.

The main parameter describing the SEE is the Secondary Emission Yield (SEY). It describes the average number of electrons emitted per incident projectile. A semi-empirical treatment of SEY was formulated by E.J. Sternglass in 1957 [42]. In this formulation, two sources of SE are considered. Firstly, the SE generated by small energy transfers from the incident particles to the target electrons. This first mechanism is the main contributor to the SEY. Secondly, a smaller contribution comes from the SE generated by delta electrons (defined in the following section). This formulation allows for the following numerical relation:

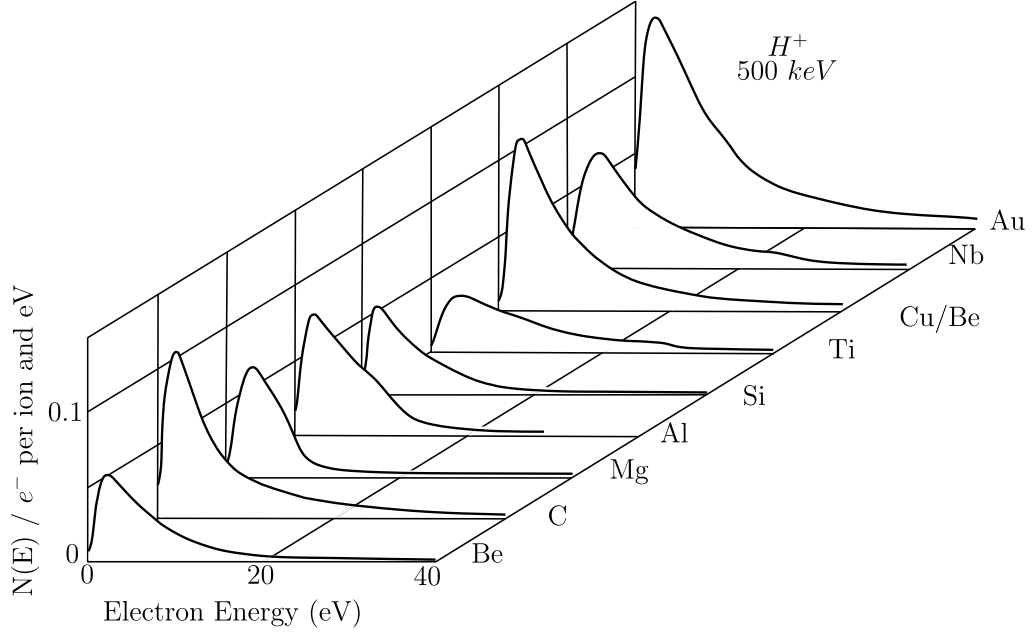


Figure 2.6: Ion induced secondary electron spectra for a variety of metals. Incident ion: Proton 500 keV. From [40]

$$SEY = 0.01L_S \left. \frac{dE}{dx} \right|_{el} \left[1 + \frac{1}{1 + 5.4 \cdot 10^{-6} E/A_p} \right] \quad (2.11)$$

$$L_S = (3.68 \cdot 10^{-17} N_v Z^{1/3})^{-1} \quad (2.12)$$

Here, E and A_p are the kinetic energy and the mass of the projectile. L_s is the characteristic length, which is of the order of the distance between inelastic collisions, and it is expressed in (cm). N_v is the number of atoms per unit volume. dE/dx is the energy deposition in the material due to interactions with the electrons. It should be expressed in eV/cm. As we saw previously (subsection 2.0.1), this term is greatly affected by the speed of the incident particle and its nature.

The Secondary Emission Yield also depends on the angle of incidence of the incident particle. In the theory of Sternglass, the angular dependence is treated as a change in the effective penetration distance L_s . If the particle impacts at an angle different to the normal, the effective track length of the projectile extends by a factor $1/\cos(\theta)$. In that case the corresponding SEY would be:

$$\frac{SEY(\theta)}{SEY(0)} = \frac{1}{\cos(\theta)} \quad (2.13)$$

Experimental values confirm this approximation for incident angles up to 70 deg. However, if the incident particles are electrons, recent measurements show a different angular dependence [43]:

$$\frac{SEY(\theta)}{SEY(0)} = e^{0.5(1-\cos(\theta))} \quad (2.14)$$

Early investigations of SEE already show a dependence of SEE on temperature [44]. Temperature seems to affect the escape probability. An increase in temperature results in increased vibrations of the atoms about their equilibrium position,

which should reduce L_s , therefore increasing the Yield. Sternglass gives a rough quantitative hypothesis that goes as follows:

$$\frac{L_S(T_1)}{L_S(T_2)} = \frac{1 + 2.5 \cdot 10^{-3}T_1}{1 + 2.5 \cdot 10^{-3}T_2} \quad (2.15)$$

Where $L_S(T_1)$ is the characteristic length at T_1 and $L_S(T_2)$ is the length at T_2 . It is important to note that the semiempirical theory of secondary emission is only considered to be accurate for backward emission (projectile entering the target). As a first approximation, here we will consider that this formulation is also valid for rear-face emission.

2.1.1 Delta Rays

Most frequently, the electrons generated by SE have low energy. However, if the energy transferred to the electron is above a few hundred eV (up to T_{max}), they might be able to generate further ionization on their own. An analytical formulation for the total number of δ -rays produced from charged particle interactions was presented by Rossi in 1952 [45], and gives the distribution of δ rays for incident particles with energy $I \ll T \ll T_{max}$ as follows:

$$\frac{d^2 N_\delta}{dT dx} = \frac{1}{2} K z^2 \frac{Z}{A} \frac{1}{\beta^2} \frac{F(T)}{T^2} \quad (2.16)$$

Where T_{max} is given by Eq. 2.3. The factor F is spin-dependent, but it is about unity for $T \ll T_{max}$. To calculate the total number of generated delta rays per unit of distance, one can integrate the previous equation from an arbitrary lower limit to the maximum energy for delta rays can get (T_{max}), described by Eq. 2.3.

Chapter 3

Secondary Emission Monitors Signal Modeling

As explained in the previous chapter several processes can contribute to the signal generated by particle beams interacting with the thin targets used as secondary emission monitors. This chapter discusses the semi-empirical model used to estimate such a signal. This model has been used extensively to predict and interpret the signal generated in various detector types. As an example, its application to the detectors used for the LINAC4 H^- beam will be presented.

3.1 Signal Generation in SEM

The schematic diagram in Fig. 3.1 describes the various contributions to a SEM detector signal. If we consider an incident projectile P_{proj} constituted by N_p protons and N_e electrons, one can define the net charge generated on a SEM as:

$$Q\left(\frac{e}{Proj}\right) = Q_{dep} + Q_{SE} + Q_{th} \quad (3.1)$$

where Q_{dep} is the direct charge deposition, Q_{SE} the contribution from secondary electron emission and Q_{th} the one from thermionic electrons emission.

3.1.1 Charge Deposition (Q_{dep})

The electrical charge directly deposited in the target depends on the probability of the protons and the electrons to be stopped in the target itself. This can be written as:

$$Q_{dep} = N_p \cdot \eta - N_e \cdot \mu \quad (3.2)$$

where η is the proportion of protons that are stopped in the material and μ the proportion of electrons. These parameters depend on the range of the particles in the detector material, and on the back-scattering probability.

3.1.2 Secondary Emission Charge (Q_{SE})

Each charged particle entering or exiting the detector surface has a certain probability of generating secondary electrons (SE) that escape the wire. The model

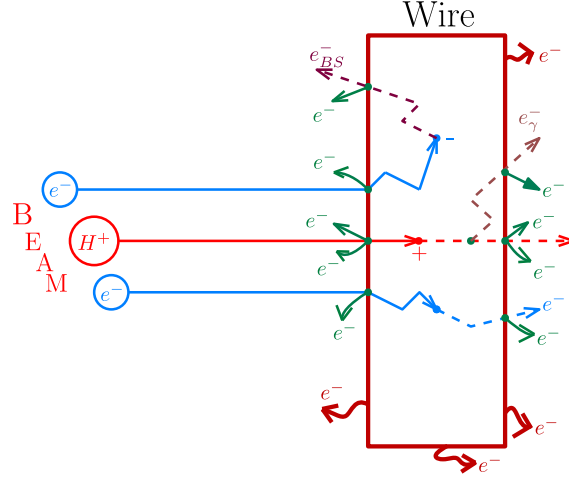


Figure 3.1: Schematic representation of the processes inducing current in the detector material.

adopted can be summarized as follows:

$$Q_{SE} = N_p \cdot SEY_{p1} + N_p (1 - \eta) SEY_{p2} + N_e \cdot SEY_{e1} + N_e (1 - \mu) SEY_{e2} + N_p \cdot BS_p \cdot SEY_{BSp} + N_e \cdot BS_e \cdot SEY_{BS_e} \quad (3.3)$$

In all the cases, SEY represents the secondary emission yield that was introduced in Section 2.1 and it can be induced by both the incident protons (SEY_p) and the electrons (SEY_e). Secondary emission is a surface process. In the case of a thin target detector, SE can occur at the entrance surface (SEY_1) and at the exiting one (SEY_2). In some cases, the probability of electron and proton back-scattering (BS_e and BS_p) is not negligible. In those cases, one must also consider the contribution of the secondary electrons generated due to the backscattered particles crossing twice the incident surface (SEY_{BEp} and SEY_{BEe}).

3.1.3 Thermionic Emission Charge (Q_{Th})

Thermionic emission is the process by which free electrons are emitted from the surface of a metal when they gain enough thermal energy to overcome the work function. As thermionic electrons are negative charges exiting the material surface, they will contribute to signal generation. J_{Th} is the current density of emitted electrons and it is described by Richardson-Duschman equation [46]:

$$J_{Th} = A_R \cdot T^2 \cdot \exp\left(-\frac{\phi}{k_B T}\right) \quad (3.4)$$

where A_R is the Richardson constant and K_B is Boltzmann's constant. From this equation, one can observe the dependence on temperature, which makes this term negligible at low temperatures but meaningful when the detector material is heavily heated.

3.2 Signal Generation Studies at LINAC4.

As introduced in Section 1.1.1, LINAC4 accelerates H^- particles up to 160 MeV. H^- ions consist of one proton ($N_p = 1$) and two electrons ($N_e = 2$). In this case, assuming that for both electrons and protons the SEY yield is the same at the entrance and exit of the detectors, formula 3.1 can be written as:

$$Q\left(\frac{e}{H^-}\right) = \eta - 2\mu + (2 - \eta + BS_p) \cdot SEY_p + 2(2 - \mu - BS_e) \cdot SEY_e \quad (3.5)$$

At LINAC4, the wires have a width of 40 μm for the case of tungsten and 33 μm for the case of graphite. Tungsten wires are used at high energies. Graphite wires are located at lower beam energies. Fig. 3.2 shows the range of protons as a function of the particle energy for the two materials.

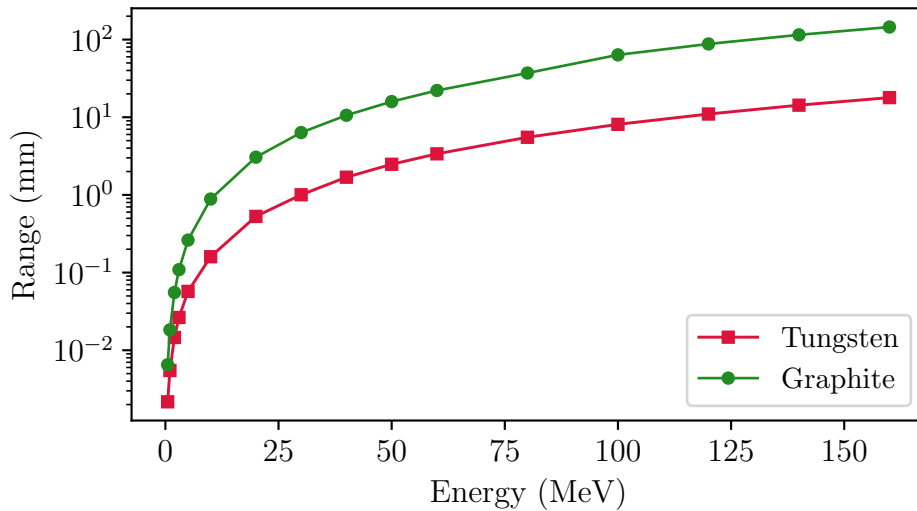


Figure 3.2: Range of particles as a function of incident ion energy.

As can be intuitively anticipated, the range of the particles in the material increases with energy. Due to the different material densities, at a fix energy, the particles have a much larger range in the case of graphite compared to tungsten. The range of protons is larger than the detector thickness in most of the energy range. Only in tungsten detectors placed at energies smaller than 5 MeV the protons can be stopped.

As the H^- enter the wire material, the two electrons are stripped. Such electrons, with a kinetic energy reduced a factor $m_p/m_e = 1836.15$ w.r.t. protons, always have a small range in the the targets have high probability to be stopped. So we expect to always have a double negative charge contribution.

Table 3.1 summarizes the values of η and μ parameters along the LINAC4 accelerator. This table also summarizes the values of the Backscattering probabilities for electrons and protons. All these values have been calculated with Geant4 [47]. The back-scattering probability is negligible for protons but not for electrons. In the case of tungsten, for ion energies of 160 MeV, half of the electrons are backscattered.

p^+ energy (MeV)	e^- energy (keV)	Graphite				Tungsten			
		η	μ	BS_p	BS_e	η	μ	BS_p	BS_e
3	1.63	0.001	0.918	0.0	0.081	1.0	0.632	0.0	0.367
50	27.23	0.0	0.931	0.0	0.068	0.0	0.506	0.0	0.493
102	55.55	0.0	0.887	0.0	0.112	0.0	0.487	0.0	0.512
160	87.14	0.0	0.857	0.0	0.142	0.0	0.464	0.0	0.536

Table 3.1: Summary of charge deposition and backscattering probabilities for Tungsten ($40\mu m$) and Graphite ($33\mu m$) detectors.

Fig. 3.3 shows the SEY calculated with the semiempirical Sternglass formula (Eq. 2.11) as a function of the incident proton energy. In both materials, the SEY reaches a maximum (0.1 MeV) and then decreased. The SEY is higher in Graphite for proton energies below 300 keV and in Tungsten above.

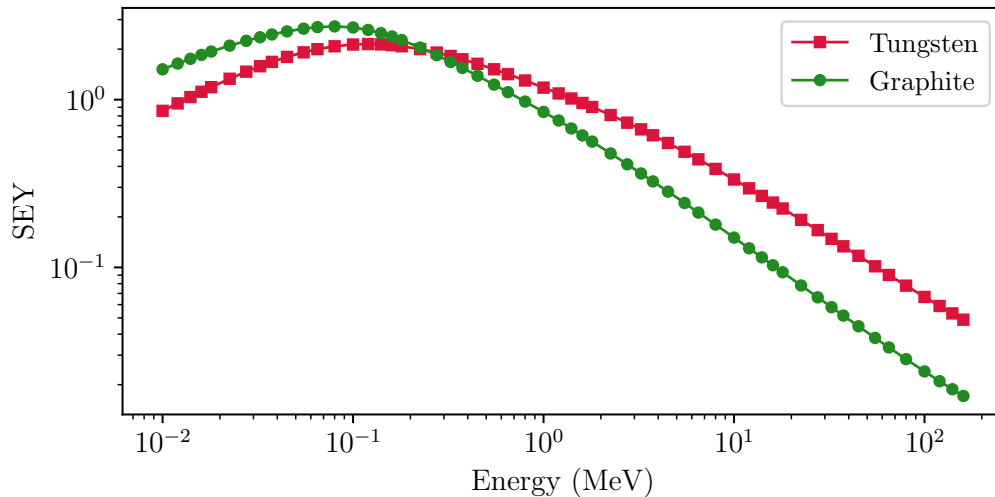


Figure 3.3: Secondary Emission Yield as a function of incident proton energy.

Putting all the terms together, one can estimate the signal for a monitor traversed by a Gaussian beam. As an example, Fig. 3.4 shows a simulated beam profile at 3 MeV and 160 MeV. From these figures, we can observe how at 3 MeV the positive contribution to the charge is predominant. For tungsten, at 3 MeV, the overall signal is negative as the charge deposition contribution is higher than the SEY. At 160 MeV, the absolute signal in tungsten is also smaller than in graphite due to this high SEY.

At LINAC4, even if these detectors are called Secondary Emission Monitors, the biggest contribution to the charge formation is the charge deposition term. Indeed, to enhance the signal, SE is typically suppressed by a bias current. At LINAC4, the detectors at lower energies are usually conformed with graphite wires, to avoid the positive contribution of the proton charge deposition.

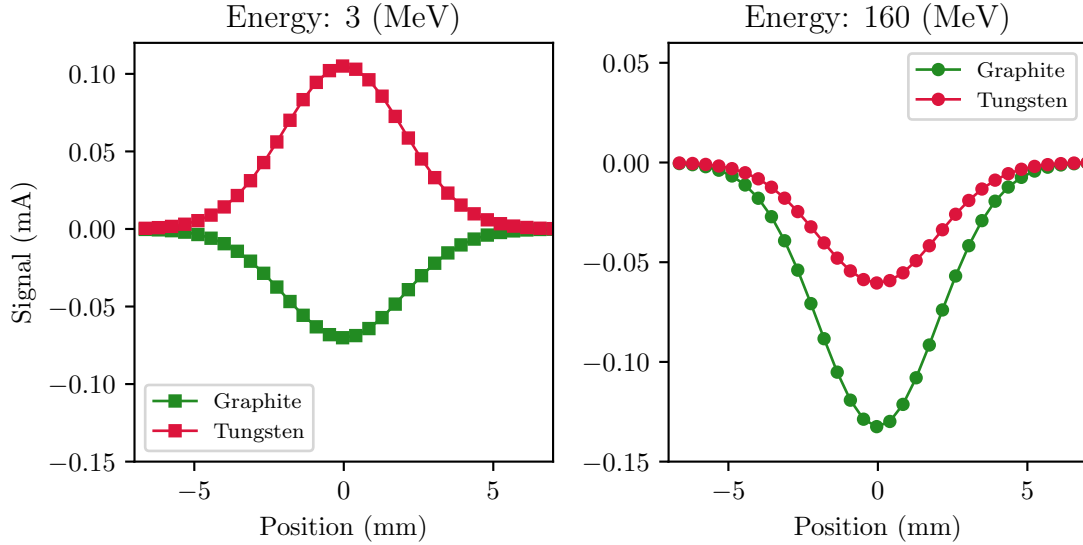


Figure 3.4: Expected transverse beam profile for incident H^- particles. Left: 3 (MeV), Right: 160 (MeV). For these simulations, a 25 mA, 100 μs particle beam was considered.

3.3 Beam Intensity and Profile Measurements.

All the results presented in this section refer to the first profile and current measurements for the *LBE run*, which took place in November 2019 [48]. The LBE is a beam line located between the LINAC4 and the PSB, only composed of quadrupole magnets and beam instrumentation, mainly designed for transverse emittance measurements. Figure 3.5 shows a schematic representation of Linac4, with the beam lines locations and naming. During the *LBE run*, the beam was for the first time extracted from LINAC4 at 160 MeV and sent to the LBE line instead of injecting in the PSB, which was not ready yet.

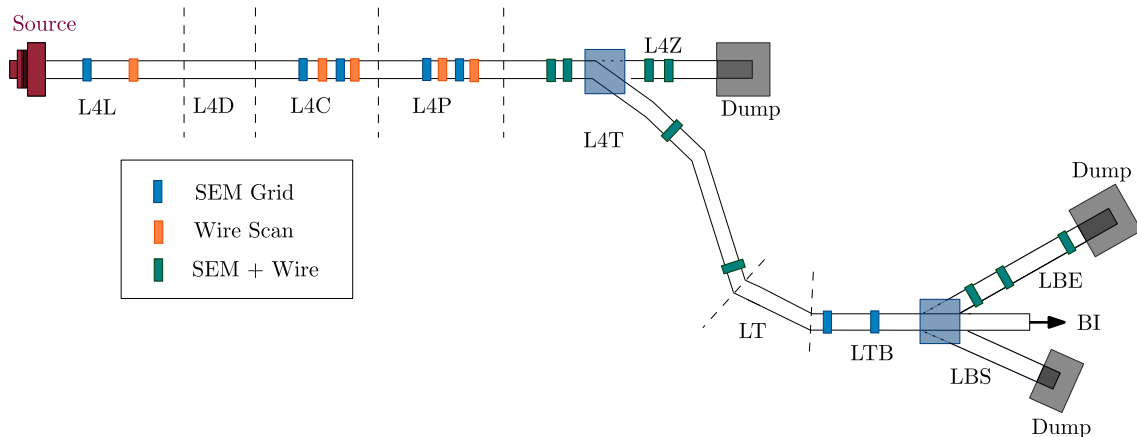


Figure 3.5: Schematic representation of Linac4 and the profile monitor locations.

The objective of these measurements was to study the transverse profile evolution of the particle beam along the LINAC4 accelerator. These measurements were the first systematic set of measurements in the transfer line from the LINAC4 to

the PSB, carried out to understand the beam evolution along the accelerator and tune the LINAC4 settings. They also helped to assess and correct any issues on the measuring devices, such as broken wires, position misreadings, data acquisition problems, etc.

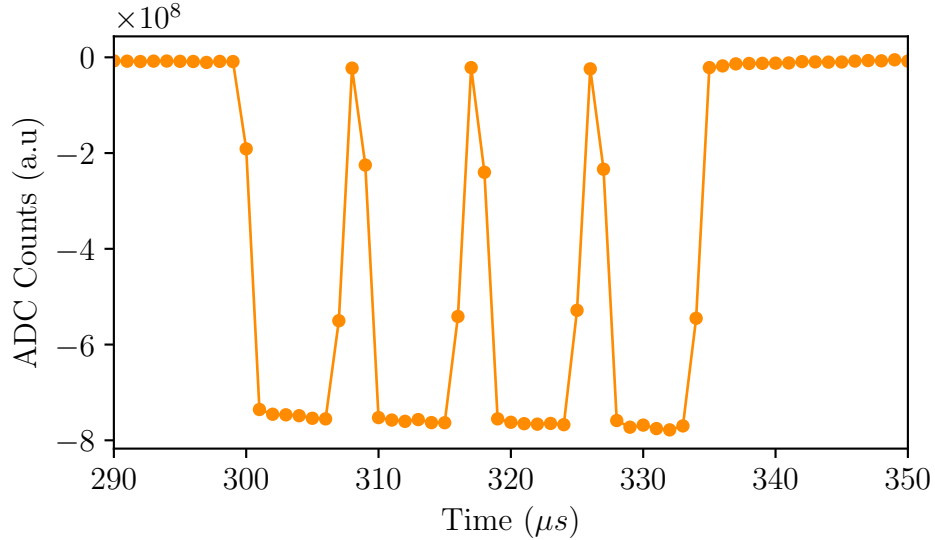


Figure 3.6: Beam current shape along beam pulse, from the first BCT in L4T line.

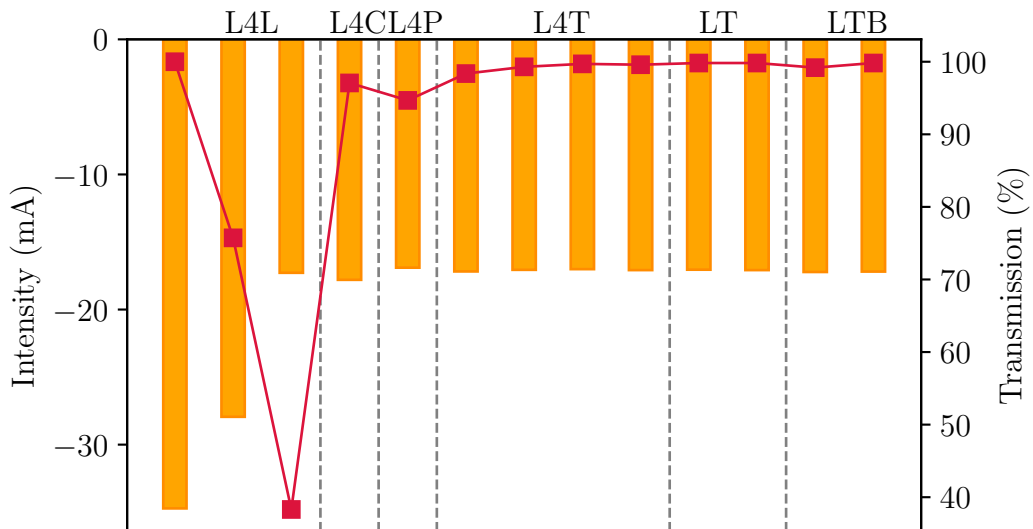


Figure 3.7: Average intensity measured by the different BCTs at LINAC4. Transmission along the LBE line.

Fig. 3.6 shows an example of intensity measurement taken by the first Beam Current Transformer (BCT) located in the L4T section at 160 MeV. In this case, the beam pulse length was $360 \mu\text{s}$ with an average intensity of $\sim 17 \text{ mA}$. One can observe the $1 \mu\text{s}$ gaps generated by the chopper, which make the beam pulse ready to be injected into the different PS Booster rings.

By measuring the average current of the beam at all the available BCTs in the LINAC and transfer line, one can assess the beam transmission along the accelerator. Fig. 3.7 shows an example in which, as desired during normal operation, the beam transmission remains very close to 100% along the whole accelerator. Similarly, the beam profile was measured along the accelerator, to cross-check the beam evolution as well as to assess the integrity and status of the devices installed along the accelerator. Fig. 3.8 shows the measurements of the horizontal profile of the beam along the LINAC4 accelerator¹. All these measurements were taken with the SEM grids. From this figure we can observe:

- The beam profile seemed to be very much Gaussian in all the measurement points except for LBE1 and LBE2 positions.
- Broken wires: SEM grids L4T2 and LBE3 present a broken wire that must be repaired. Wires 12-13 and 14-15 in L4P1 are glued together.
- Some of the grids have an even wire separation while others present a non even wire distancing.

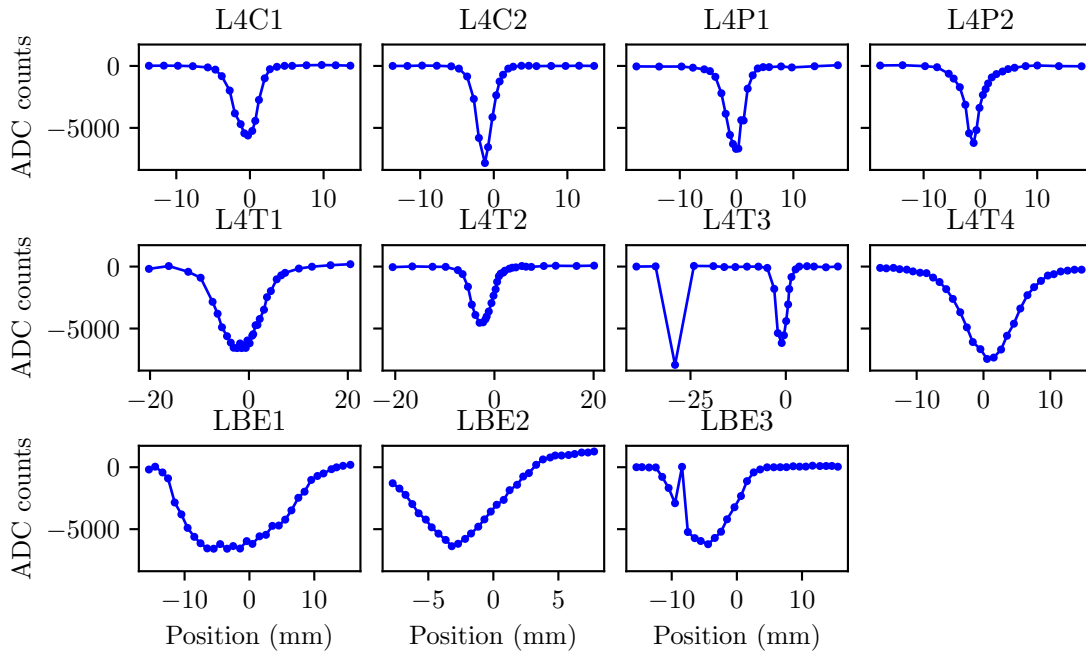


Figure 3.8: Horizontal transversal beam profile measured by the different detectors at LINAC4

The evolution of the vertical profile was similarly studied. Also, measurements of the transverse beam profile were taken with the wire scanners. Fig. 3.9 shows an example of a vertical profile taken with both the second SEM grid and the second Wire Scanner from the L4T line. In this case, the particle beam clearly shows some shoulders or tails that push it away from the Gaussian distribution. Another thing that one can observe from this figure is the very good agreement between wire grids and the wire scanners.

¹A schematic of the transverse profile locations will be shown in Fig. 5.2

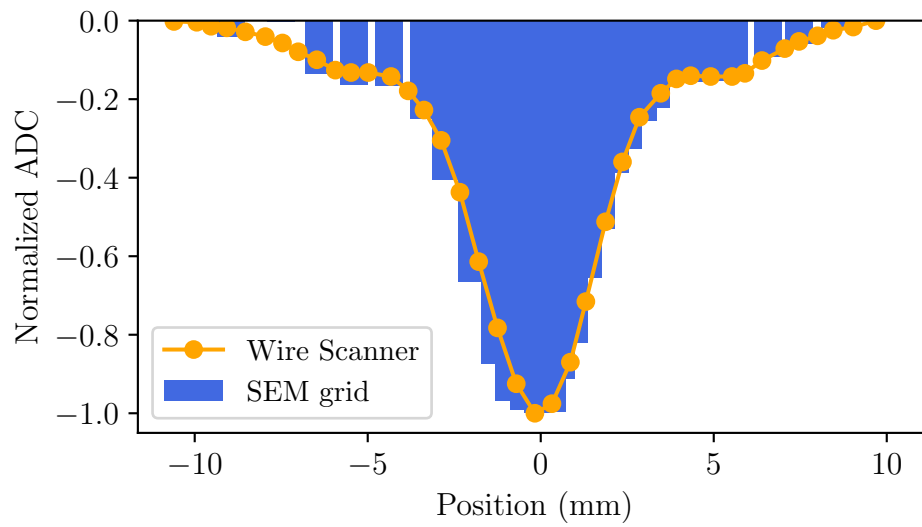


Figure 3.9: Vertical transverse profile measured by the second SEM grid and second wire scanner of the L4T line at Linac4.

Chapter 4

Thermal Modeling of Thin Target Detectors.

The bulk of this thesis consisted in implementing a thermal simulation code able to reproduce the thermal evolution of thin target detectors during operation. The work started from what implemented by M. Sapinski in 2012 for fast wire scanners [49]. It was then extended in functionalities/interfaces and generalized to other types of thin target detectors, such as wire grids, slow wire scanners and foils.

4.1 Introduction and Motivation

During operation, intercepting devices interact directly with the beam of particles. As discussed in chapter 2, the particles energy deposition depends on the beam energy, the type of particle but also the detector's material and geometry. The deposited energy leads to a fast increase of the detector temperature. Depending on the beam conditions, the thermal shock suffered by the detectors can be very severe. This might affect the measured currents (e.g. due to Thermionic Emission), and damage the detectors.

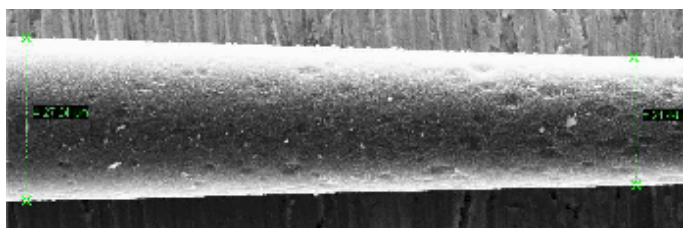


Figure 4.1: Carbon fiber wire scanner used at SPS in 2008.

Fig. 4.1 shows a picture of a wire scanner photographed with a scanning electron microscope. This scanner was used in 2008 at CERN SPS during a systematic breakage experiment [49]. The picture shows the consequence of high temperature that caused the wire radius reduction due to sublimation.

Another clear example of detector damage due to high temperature can be observed in Fig. 4.2. In this case, we can observe three pictures taken from a wire grid used at LINAC4 in 2019. This grid had $40\ \mu\text{m}$ gold-coated tungsten wires. Already in the first picture (left) one can observe how the gold coating was evaporated from the wires in the central part of the grid (Gold Melting Temperature is $1400\ \text{K}$).

From the images taken with the optical microscope (right), we can observe two wires glued together due to the high temperatures reached by the detector. To avoid these permanent damages, a deep understanding of the thermal evolution suffered by the detectors is necessary.



Figure 4.2: SEM Grid used at Linac4, in L4T Line.

4.2 The heat equation

The general equation describing the thermal evolution of thin target detectors can be written as:

$$\left(\frac{\partial T}{\partial t}\right)_{tot} = \left(\frac{\partial T}{\partial t}\right)_{Ht} - \left(\frac{\partial T}{\partial t}\right)_{Rd} - \left(\frac{\partial T}{\partial t}\right)_{Cd} - \left(\frac{\partial T}{\partial t}\right)_{Th} - \left(\frac{\partial T}{\partial t}\right)_{Sub} \quad (4.1)$$

The term with sub-index Ht represents the beam heating, and the other terms represent the different cooling processes: radiative (Rd), conduction (Con), thermionic (Th) and sublimation (Sub). Since in our case this thermal model is meant for applications in ultra-high vacuum conditions ($10^{-6} - 10^{-9}$ mbar), convection cooling is not considered. Even if not explicitly written in the equation in order to simplify the notation, each temperature term must be intended as variable with temporal (t) and spatial coordinates (x, y). Due to the thin target nature of the detectors, the dependence on the coordinate (z) along the beam axis can be neglected in the model.

4.2.1 Target Heating (Ht)

Beam-induced detector heating can be reconducted to two possible phenomena:

- **Direct Beam Energy Deposition:** It is related to nuclear and atomic interactions of the beam of particles with the material of the detector.
- **Indirect Electromagnetic Coupling:** This is related to the energy exchange due to electromagnetic coupling between the beam of particles and the detector.

Indirect electromagnetic coupling is a phenomenon that can be heavily mitigated by properly designing the detector geometry, and will not be covered in this work. If it is of the reader interest, a detailed description of this phenomenon can be found

in [50]. One can describe the temperature variation due to direct energy deposition as follows:

$$\left(\frac{\partial T}{\partial t}\right)_{Ht} = \frac{N(x, y, t)}{V \cdot Cp(T) \cdot \rho(T)} \cdot \frac{dE}{dx} \quad (4.2)$$

where V , $Cp(T)$ and $\rho(T)$ are the volume, specific heat and density of the detector's material. dE/dx is the single particle energy deposition, which was explained in Chapter 2. $N(x,y,t)$ refers to the surface density of beam particles reaching a point in space (x,y) at time t . This concept can be generalized to any particle distribution. However, in most cases, the particles transverse distribution is Gaussian and $N(x,y)$ can be written as:

$$N(x, y) = \frac{N_{Tot}}{2\pi\sigma_x\sigma_y} \cdot \exp\left(-\frac{1}{2}\left(\frac{x-x_0}{\sigma_x}\right)^2 - \frac{1}{2}\left(\frac{y-y_0}{\sigma_y}\right)^2\right) \quad (4.3)$$

Here x_0 and y_0 represent the coordinates of the beam centroid and σ_x and σ_y the normal distribution standard deviation. N_{tot} is the total number of particles (per unit time) in the particle beam. The temporal distribution can be approximated as a pulse train function. This means:

$$\begin{cases} N(x, y, t) = N(x, y) & \text{if } Beam = Yes \\ N(x, y, t) = 0 & \text{if } Beam = No \end{cases} \quad (4.4)$$

4.2.2 Radiative Cooling (Rd)

Radiative cooling occurs due to heat transfer by thermal radiation carried by electromagnetic waves [51]. In vacuum, or in materials that allow the transmission of electromagnetic waves, radiation cooling is often dominant with respect to other cooling effects. Radiative cooling is a surface effect, and it depends on the surface characteristics. It strongly varies with the instantaneous absolute temperature. The net temperature variation from a surface S at a temperature T to a surrounding large enclosure at temperature T_0 can be described by Stephan-Boltzman's law:

$$\left(\frac{\partial T}{\partial t}\right)_{Rad} = \frac{S \cdot \sigma_{SB} \cdot \epsilon(T) \cdot (T(x, y, t)^4 - T_0^4)}{Cp(T) \cdot V \cdot \rho(T)} \quad (4.5)$$

where σ_{sb} is the Stephan-Boltzmann constant. The material emissivity ϵ is a measure of the efficiency with which a surface emits thermal energy and is defined as the ratio of the energy radiated from a material's surface to that radiated from a perfect emitter, known as black-body. A more detailed description of the emissivity can be found in Chapter 6.

4.2.3 Conduction Cooling (Cd)

Thermal conduction in solids or static fluids [**ref:ConductionCooling**] occurs as soon as a spatial temperature gradient exists. The carriers of the energy transfer can be molecules, atoms, electrons and phonons. The rate of change due to conduction can be described by Fourier's equation as follows:

$$\left(\frac{\partial T}{\partial t}\right)_{Cond} = \alpha(T) \left(\frac{\partial^2 T}{\partial x^2} + \frac{\partial^2 T}{\partial y^2}\right) \quad (4.6)$$

$\alpha(T)$ is called the thermal diffusivity of the medium and it measures the rate of heat transfer in a material from the hot end to the cold end. It has SI units of m^2/s . It can be calculated as:

$$\alpha(T) = \frac{k(T)}{\rho(T)C_p(T)} \quad (4.7)$$

in which $k(T)$ is defined as the thermal conductivity of the material (W/mK) and indicates the capability of the material to conduct heat. In general, metals have high thermal conductivity and gases have low thermal conductivity.

4.2.4 Thermionic Cooling (Th)

Thermionic emission, introduced in Section 3.1.3, is a process by which free electrons are emitted from the surface of a metal when they gain enough thermal energy to overcome the work function. These thermionic electrons take with them some energy, and thus contribute to the thermal cooling [52]. The temperature variation due to thermionic emission can be described as:

$$\left(\frac{\partial T}{\partial t}\right)_{Th} = S \cdot (\phi + 2K_B T) \cdot \frac{J_{Th}(T)}{C_p(T) \cdot V \cdot \rho(T)} \quad (4.8)$$

where ϕ is the work function of the material. K_B is Boltzmann constant. $J_{th}(T)$ was described in Sec. 3.1.3 can be written as:

$$J_{th}(T) = A_R \cdot T^2 \cdot \exp\left(-\frac{\phi}{K_B T}\right) \quad (4.9)$$

4.2.5 Sublimation Cooling (Sub)

Sublimation is a process in which a solid changes into a gas without passing through the liquid phase. To sublimate a substance, certain energy must be provided. We will call this energy H_{sub} , and it must be sufficient to break the intermolecular forces holding the solid together. Usually it is expressed in (KJ/mol) and its value can be found in the literature. Similar to the thermionic case, the newly formed gas molecules will escape the material, and the energy given to them for transforming their estate contributes to the overall cooling of the detector [53]. Sublimation cooling can be written as:

$$\left(\frac{\partial T}{\partial t}\right)_{Sub} = H_{sub} \cdot n(T) \quad (4.10)$$

in which $n(T)$ is the material sublimation rate. Following the same procedure as [54], one can determine an upper limit of the sublimation rate. To do so, one needs to assume the following:

- No atoms leaving the boundary layer return to the hot surface.
- A thin boundary layer over the hot material surface is at equilibrium with the substance sublimation pressure (P_{vap}) for temperature T_{vap} .
- This thin layer of gas is considered to be an ideal gas.

With these approximations, the amount of sublimated material per unit of time can be expressed as:

$$d_{sub} = \frac{1}{2} v_{vap} \cdot \rho_{vap} / \rho \quad (4.11)$$

v_{vap} is the velocity of the vapor particles and ρ the density of the material. According to the ideal gas theory, the average velocity of gas particles in a hemisphere can be described as follows:

$$v_{vap} = \frac{1}{2} \cdot \sqrt{\frac{8k_B T_{vap}}{m\pi}} \quad (4.12)$$

where m is the mass of the material particle. In addition, ρ_{vap} in Eq. 4.11 refers to the vapor density in the equilibrium layer and can be expressed as:

$$\rho_{vap} = \frac{m_{mol} T_{std}}{V_{mol} P_{atm}} \cdot \frac{P_{vap}(T_{vap})}{T_{vap}} \quad (4.13)$$

where P_{atm} is the atmospheric pressure (10^5 Pa) and $V_{mol} = 22.4 \text{ dm}^3$ the molar volume of an ideal gas at the standard temperature $T_{std} = 273$ K. The vapor pressure highly depends on the maximum temperature of the material, and consequently also the total amount of sublimated material.

4.3 Numerical Approximation to the heat equation.

Putting together all the concepts from the previous section, we can re-write Eq. 4.1 as follows:

$$\begin{aligned} \left(\frac{\partial T}{\partial t} \right)_{Tot} = & \frac{N(x, y, t)}{V \cdot Cp(T) \cdot \rho(T)} \cdot \frac{dE}{dx} \\ & - \frac{S \cdot \sigma_{SB} \cdot \epsilon(T) \cdot (T^4 - T_0^4)}{Cp(T) \cdot V \cdot \rho(T)} - \alpha(T) \left(\frac{\partial^2 T}{\partial x^2} + \frac{\partial^2 T}{\partial y^2} \right) \\ & - S \cdot (\phi + 2K_B T) \cdot \frac{J_{Th}(T)}{Cp(T) \cdot V \cdot \rho(T)} - H_{sub} \cdot n(T) \end{aligned} \quad (4.14)$$

This is an evolutionary, non-linear, second order, partial differential equation (PDE). In this work, this equation is treated numerically. Different numerical techniques to solve non-linear or quasi-linear PDEs exist. For a comprehensive introduction to this field, enough to understand the basics of the techniques can be found in [55].

In this document, we will focus on the classical theory of finite differences, based on the idea of replacing derivatives with linear combinations of discrete function values. One assumes the numerical solution is known only at a finite number of points (or nodes) in the physical domain. Fig. 4.3 shows an example of the spatial discretization of a homogeneous body.

The parameters Δx and Δy indicate the local distance between adjacent points in space, and in our case, they are considered to be uniform throughout the mesh. Increasing the number of nodes in the mesh (reducing $\Delta x, \Delta y$) increases the resolution and the accuracy of the numerical solution. However, it increases computational costs.

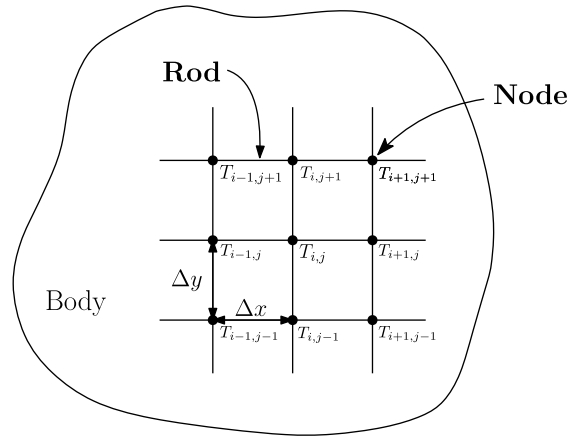


Figure 4.3: Space discretization of a homogeneous body.

Every node in the grid has a temperature and can exchange heat with its neighbors through a heat conducting rod. The sub-indexes i, j refer to nodes in the physical space. $T_{i,j}$ refers to the temperature in the position x_i, y_j .

Because the temperature of the system changes as function of time, the numerical solution of the PDE requires also time discretization. Fig. 4.4 shows a schematic representation of the time discretization of a strip of material. The time nodes are referred to with the super-index m , so that T^m corresponds to the temperature at the time instant t^m . Δt refers to the difference between time nodes. This distance was also considered to be equidistant, however, two different time constants were considered, one for the heating time (Δt_{heat}) and one for the cooling period (Δt_{Coold}). In most applications, the beam of particles is pulsed, and the beam pulse length is much shorter than the period without beam (i.e. the particles time distribution has a duty factor much smaller than 1).

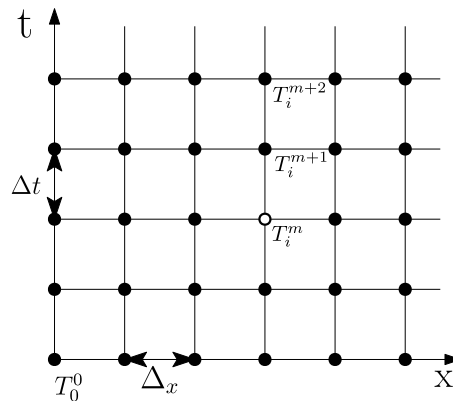


Figure 4.4: Time discretization of the material rod.

4.3.1 Finite Differences Schemes

Working with the full heat equation (Eq. 4.14) can result in a very cumbersome notation. The one-dimensional case of a thin rod with only radiative and conduction cooling will be considered for this explanation. The resulting simplified equation is:

$$\frac{\partial T(x, t)}{\partial t} = H(x, t, T) - A(T) (T(x, y)^4 - T_0^4) - \alpha(T) \frac{\partial^2 T(x, t)}{\partial x^2} \quad (4.15)$$

where $H(x, t)$ refers to the heating term. $A(T)$ can be written as:

$$A(T) = \frac{S \cdot \sigma_{SB} \cdot \epsilon(T)}{Cp(T) \cdot V \cdot \rho(T)}. \quad (4.16)$$

At any instant of time, one has access only to the values of the temperature at the aforementioned nodes (T_{ij}^m). The objective now is to obtain an approximation of $\partial T/\partial t$, $\partial^2 T/\partial x^2$ and $\partial^2 T/\partial y^2$ in those nodes by only knowing the information provided by the other nodes. Using different combinations of the mesh points results in different schemes. In the following, three of these schemes will be introduced. For a more detailed description of these methods can be found in [56].

Forward in Time, Centered in Space (FTCS)

This scheme approximates the time derivative with a forward difference:

$$\left. \frac{\partial T}{\partial t} \right|_{t^{m+1}, x_i} = \frac{T_i^{m+1} - T_i^m}{\Delta t} + \mathcal{O}(\Delta t) \quad (4.17)$$

And for $\partial^2 T/\partial x^2$ a central difference approximation is used.

$$\left. \frac{\partial^2 T}{\partial x^2} \right|_{x_i} = \frac{T_{i-1}^m - 2T_i^m + T_{i+1}^m}{\Delta x^2} + \mathcal{O}(\Delta x^2) \quad (4.18)$$

The expression $\mathcal{O}(\Delta t)$ means that the local truncation error is in this case proportional to the time step size, while $\mathcal{O}(\Delta x)$ indicates that the truncation error reduces quadratically with the spatial step size.

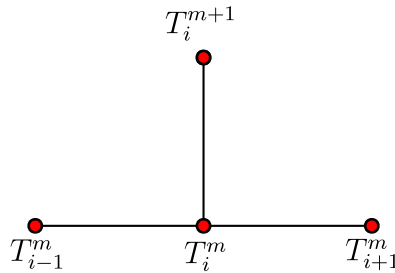


Figure 4.5: Stencil for the Forward Time, Central Space finite difference method.

The stencil of this method can be found in Fig. 4.5. This method calculates the state of the system at a later time from the state of the system at the current time. It is considered to be an explicit method. Introducing these approximations in Eq. 4.15 one obtains:

$$\frac{T_i^{m+1} - T_i^m}{\Delta t} = H_i^m - A_i^m ((T_i^m)^4 - (T_0)^4) + \alpha_i^m \frac{T_{i-1}^m - 2T_i^m + T_{i+1}^m}{\Delta x^2} \quad (4.19)$$

After a little bit of algebra, this equation can be written in a matrix form:

$$\begin{bmatrix} 1 & 0 & 0 & 0 & 0 & 0 \\ r_1^m & (1-2r_1^m) & r_1^m & 0 & 0 & 0 \\ 0 & r & (1-2r_1^m) & r_1^m & 0 & 0 \\ 0 & 0 & \ddots & \ddots & \ddots & 0 \\ 0 & 0 & 0 & r_1^m & (1-2r_1^m) & r_1^m \\ 0 & 0 & 0 & 0 & 0 & 1 \end{bmatrix} \begin{bmatrix} T_0^m \\ T_1^m \\ T_2^m \\ \vdots \\ T_{N-1}^m \\ T_N^m \end{bmatrix} = \begin{bmatrix} T_0^{m+1} + g(T_0^m) \\ T_1^{m+1} + g(T_1^m) \\ T_2^{m+1} + g(T_2^m) \\ \vdots \\ T_{N-1}^{m+1} + g(T_{N-1}^m) \\ T_N^{m+1} + g(T_N^m) \end{bmatrix}$$

with $r_i^m = \alpha_i^m \cdot \Delta t / \Delta x^2$ and where $g(T)$ includes all the non-linear terms of the equation. In a more simplified way:

$$D_{FTCS} \cdot T^m = T^{m+1} + g(T^m) \quad (4.20)$$

This is a relatively simple method to implement, as the values of T_i^{m+1} can be updated independently of each other. However, the FTCS method can yield unstable solutions that can oscillate and grow if Δt is too large. To ensure stability (see also [57] and [58]):

$$r = \alpha \cdot \frac{\Delta t}{\Delta x} < \frac{1}{2} \quad (4.21)$$

Backwards in Time, Centered Space (BTCS)

In this case, a backward in time difference is used to approximate the time derivative while a central space scheme is used for the spatial derivative:

$$\left. \frac{\partial T}{\partial t} \right|_{t^{m+1}, x_i} = \frac{T_i^m - T_i^{m-1}}{\Delta t} + \mathcal{O}(\Delta t) \quad (4.22)$$

As in the previous case, the full equation can be represented in a matrix form:

$$\begin{bmatrix} b_0 & c_0 & 0 & 0 & 0 & 0 \\ a_1 & b_1 & c_1 & 0 & 0 & 0 \\ 0 & a_2 & b_2 & c_2 & 0 & 0 \\ 0 & 0 & \ddots & \ddots & \ddots & 0 \\ 0 & 0 & 0 & a_{N-1} & b_{N-1} & c_{N-1} \\ 0 & 0 & 0 & 0 & a_N & b_N \end{bmatrix} \begin{bmatrix} T_0^m \\ T_1^m \\ T_2^m \\ \vdots \\ T_{N-1}^m \\ T_N^m \end{bmatrix} = \begin{bmatrix} d_0 + g(T_0^m) \\ d_1 + g(T_1^m) \\ d_2 + g(T_2^m) \\ \vdots \\ d_{N-1} + g(T_{N-1}^m) \\ d_N + g(T_N^m) \end{bmatrix}$$

Where the coefficients are:

$$\begin{aligned} a_i &= -r_{i-1}^m \\ b_i &= 1 + 2r_i^m \\ c_i &= -r_{i+1}^m \\ d_i &= T_i^{m-1} + g(T_i^m) \end{aligned} \quad (4.23)$$

Fig. 4.6 shows the stencil representation of this method. In this case, we are dealing with an implicit method. To find the temperature in the time step m one must solve an equation involving the current state of the system (m) and the previous state ($m-1$).

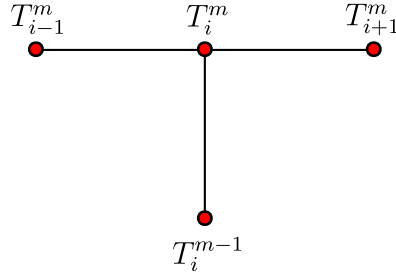


Figure 4.6: Stencil for the Backwards in time, Central in space finite difference method.

Crank-Nicolson

To improve the temporal truncation error, the Crank-Nicolson scheme approximates the spatial derivative by the average of the central difference scheme, evaluated in the current (m) and the previous ($m - 1$) time steps:

$$\frac{T_i^m - T_i^{m-1}}{\Delta t} = g(T_i^m) + \frac{\alpha_i^m}{2} \left[\frac{T_{i-1}^m - 2T_i^m + T_{i+1}^m}{\Delta x^2} + \frac{T_{i-1}^{m-1} - 2T_i^{m-1} + T_{i+1}^{m-1}}{\Delta x^2} \right] \quad (4.24)$$

The stencil representation of this method is shown in Figure 4.7. This method is implicit, like the BTCS method. However, it accomplishes a truncation error $\mathcal{O}(\Delta t^2)$ without over complicating the implementation. The matrix representation is the same as in the BTCS case, but with the following coefficients:

$$\begin{aligned} a_i &= -r_{i-1}^m/2 \\ b_i &= 1 + r_i^m \\ c_i &= -r_{i+1}^m/2 \\ d_i &= a_i T_{i-1}^{m-1} + (1 + a_i + c_i) T_i^{m-1} + c_i T_{i+1}^{m-1} + g(T_i^m) \end{aligned} \quad (4.25)$$

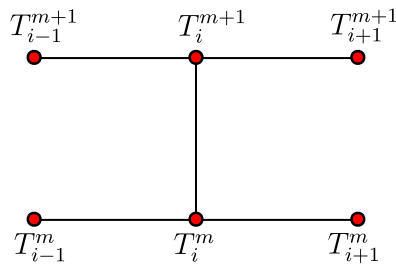


Figure 4.7: Stencil for the Crank-Nicolson finite difference method.

4.3.2 Initial and Boundary Conditions

Due to the time-dependent part of our equation, we need an initial condition, i.e. the temperature of the system at time t^0 . Unless specified otherwise, a constant temperature $T_{i,j}^0 = 300(K)$ will be considered.

At each time step, because of the spatial dependence of the equation, some boundary conditions need to be specified. Here the so-called Dirichlet boundary

conditions are considered. For the one-dimensional case, these conditions can be written as follows:

$$\begin{cases} T(0, t) = 300 & (K) \\ T(L, t) = 300 & (K) \end{cases} \quad (4.26)$$

Where L refers to the length of the one-dimensional rod. In the 2D case, these conditions indicate that all the borders of the foil are in contact with a thermal sink at 300 (K).

4.3.3 The Non-Linear Problem

In the previous sections, $g(T)$ was described as the non-linear term. The explicit expression is:

$$g(T) = \frac{N(x, t)}{V \cdot Cp(T) \cdot \rho(T)} \frac{dE}{dz} - \frac{S \cdot \sigma_{SB} \epsilon(T) \cdot (T(x, t)^4 - T_0^4)}{V \cdot Cp(T) \cdot \rho(T)} \quad (4.27)$$

In the case with no heating and no radiative cooling, $g(T) = 0$. This case yields to the diffusion equation. In such a scenario, the systems of equations presented in the previous section can be easily solved by techniques like Gaussian elimination methods, LU factorization, etc. More information about those methods can be found in [59].

$g(T) \neq 0$ implies that, at each time step, one has to solve a system of non-linear equations. This is still solvable numerically, but it implies using other numerical techniques such as Newton's method for non-linear systems [59]. At every time step, one must guess an approximate solution and compute the Jacobian matrix, which can be computationally expensive and cumbersome. By default, instead of considering the full equation, each term of the equation is considered separately and then added together. For Eq. 4.15 this would mean solving the following:

$$\frac{\partial \Delta T_{Ht}(x, t)}{\partial t} = H(x, t, T) \quad (4.28)$$

$$\frac{\partial \Delta T_{Rad}(x, t)}{\partial t} = A(T) (T(x, y)^4 - T_0^4) \quad (4.29)$$

$$\frac{\partial \Delta T_{Con}}{\partial t} = \alpha(T) \frac{\partial^2 T(x, t)}{\partial x^2} \quad (4.30)$$

The total temperature variation is then calculated as:

$$\Delta T_{tot} = \Delta T_{Ht} - \Delta T_{Rd} - \Delta T_{Con} \quad (4.31)$$

4.4 The two-dimensional problem

The biggest difference in the two-dimensional case is the conduction term on the heat equation. Each point in space is now connected to four other points, which means assuming conduction along four rods. For the two-dimensional case, a five-point finite difference formulation is used [56]. Taking the simplified case of the 2D diffusion equation:

$$\frac{\partial T(t, x, y)}{\partial t} = \alpha(T) \left(\frac{\partial^2 T}{\partial x^2} + \frac{\partial^2 T}{\partial y^2} \right) \quad (4.32)$$

One could write the FTCS formulation as follows:

$$\frac{T_{i,j}^{m+1} - T_{i,j}^m}{\Delta t} = \alpha(T_{i,j}^m) \left(\frac{T_{i-1,j}^m - 2T_{i,j}^m + T_{i+1,j}^m}{\Delta x^2} + \frac{T_{i,j-1}^m - 2T_{i,j}^m + T_{i,j+1}^m}{\Delta y^2} \right) \quad (4.33)$$

Similarly, this could be applied to the BTCS and Crank-Nicolson formulations. The same procedure to transform this into a system of equations, and solve it numerically, can also be followed.

4.5 Importance of Cooling Effects

The most accurate simulation is obtained when all the cooling mechanisms indicated in Eq. 4.1 are considered. However, if simulation speed is what matters, a faster simulation can be run by ignoring certain cooling mechanisms. Particularly, conduction cooling is the most time-consuming effect. Fig. 4.8 shows how much each cooling mechanism contributes to the total cooling as a function of the temperature. This figure was calculated for a 30 μm Graphite wire. It might differ slightly for different materials and geometries.

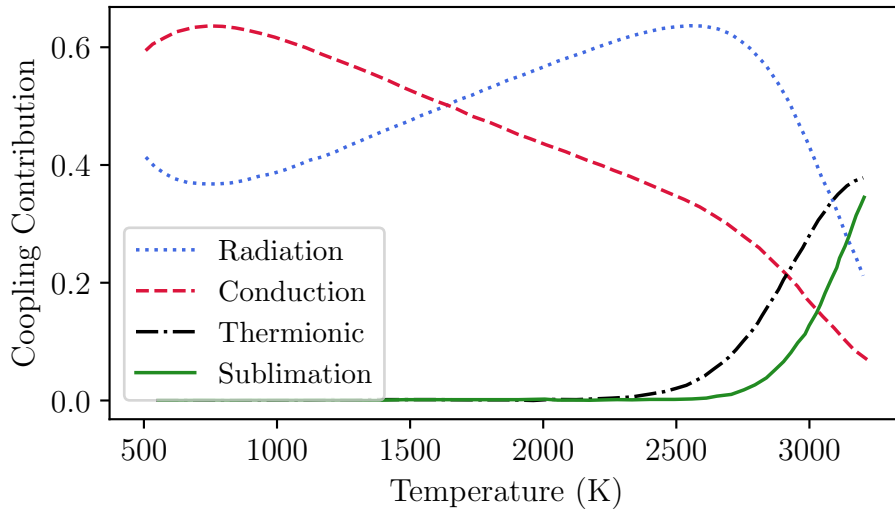


Figure 4.8: Relative importance of the different cooling mechanisms as a function of the temperature.

From this figure, one can observe how radiation cooling is the predominant mechanism throughout the biggest temperature range. For a thin wire, conduction cooling plays a very important role at lower temperatures while thermionic and sublimation cooling are important only at very high temperatures. If there is some a-priori knowledge of the expected temperature range, or simply a fast upper limit of the maximum temperature is needed, various cooling processes can be deliberately eliminated for speed purposes.

4.6 PyTT

All the concepts and models described above were wrapped up in a comprehensive simulation program written in Python 3.6.9. The latest version of the code can be found in the *git* repository under the project label *PyTT* [60]. As aforementioned, the main objective of this code is to quickly obtain an estimation of the maximum temperature reached by thin target detectors when interacting with the beam of particles. Additionally, the code also needed to be easy to use by people who aren't particularly familiar with python or numerical techniques. For that, a user-friendly interface was implemented.

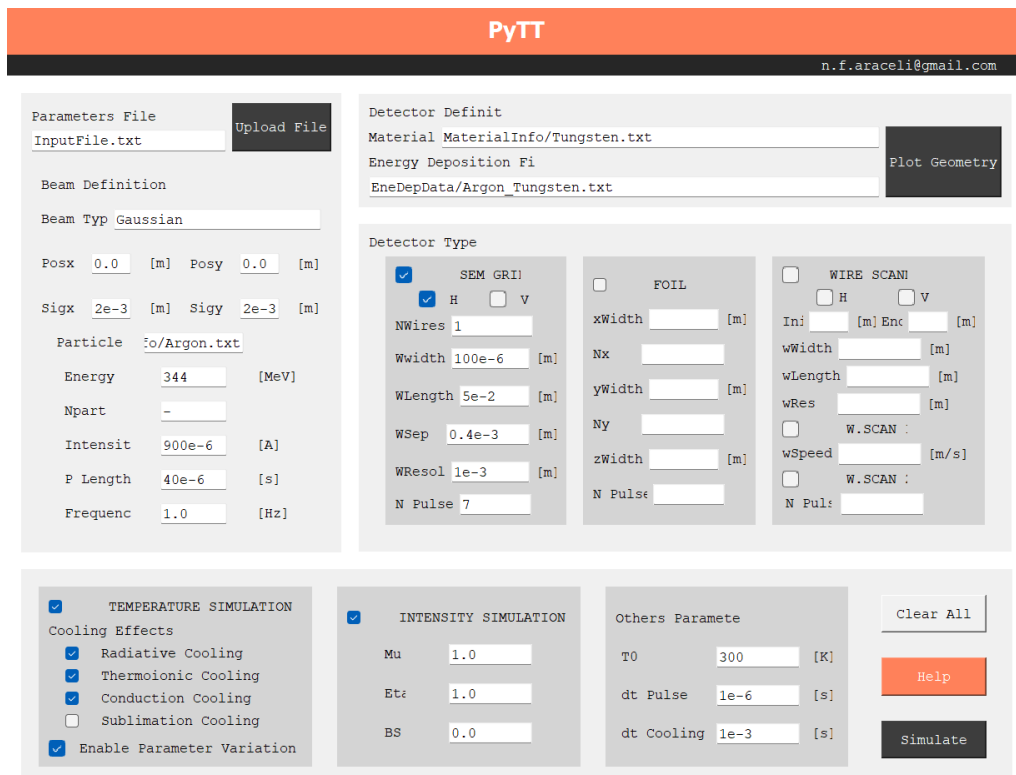


Figure 4.9: Graphical User-Friendly interface of PyTT code.

Fig. 4.9 shows a screenshot of the GUI. Without going into the details of the SW implementation, a general description and the main functionalities of *PyTT* are reported here below.

1. *Variety of Beam Conditions*: the program allows the user to choose several beam parameters. For example, the particle or ion type and energy, the spatial and temporal distribution, and the repetition frequency of the particle beam.
2. *Variety of Detector Materials*: the material of the detector can be chosen among a default predefined list or by defining a new one.
3. *Type of thin target detectors*: the program can simulate wire grids, thin foils and wire scanners. For the wire scanners, both fast and slow wire scanners can be considered.

4. *Simulation Parameters*: several simulation parameters (Such as space-time discretization parameters, simulation length, thermal effects, parameter temperature dependence, etc.) can be easily selected at the user's convenience.
5. *Intensity Simulation*: the program includes an intensity simulation module based on the theory and assumptions explained in Ch. 3. This module calculates the current generation in the detector during operation.

Results like the maximum temperature in the detector as a function of time are provided by default. Figure 4.10 shows an example of the simulated output. The output files produced by the simulation include spatial thermal distributions, the relative importance of the different cooling methods, the evolution of material properties during simulation, intensity distribution, etc.

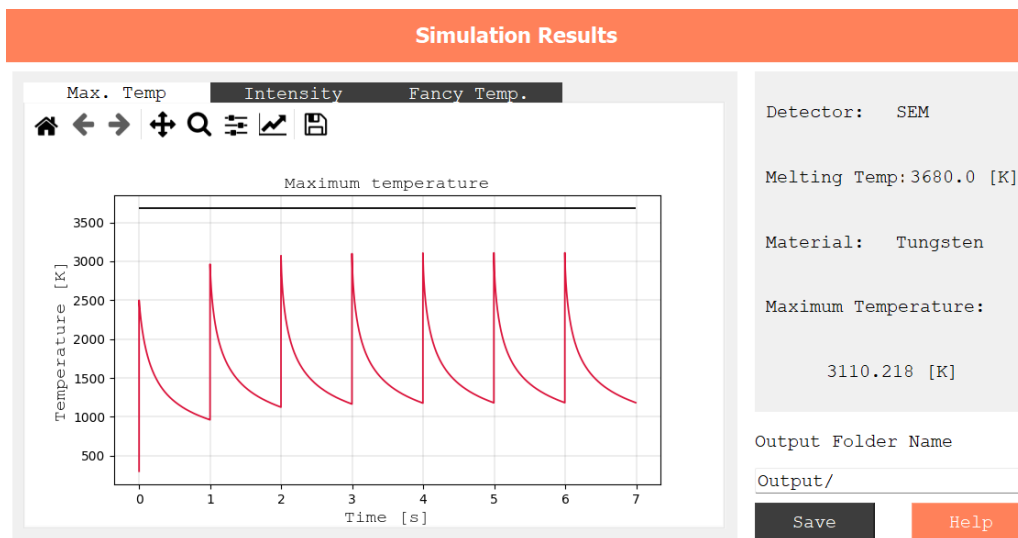


Figure 4.10: Example of output visualization GUI.

The program has been optimized for it to be used by the python interface. However, it can also be launched by a stand-alone executable for windows systems. It can also be used without the GUI, which allows for easy paralelization and automatization. A more detailed description of how to use the code can be found in the user manual, accessible through the help button in the GUI, or directly in the HelpFolder.

4.7 Model uncertainties

This section will summarize the model uncertainties, which at first depend on the initial knowledge of the simulation case and the related input parameters. One can divide these parameters into two categories: Beam Parameters and Material Properties.

4.7.1 Beam Parameter Uncertainties

The beam input parameter can be usually summarized as beam size (σ_x, σ_y for Gaussian distributions), position, intensity, pulse length, repetition rate, etc.

Each simulation case has different beam parameters and the knowledge of these parameters is also dependent on the simulation case.

Let's take as an example a simulation performed for the LINAC4 accelerator. First, a specific case is simulated and considered to be the average. The beam parameters of this average case are summarized in table 4.1. All these parameters were varied independently up to a $\pm 30\%$ of their average value (Parameter Rel. Error) and the relative error of the simulation was calculated in each case with respect to the average solution.

Energy (MeV)	Intensity (mA)	Pulse Length (us)	σ_x (mm)	σ_y (mm)
160	25	100	1.0	1.0

Table 4.1: Beam parameters used for uncertainty calculations. Average case example.

Fig. 4.11 shows how in this case uncertainties in the beam parameters affect the final temperature simulated results. The dependency of the uncertainties for the intensity and the beam pulse length is identical and linear. The beam heating and cooling is dependent on how many particles (per unit time) reach the material (N_{Tot}). Variations in both, intensity and beam pulse length, affect N_{Tot} , which variation yields the linear response in the uncertainties.

The uncertainty of the beam size has a greater impact than the uncertainty of the final result. One can also observe a non-linear and non-symmetrical response in the induced uncertainties. Because the beam size is introduced in the model as a $1/\sigma^2$ factor, changes in the beam size are more considerable for smaller beam sizes.

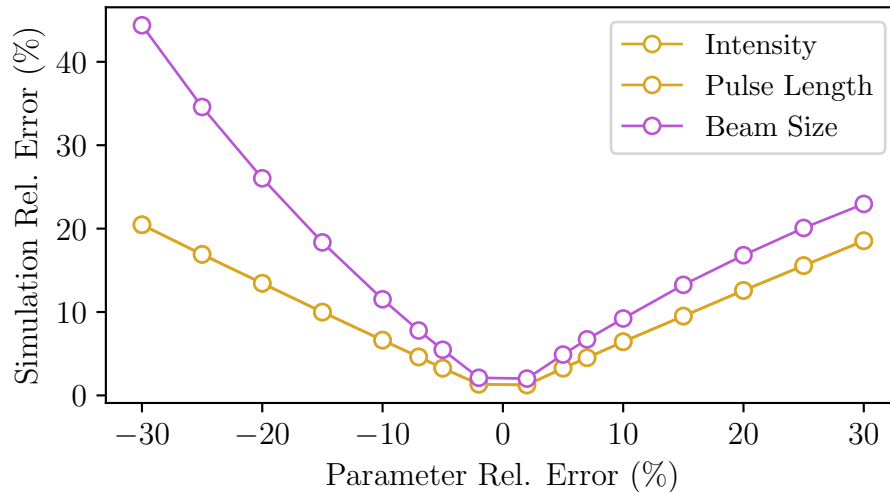


Figure 4.11: Effects of beam parameter uncertainties on maximum temperature simulation results.

It is difficult to give a specific value of the Beam parameters uncertainty, as it is very much dependent on the simulation case. If the range of confidence of the simulation studies is necessary for a certain application a proper study of the Beam parameter uncertainties should be carried out.

4.7.2 Material Parameter Uncertainties.

The material parameters used as input for the simulations are listed in Table 4.2. Some of them are perfectly known (as Atomic number and mass) and others often well known from literature (see for example metallic and non-metallic properties of solids in [61]).

Property	Abbreviation	Units
Atomic Number	Z	
Atomic Mass	A	amu
Density	rho	g/cm ³
Melting Point	Mp	K
Work Funktion	phi	eV
Emissivity	eps	
Specific Heat	Cp	J/gK
Conductivity	k	W/mK

Table 4.2: Material parameters necessary for thermal simulations.

Similarly to the beam parameter case, Fig. 4.12 shows how material parameters uncertainties propagate to the error on the maximum temperature prediction. In this case, one can observe how the parameter that induces the highest uncertainty is the specific heat (Cp). To give a numerical example of typical uncertainty values we studied the Graphite and the Tungsten case.

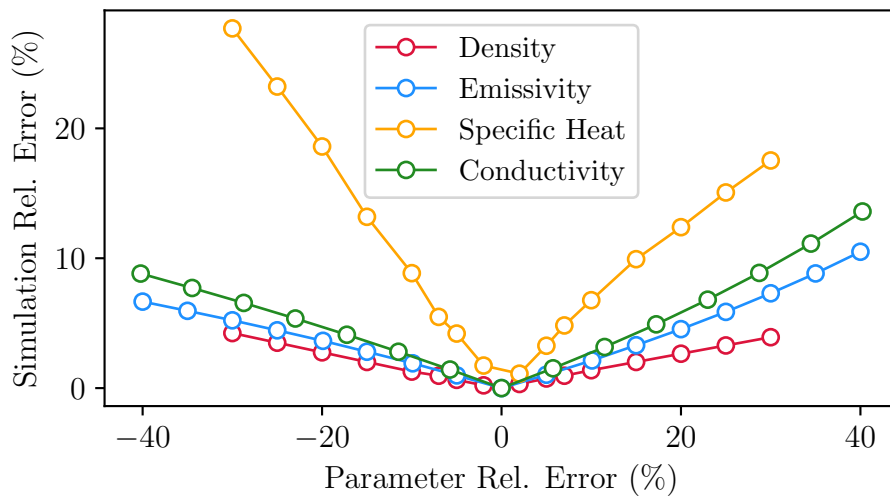


Figure 4.12: Effects of material property uncertainties on maximum temperature results.

Fig. 4.13 shows the uncertainties for specific heat, emissivity and thermal conductivity parameters for Tungsten and Graphite. In this case, the uncertainties for the other parameters were negligible. The central points on the boxes represent the average property value, while the limits of the colored boxes represent the RMS. The error bars represent the maximum and minimum discrepancies found with respect to the average value.

Uncertainties of the Specific heat are quite small (2.83%) for both graphite and tungsten. In the case of graphite, values for the emissivity seem to be quite well

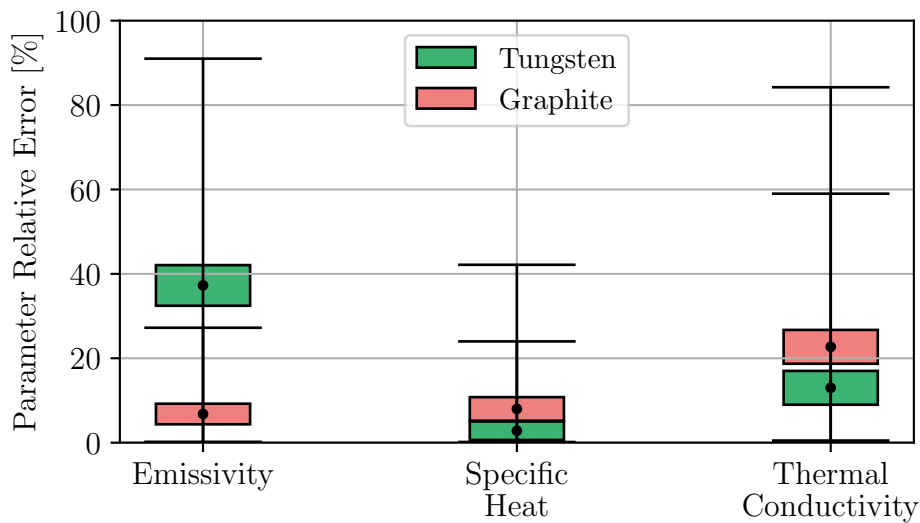


Figure 4.13: Material property uncertainties for Graphite and Tungsten.

known (6.75%). Contrarily, a much higher uncertainty was found in the case of its thermal conductivity (22.71%). In the case of tungsten, we find the opposite situation, different sources seem to agree on the value of the thermal conductivity (13.0%), however, big uncertainties are found in the emissivity case (43.26%).

The meaningful uncertainty in the tungsten emissivity led to in-depth studies and experiments that will be presented in Chapter 6.

Chapter 5

Simulation Benchmarking and Applications

In this chapter, the first two sections present a series of studies for benchmarking the PyTT simulation tool. This includes dedicated measurements performed at LINAC4 in which the thermal evolution of the detectors was indirectly measured and compared to the simulations. These measurements were published in [62]. Then, we present a comparison between the thermal evolution (for thin wires and thin foil) simulated with PyTT and the commercially available software ANSYS. The last part presents three examples of how the PyTT software has been useful for CERN operation. In particular, we show how the PyTT code has been used to calculate beam power limits at LINAC4 and SPS accelerators.

5.1 Thermionic Measurements at LINAC4

The best way to crosscheck the reliability of the thermal evolution simulations introduced in the previous chapter is to compare them with experimental measurements. Many techniques have been developed for measuring the temperature evolution in objects [63]. In our particular case, we were interested in measuring experimentally the temperature evolution of thin wires ($40\mu m$) during their interaction with the particle beams. Without the possibility of installing a dedicated setup in a CERN facility, the signal generated on LINAC4 wire based detectors and the knowledge of thermionic emission processes were used to estimate wire temperature during operation.

As explained in Ch. 2, and then in Section 3.1.3, Thermionic emission current (J_{th}) is negligible at low temperatures but it becomes considerable when higher temperatures are reached. The dedicated measurements were based on increasing in a controlled way the beam power and observe the onset of thermionic emission.

From the relationship between the thermionic current and the temperature, by comparing the simulated current and the experimentally measured one, we could judge the reliability of our thermal simulation results.

5.1.1 Experimental setup and preparation

For normal beam conditions, the currents measured by the individual wires in SEM grid, or the single wire in a Wire Scanner, are around 1 (mA). For the exper-

imental planning, a signal was considered detectable if the thermionic current was higher than 0.05 (mA). Fig. 5.1 shows the expected current generated, by thermionic emission, in a Tungsten ($40\mu\text{m}$) and a Graphite ($33\mu\text{m}$) wire as a function of the wire temperature. From this figure, one can observe that temperatures above 2100 (K) will be required to obtain a detectable thermionic current.

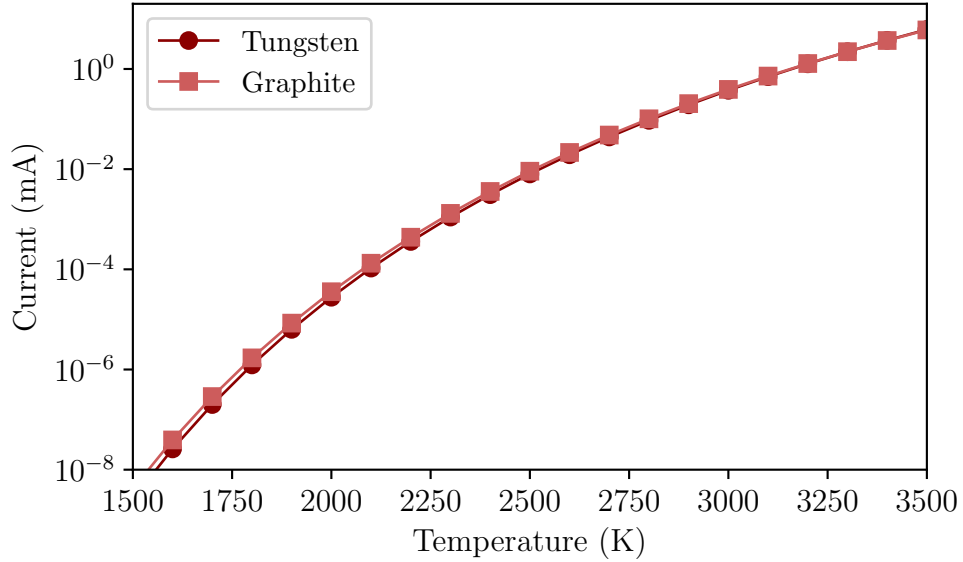


Figure 5.1: Thermionic current as a function of the temperature for Tungsten ($40\mu\text{m}$) and a Graphite ($33\mu\text{m}$) wires.

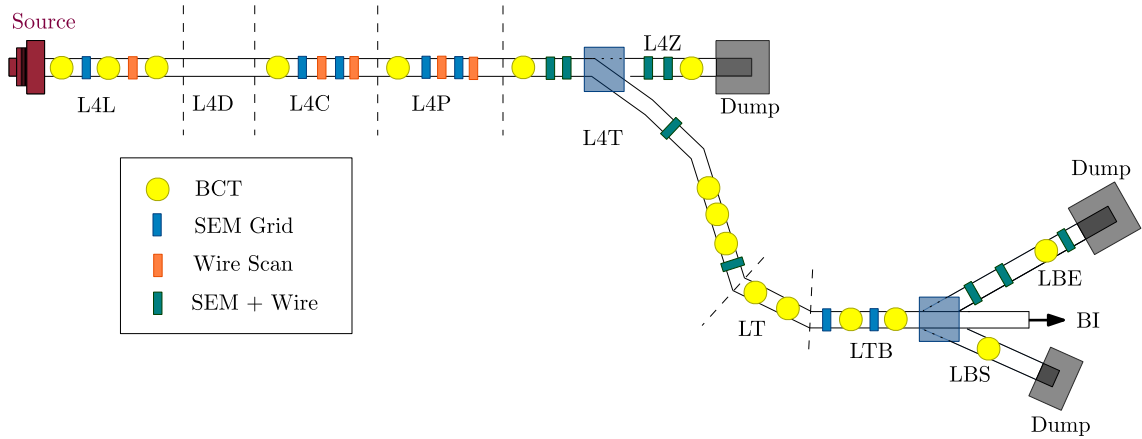


Figure 5.2: Schematic representation of Linac4 layout, with locations of the SEM Grid (L4T.BSGH/V.0243) and the BCT (L4T.BCT.0107) used for thermionic measurements.

By definition, the planned measurements were potentially destructive for the wires. For this reason the experiment was planned at the end of an operational year (i.e. before a planned shutdown period in which wire could be exchanged if necessary and preferably using detectors with already known damaged (i.e. to be repaired anyway).

Referring to Fig. 5.2, representing the L4T line at 160 MeV, it was decided to use the wire grid systems labelled as L4T.BSGH/V.0243. The beam current transformer

L4T.BCT.0107 was used for continuous intensity and pulse length measurements.

Pitch	# of Wires	Wire Distance (mm)	Covered Region (mm)
	6 + 6 = 12	0.4	4.4
	3 + 3 = 6	0.75	8.9
3	3+3 = 6	1.0	14.9
	2 + 2 = 4	2.5	24.9
	2 + 2 = 4	4.0	40.9

Table 5.1: Detailed description of wire location in SEM grid L4T.BSGH/V.0243

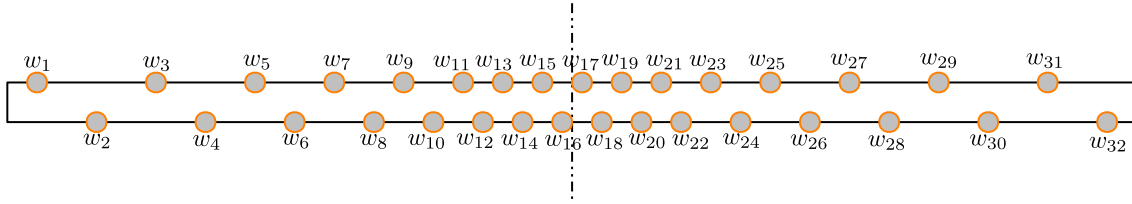


Figure 5.3: Schematic representation of wire position at L4T.BSGH/V.0243, as they are mounted on the ceramic support.

The wire grids used for the measurement were composed of 32 Tungsten wires with gold coating. The wires had a length of 5 (cm) and a thickness of 40 (μm). The wires were unevenly spaced, covering a total area of 40.9 (mm). Table 5.1 details the locations of the different wires. The wires were placed on the top and the bottom part of the (ceramic) supporting frame as shown in Fig. 5.3. This mounting scheme allows reaching a minimum wire distance of 0.4 mm (between wires sitting on opposite frame side), difficult to reach by mounting wires on one side only.

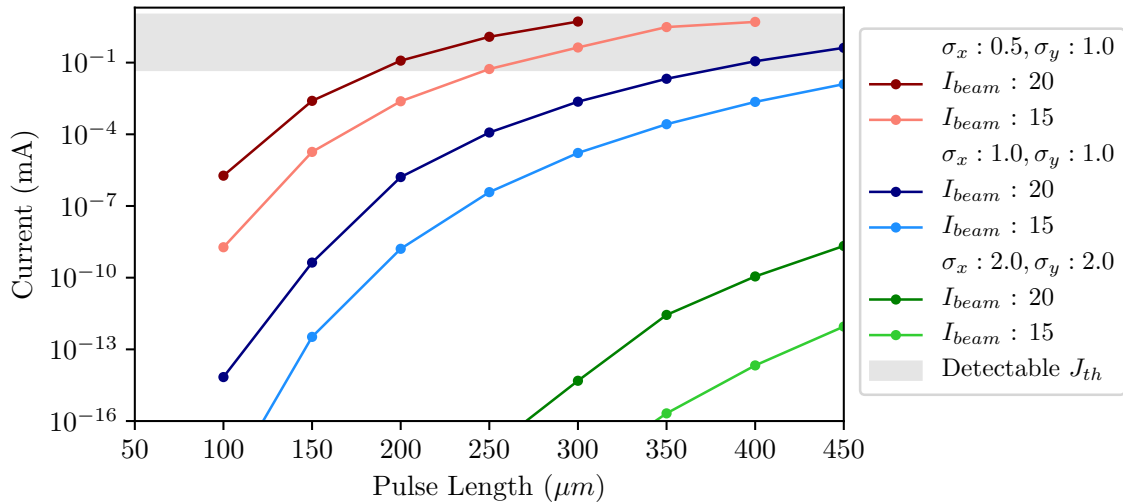


Figure 5.4: Summary of expected maximum current for different beam conditions. Gray Area indicates where thermionic emission is detectable. The beam size is given in (mm) and Beam intensity in (mA).

A preliminary study was performed to determine what kind of beam parameters would potentially yield a detectable thermionic current. In the L4T line, the energy

of the H^- beam of particles is already 160 MeV. The beam power then depends on: beam intensity (I_{beam}), beam pulse length (Δt), and beam size (σ_x, σ_y). Fig. 5.4 shows a summary of the maximum expected thermionic current for different beam conditions.

According to the model, relatively large beam sizes (e.g. $\sigma_x = \sigma_y = 2$ mm) do not yield to detectable thermionic emission. For smaller beam sizes (e.g. $\sigma_x \leq \sigma_y \leq 1$ mm), thermionic emission can be detected for beam pulse lengths $\Delta t > 300$ μs . Setting up the beam size to a specific dimension is not an easy task. Changes in the intensity of the beam also did not produce very dramatic changes in the detectable current. During the measurements, these two quantities were kept constant while the beam pulse length was increased in steps in order to reach the thermionic stage in a controlled way.

5.1.2 Experimental Results

The first set of measurements was taken using beam conditions expected to stay in a low temperature regime, i.e. below the onset of measurable thermionic emission. The intensity of the beam was kept constant to $I_{beam} = 17.30(17)$ mA. The beam size was $\sigma_x = 1.02(5)$ mm and $\sigma_y = 1.76(2)$ mm, with the beam centered at $\mu_x = -0.22(6)$ mm and $\mu_y = -0.43(21)$ mm. Fig. 5.5 shows the evolution of the beam size and position during a LINAC4 pulse. During these measurements, the beam pulse length was varied between $\Delta t = 165.38(48)$ μs up to $\Delta t = 247.12(33)$ μs . As expected, no sign of thermionic emission was observed. However, after the measurements with the longest pulses, we could observe that wires 15 and 17 (sitting on the same ceramic support side, see Fig. 5.3) were glued together. This can be inferred from Fig. 5.6 showing the current registered by the different wires of the grid as a function of time for four consecutive beam pulses. After the second pulse the two glued wires give the same signal. The most probable hypothesis for explaining the wire gluing is the successive occurrence of the following events:

- wire heating due to high power deposition and poor cooling (gold coating featuring low emissivity)
- loss of wire tension due to thermal expansion.
- melted gold coating acting as glue during the partial cooling in between beam pulses
- in later beam pulses, with not coated Tungsten cooling better, the maximum temperature was lower and the wires remained glued

In order to avoid this situation and proceed with more measurements, the beam of particles was steered away from the glued wires and centered around $\mu_x = -1.89(11)$ mm and $\mu_y = 1.15(31)$ mm. The wire separation in this position is larger, thus reducing the probability of wire gluing. The horizontal beam size was reduced to $\sigma_x = 0.59(17)$ mm and consequently the vertical size de-focused to $\sigma_y = 3.23(54)$ mm. During these measurements, the beam intensity was slightly smaller $I_{beam} \sim 16.7$ mA. The beam pulse length was increased systematically until thermionic emission was observed. On the vertical grid, thermionic emission was observable in various wires for a beam pulse length of ~ 450 μs .

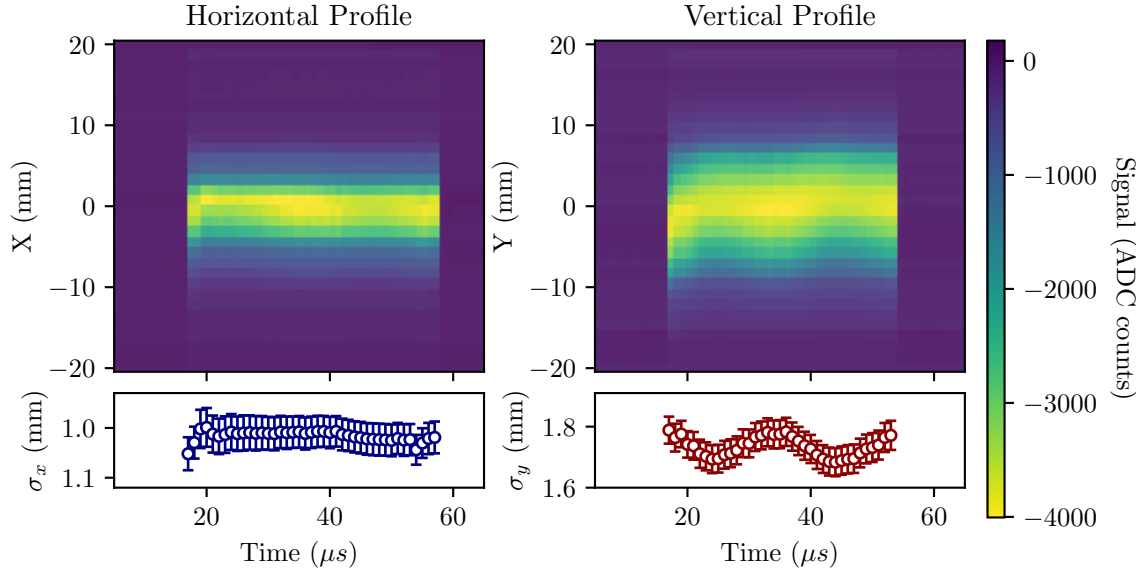


Figure 5.5: Evolution of the transverse beam profile along the beam pulse. Top: example of transverse beam profile measurement. Bottom: Calculated beam size from gaussian approximation. Error bars were calculated by measuring different beam pulses.

Fig. 5.7 shows the current measured by several wires in the vertical SEM grid during the beam passage. When the particles reached the detector a negative signal (from the stripped electrons stopping in the wire) is registered. During the pulse, the energy deposition in the detector material heat the wires. Thermionic emission (positive current in the wire) increases, thus contributing to the overall signals decrease.

Once the particle beam has disappeared, a small positive current remains. This is because the detector is still warm, thermionic emission current is still there. As the detector cools down, this current diminishes.

In Fig. 5.7 one can also observe some fluctuations in the registered beam current. This was an effect of the particle beam itself, and could also be observed in the BCT measurements.

It must be also noted that, at $t = 250\mu s$ and $t = 400\mu s$, the measured beam current drops on all wires. This comes from the real LINAC4 beam pulse structure. The low energy chopper, a very fast RF kicker, eliminates a parts of pulse to create short empty periods in which the injection system is switching the destination from one PSB ring to the other with minimum losses. This is also measured by the BCT.

The effects of thermionic emission can be also observed in the beam profile measurements. This is shown in Fig. 5.8. In this figure, lighter colors indicate profiles taken at larger times during the beam pulse. We can see how the beam profile measurements are affected by the thermionic current.

5.1.3 Measurement-Simulation Comparison

PyTT program was used to simulate the thermal and electrical evolution of the detectors during the measurements. For the simulations, the intensity of the beam was considered to be constant. Intra-pulse intensity fluctuations and chopper effects

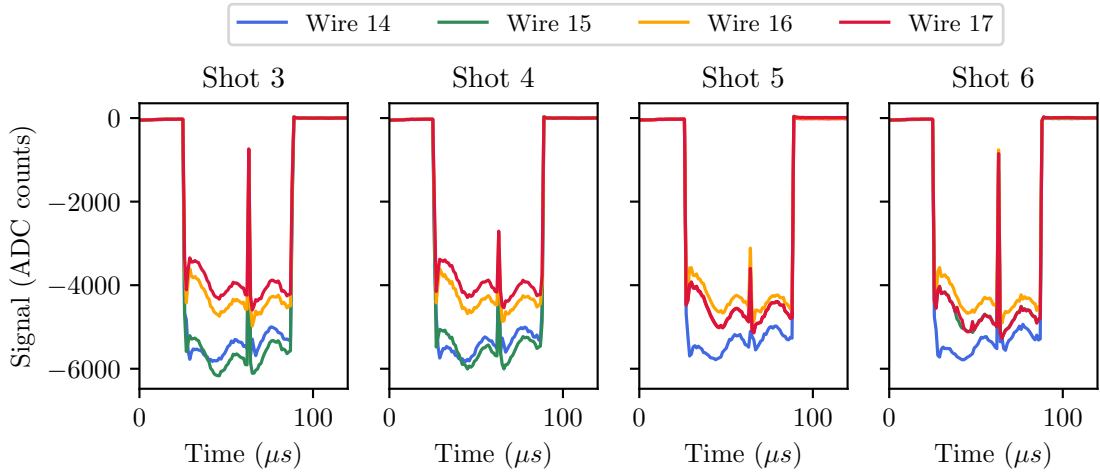


Figure 5.6: Evolution of the measured current in different wires as a function of time, for six consecutive beam pulses.

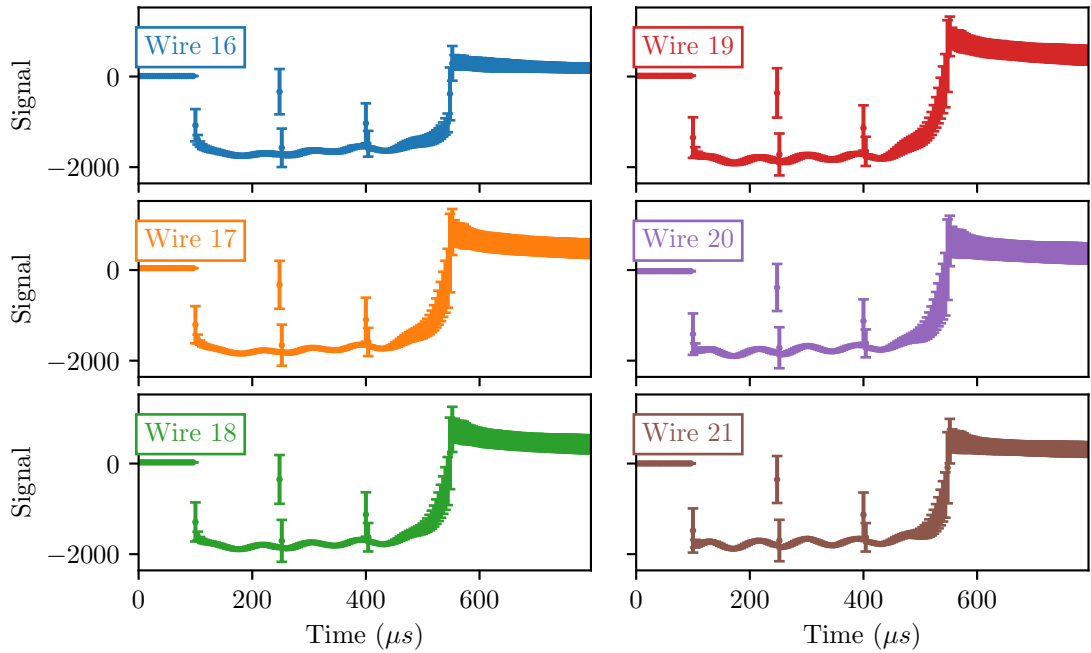


Figure 5.7: Current registered by several wires during the beam pulse. The units of the signals are (ADC counts).

were not considered. Fig. 5.9 shows a comparison between the signal measured by wire 19 of the SEM grid, the simulated current, and the current measured by BCT.0107. The BCT intensity has been included in the comparison to show the intrinsic properties of the beam. The BCT signal clearly shows when the Beam pulse starts and ends. It also shows the aforementioned beam intensity fluctuations and the chopper gaps. However, the current reduction at longer beam pulse time is not observable in the BCT measurements, as this is an effect occurring on the wire.

Also, the positive current used by the wire after the beam pulse has passed is not observable in the BCT signal. This means the current measured by the detector

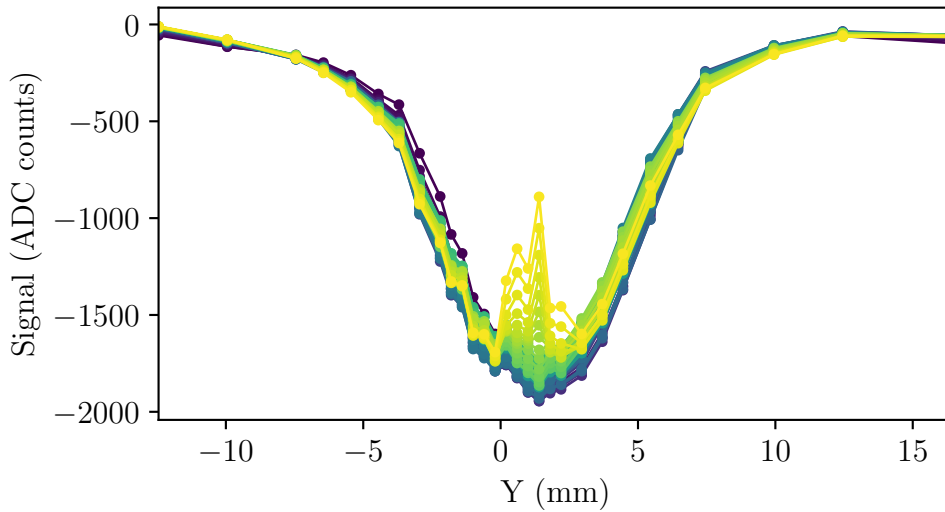


Figure 5.8: Example of vertical profile beam measurement. Darker colors indicate measurements at the beginning of the beam shot. Lighter colors indicate measurements at the end of the shot.

at that time does not come from the beam. The simulation results seem to very clearly reproduce the average of the measured SEM current. The simulations show a slightly slower start for the thermionic emission current. However, after the beam pulse is gone, the simulated and the measured results for the thermionic current match very well.

The maximum relative error between simulated and measured results is found to be around 30 %, and it is found at the very end of the beam shot. Even then, the average relative error along the whole pulse is 6.3(25)%.

A dedicated uncertainty study was performed to determine the uncertainties of the simulated results (See Sec. 4.7). In this particular case, the biggest contributor to the simulation's uncertainty came from uncertainties in the beam size. As indicated in the previous section, the beam size was $\sigma_x = 0.59(17)$ mm and $\sigma_y = 3.23(54)$ mm. This implies, beam size uncertainty was $\xi_x = 28.81\%$ and $\xi_y = 16.71\%$. As shown in Sec. 4.7, uncertainties in beam sizes can yield big uncertainties in simulation results, mainly when small beam sizes are involved.

As we saw in Fig. 5.7, several wires measured thermionic emission. However, due to the small changes in the measured intensity between the different wires and the big uncertainties in the simulated results, it was impossible to distinguish among them.

5.2 Simulation Comparison: Ansys

The objective of this study was to compare the results obtained with the PyTT code, with results obtained with Ansys, a highly used and benchmarked commercially available software.

For this work, the theory of finite differences (FDM) has been used to solve the heat equation, as was explained in Ch. 4. However, FDM is just an example

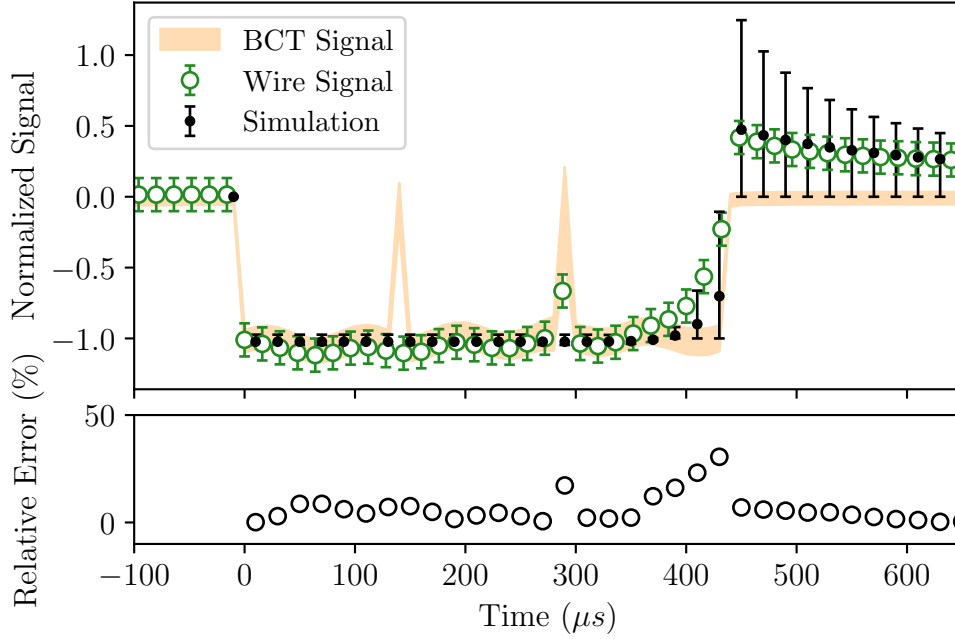


Figure 5.9: Signal generated in the wire intercepting the beam as a function of time. Compared with simulated intensity results.

of a numerical technique to solve PDEs and it is important to stress that alternative approaches abound. Commercially available softwares, such as Ansys [64], are commonly used to accurately solve a big variety of multiphysics phenomena. In particular, Ansys uses Finite Element Analysis (FEA) [55] to aid the users obtain solutions for real engineering problems.

5.2.1 Thin Wire Studies

The first part of this study compares the thermal evolution results, of a thin tungsten wire ($\phi = 40 \mu m$), calculated with the PyTT code and Ansys. Here, a LINAC4-like beam of particles was considered as the heating source. Table 5.2 summarizes the parameters of the beam. The parameters on this table remained constant for all the simulations. The beam pulse length was systematically varied to cover different temperature ranges.

Particle	Energy (MeV)	Inensity (mA)	Sigma x (mm)	Sigma y (mm)
Proton	160	25	0.5	1.

Table 5.2: Summary of the beam parameters that remained constant during the simulations.

To achieve the closes simulation conditions, a cuboid approximation of the wire was considered in both, PyTT and Ansys. The wire was oriented along the y-axis, with a wire length of 2 (cm). The spatial mesh resolution was 0.1 (cm) along the wire length and for the x and z directions a single mesh element was considered. The temporal resolution was divided into two sections. During the beam pulse, temporal

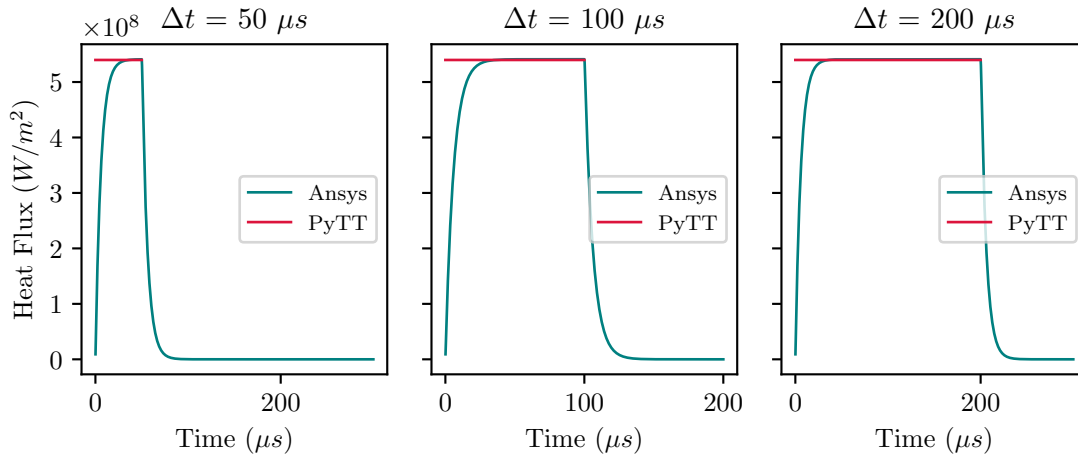


Figure 5.10: Examples of the heat flux provided to Ansys and PyTT for three different simulation cases.

elements of 10^{-7} (s) were considered, while during the cooling section the temporal elements were 10^{-4} (s) long. Material parameters, such as heat capacity and conductivity, were considered to be temperature-dependent. However, the emissivity was considered to be constant and equal to 0.1 in both cases.

In Ansys, the heat load was given using APDL commands [65]. Here, a gaussian distribution with the heat flux (W/m^2) equivalent of a beam pulse was described and applied to the material surface. Fig. 5.10 shows the heat flux applied to the wire by both Ansys and PyTT. The heat load in PyTT is constant during the presence of the beam pulse, and it immediately goes to zero once the beam pulse has passed. In the case of Ansys, a more smooth heat load transition is observed. The total integrated heat flux was the same in both programs, with a maximum discrepancy of 0.64% for the shorter beam pulses ($\Delta t \leq 50 \mu s$).

Fig. 5.11 compares the evolution of the maximum temperature, for three different beam pulse lengths, as a function of time. In these figures, one can observe how the PyTT simulations systematically give a higher maximum temperature than the results obtained with Ansys. The cooling rate in the PyTT code seemed to be slightly slower than in Ansys. The maximum discrepancy between the Ansys and the PyTT results was 11.2% for a temperature of 1356K.

One big difference between these two programs when performing this study was the simulation time. PyTT averaged 10.56 (s) when performing these simulations, while Ansys averaged 7:35 (min), in a Hp Intel(R) Core(TM) i7-6700 CPU, 16.0 Go RAM. This comparison might not be fair, Ansys is a much more complex simulation tool, with many many more options and accurate models. Also with the appropriate knowledge, the simulation times can be optimized. However, if what is important is to quickly obtain a number that can give the user if certain beam parameters are going to damage or not a detector, the PyTT code can manage to do it fast, with results that are very similar to the ones obtained with Ansys.

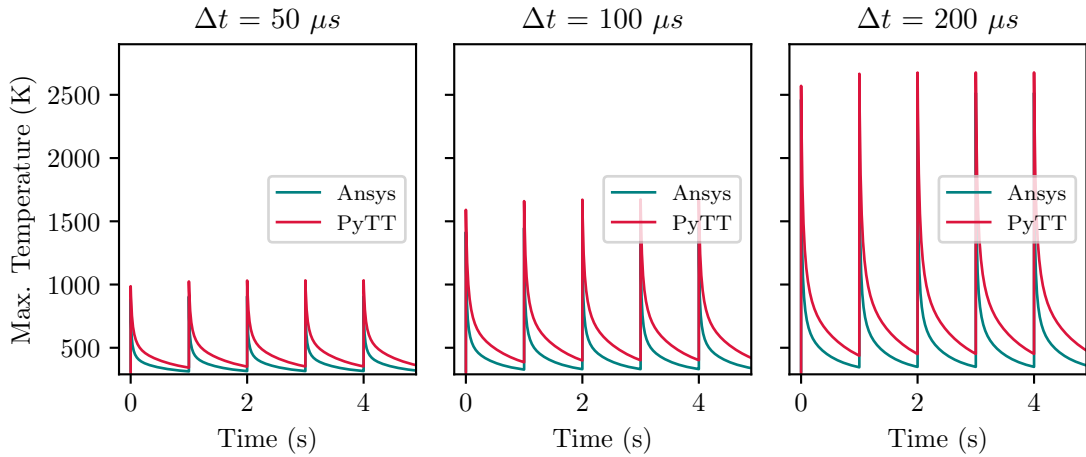


Figure 5.11: Comparison of the evolution of the maximum temperature in the detector as a function of time, for three different beam pulse lengths.

5.2.2 Thin Foil Studies

Similar Studies were performed with thin graphite foils (dimensions = 2 (cm) x 2 (cm) x 40 (μm)). The beam conditions for this study were the same as the ones described in table 5.2. Variations on the beam pulse length were used again to control the maximum temperature reached by the detectors.

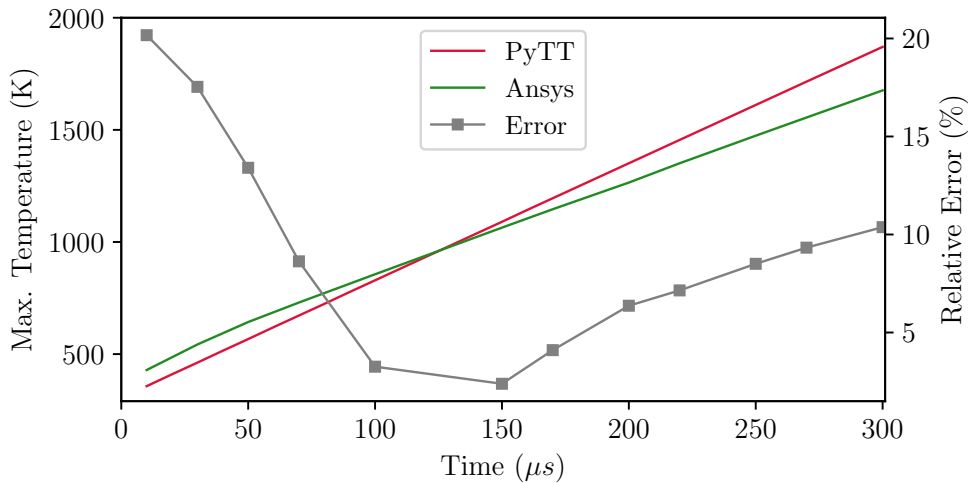


Figure 5.12: Comparison of the evolution of the maximum temperature in 40 μm graphite foil, as a function of beam pulse length. On the right axis, the relative error between them is represented.

Fig. 5.12 shows the maximum temperature reached (at equilibrium), with both PyTT and Ansys codes, as a function of the beam pulse length. From this figure, one can see how at higher temperatures PyTT continues to systematically give a higher maximum temperature. However, at lower temperatures, Ansys gives higher temperature results. The relative error between the Ansys and PyTT results is higher at lower beam pulse lengths, however, it never exceeds a 20%.

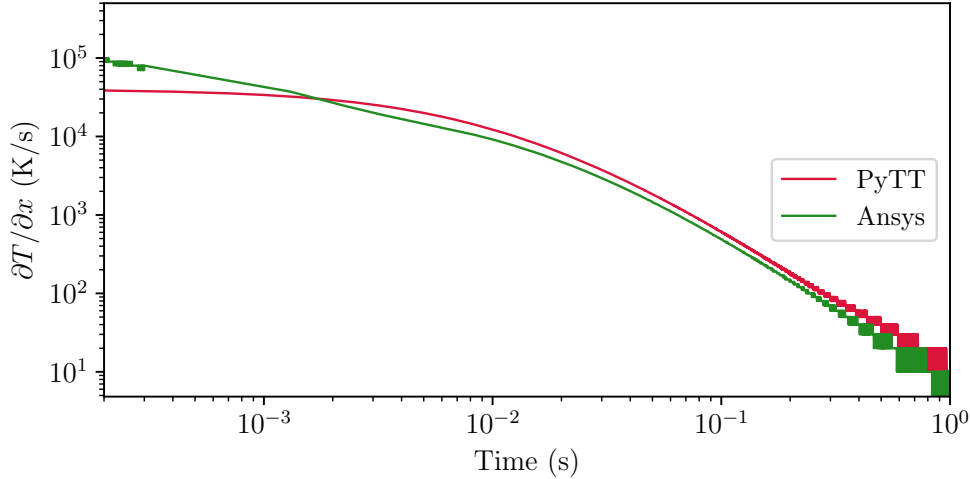


Figure 5.13: Comparison of the cooling rate between PyTT code and Ansys. For a $40\mu\text{m}$ graphite foil after a beam shot.

For a beam pulse length of $100\ \mu\text{s}$, the cooling rate was calculated with Ansys and with PyTT. Fig. 5.13 shows a comparison between the cooling rate after a beam shot. From this figure, we can observe how Ansys presented a much faster cooling at the beginning (higher temperatures) and a slower cooling after some time (lower temperatures). Here, the temperature right after the beam shot was $848\ \text{K}$.

Another interesting feature we wanted to compare was the heat distribution in space. Fig. 5.14 shows the heat distribution of the foil simulated with Ansys (left) and the PyTT code (right). These two figures were taken at the same instant of time ($10\ \text{ms}$ after beam shot arrival), during the cooling process. It is clear from these pictures that the heat distribution is very similar in both cases. It is very difficult to properly understand the differences between these results. Information about the numerical methods employed by Ansys is not publicly available. So no more quantitative or in-depth conclusions could be taken from these studies.

5.3 Beam Power Limit Calculations

Determining beam power limits means determining beam conditions that could potentially damage the detectors. To do that, the PyTT program was used to simulate the maximum temperatures reached by the detectors for the different expected beam conditions at their location. If the maximum temperature reached was above the safe limit, those beam conditions were considered to be harmful to the detectors.

5.3.1 SEM grid and Slow Wire Stanner at Linac4

For Linac4, the beam conditions under study were: Beam Intensity (I_{beam}), beam pulse length (Δt) and beam size (σ_x, σ_y). Fig. 5.2 shows a schematic representation of Linac4, with the different detectors location. The detectors in the L4L, L4D and L4C lines are made of graphite wires ($33\ \mu\text{m}$). The rest of the wire scanner detectors are also graphite wires, whereas the SEM grid detectors are gold-coated tungsten

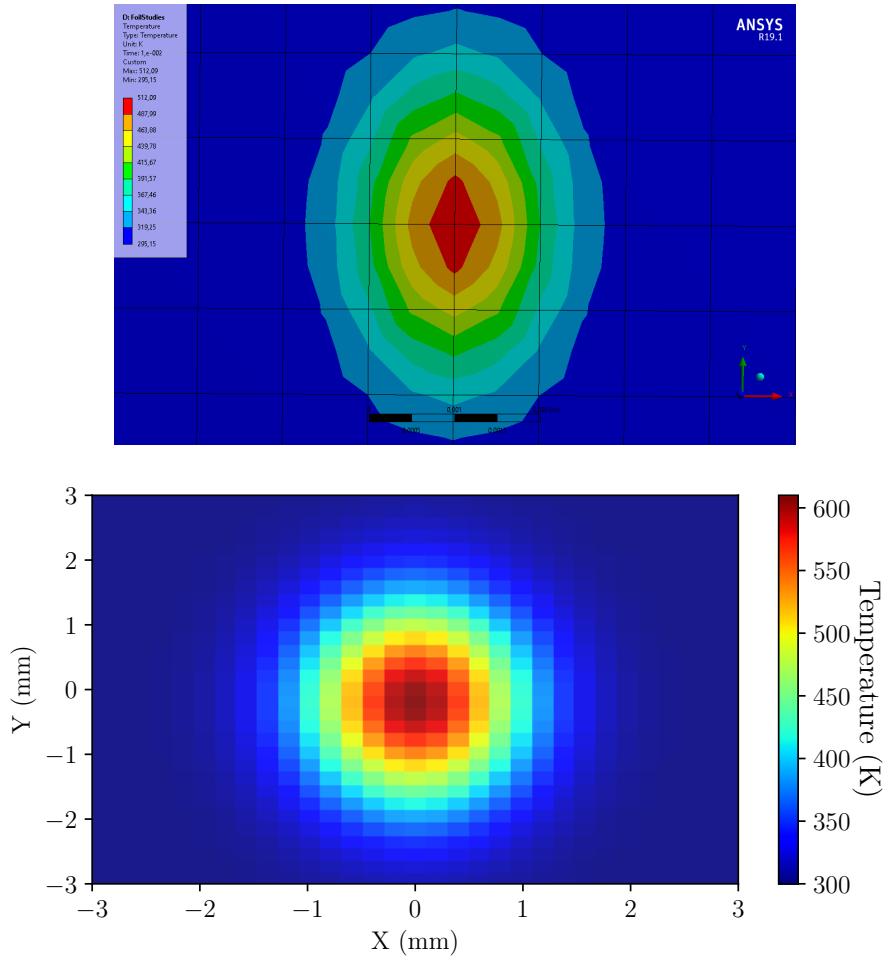


Figure 5.14: Comparison between thermal distribution in Graphite foil after one beam shot. In Ansys (top) and PyTT code (bottom). The black lines in Ansys have a separation of 1 mm.

wires ($40 \mu\text{m}$). Table 5.3 summarizes the range of the beam properties expected along the Linac4 accelerator.

For each detector, a set of dedicated simulations covering the whole parameter range were performed with the PyTT program. A maximum temperature of 1400K was taken as a safe maximum temperature limit. This limit is probably very conservative, as most of the detectors could easily handle up to 3000 K. However, due to the wire-gluing problem suffered in SEM grid detectors, due to gold coating, a much lower temperature limit was established.

Property	Min	Max	Units
Intensity (I_{beam})	10	25	mA
Pulse Length (Δt)	50	400	μs
Beam Size (σ_x, σ_y)	0.5	3.0	mm

Table 5.3: Range of beam properties expected at Linac4 accelerator.

Fig. 5.15 shows an example of the power limits calculated for a detector in L4C line (Detector 5) and a detector at the L4T line (Detector 12). Each square represents the maximum temperature reached by a simulation with the beam pulse

length indicated on the X-axis, and the beam intensity indicated on the Y-axis. The beam size in both cases was $\sigma_x = \sigma_y = 2.0$ mm. In both cases, we can observe that beam pulse lengths smaller than $200 \mu s$ are very safe. Neither detector was getting close to the set temperature limit. The only difference between the detectors is the energy deposition in the material. At higher energies, the energy deposition is smaller, so the maximum temperatures reached by the detector are smaller than the equivalent conditions at lower energies.

Fig. 5.16 shows a similar set of results, but this time, both detectors were placed at locations where the particle energy was already 160 MeV. The difference between the right plot and the left plot is the beam size. The left-hand side figure pictures a small beam size. The right-hand side figure pictures a larger beam size. From this figure, we can observe how small beam sizes result in much more critical thermal conditions.

In general, one should be very careful measuring small beam sizes at low energy ranges. An overall power limit for the Linac4 accelerator was established. Beam conditions were considered to be dangerous if the beam size was smaller than 1 (mm) and the beam pulse length was longer than $100(\mu s)$. An interlock system for SEM grids and wire scanners was established at Linac4 based on these results.

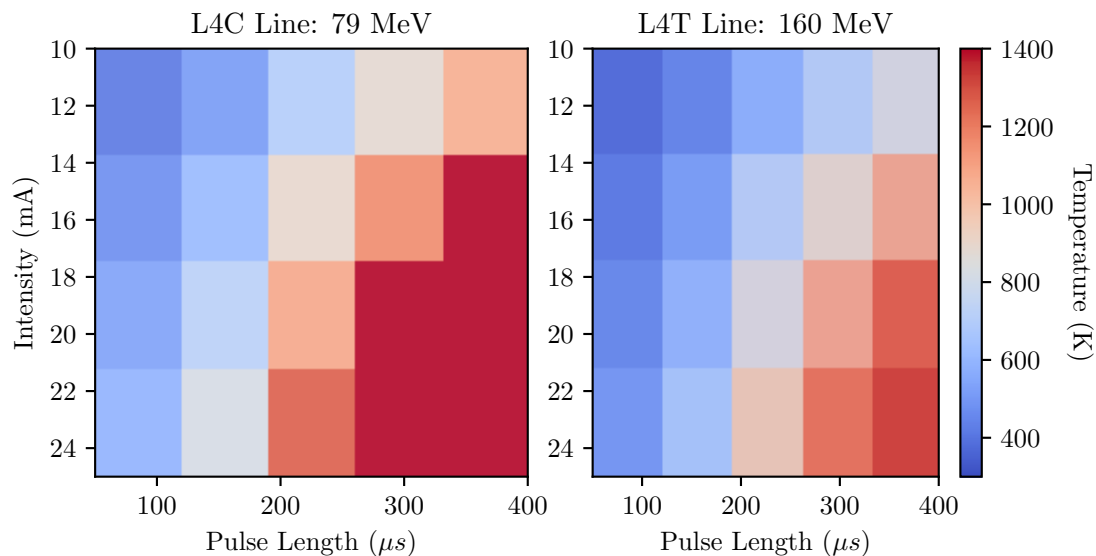


Figure 5.15: Power limit calculations for a detector at L4C (Left) and a detector at L4T (right) lines. The beam size in both cases was $\sigma_x = \sigma_y = 2.0$ mm.

5.3.2 Fast Wire Scanners at SPS

A new generation of beam wire scanners has been developed at CERN, in the framework of the LIU project [66]. In the SPS, 4 new wire scanner systems were installed, for horizontal and vertical beam size measurements. In this case, the relevant parameters under study were: beam emittance (at injection and extraction), the number of protons per bunch (from 10^9 to 10^{11}), the maximum number of bunches (from 1 to 288) and wire scanner velocity (from 1 m/s to 20 m/s).

For the SPS energies (26 GeV at injection and 450 GeV at extraction) differences in energy deposition are not as important as in the Linac4 case. Beam sizes are still a

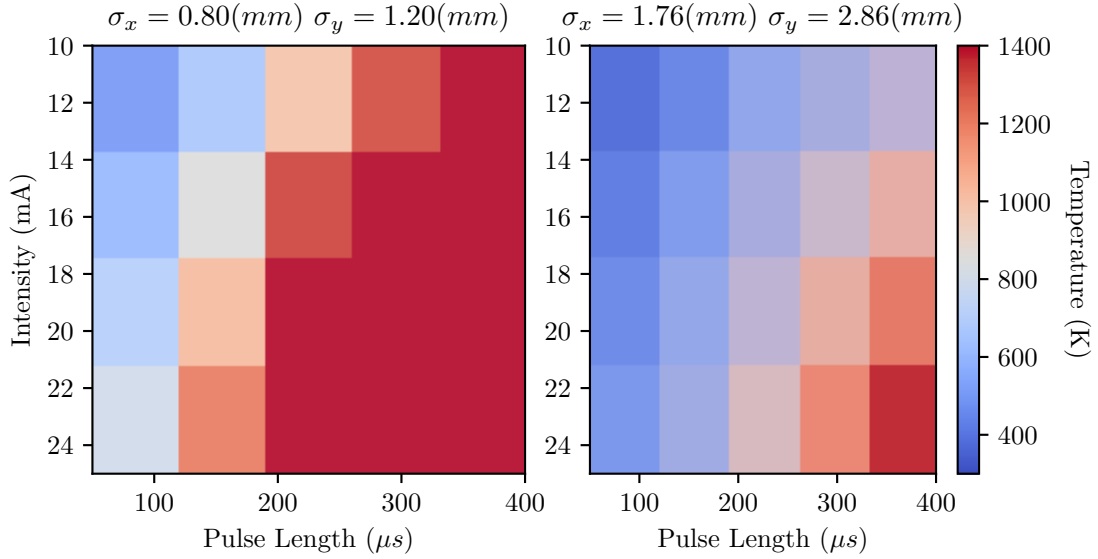


Figure 5.16: Power limit calculations for a detector at 160 MeV beam energies.

very important parameter to consider. In the SPS, the beam size is usually described in terms of beam emittance. One can easily convert from one to the other with the following relation:

$$\sigma = \sqrt{\frac{\epsilon_{norm}}{\gamma_{rel} \cdot \beta_{rel}}} \cdot \beta(s) \quad (5.1)$$

Where ϵ_{norm} refers to the normalized emittance and β_{rel} , γ_{rel} are the relativistic parameters. $\beta(s)$ is the courant-Snyder parameter at the position s . However, because the beam size decreases as the relativistic parameters increase, smaller beam sizes are found in the extraction case.

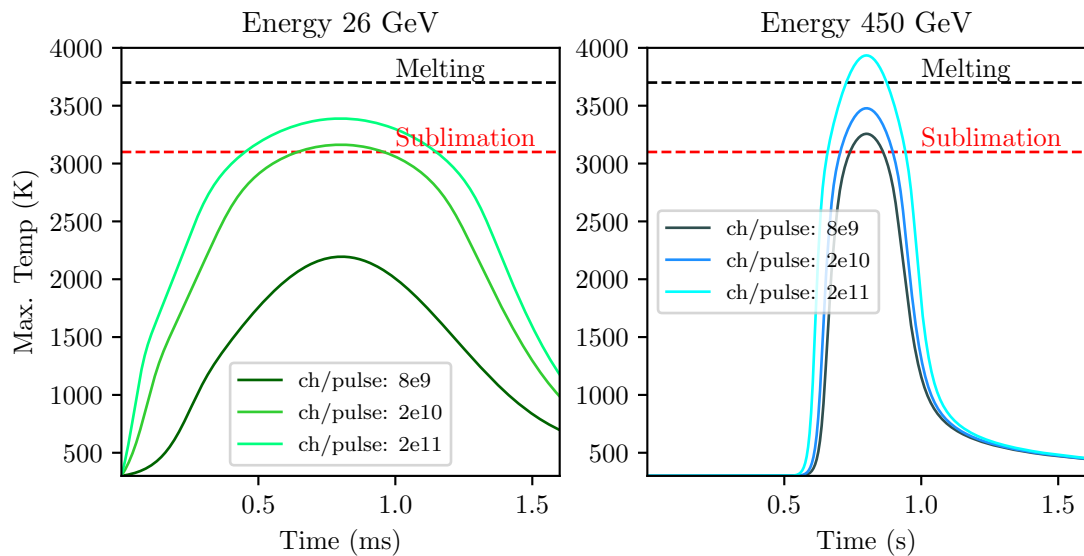


Figure 5.17: Comparison of maximum fast wire scanner temperatures reached for different beam conditions. Left: Injection energy. Right: Extraction energy.

Fig. 5.17 shows the evolution of the maximum temperature reached by a $33 \mu\text{m}$, graphite, fast wire scanner for a different number of particles per bunch. In this figure, the wire scanner speed was set constant to 1 m/s, and the total number of bunches was always 288. The figure on the left is for injection energies (26 MeV) and the one on the right is for extraction energies (450 MeV). In both cases, the higher the number of particles per pulse the higher the temperature reached by the detector. In these figures, we can also see the decrease of the beam size with the energy, as the temperature increase happens in a much narrower period during extraction energies.

The wire velocity is also a very important factor to consider. The slower the wire velocity the longer time it will spend in the central area of the beam, and thus the higher the maximum temperature reached. Increasing the wire speed is beneficial in terms of thermal limitations. However, as a tradeoff, we have the measurement resolution. Because the wire scanner in the SPS is much slower than the bunches being accelerated (revolution period $t_{rev} = 2.4 \cdot 10^{-5}\text{s}$). The number of points per sigma taken by a fast wire scanner can be calculated as:

$$n_{points} = \frac{\sigma}{v_w \cdot T_{rev}} \quad (5.2)$$

For a beam size of 1 mm, a maximum speed of 10 m/s can be used. Otherwise, the measurements would not have enough resolution. The wire damage can be associated with the density of charges traversing the wire [49]:

$$n_{ch} = \frac{N_{ch} \cdot d_w}{v_w \cdot t_{rev} \cdot \sigma} \quad (5.3)$$

Where N_{ch} is the total number of particles, understood as the number of particles per pulse times the number of pulses. d_w is the wire diameter and v_w is the wire velocity. As a limiting scenario, we could consider the case of a $33 \mu\text{m}$ Graphite wire, with a speed of 1 m/s and measuring a beam size $\sigma_x = \sigma_y = 0.3 \text{ mm}$. In this case the density of particles $n_{ch} = 2.5 \cdot 10^{12}$. Beam and wire conditions yielding a charge density higher than this number, are considered to be potentially harmful.

This number is consistent with the experiments performed by M. Sapnski [49]. This value is used in the SPS accelerator as a safety limit. Table 5.4 shows an example of how this safety value was used to calculate the maximum number of allowed turns for different wire scanners and beam conditions. At CERN SPS, the maximum number of injected turns can go up to 288. From this table, we can observe that only at injection energies this number of bunches can be measured.

Energy (GeV)	Beam Size (mm)		Wire Velocity (m/s)				
	σ_x	σ_y	1	6	10	15	20
25	3.03	2.10	54	323	538	807	1080
	2.0	1.38	35	213	350	531	708
450	0.72	0.50	12	74	129	194	258
	0.47	0.33	8	51	85	127	170

Table 5.4: Maximum allowed number of beam bunches for different beam conditions. The number of charges per bunch was $1.5 \cdot 10^{11}$ ch/bunch.

Chapter 6

Thin Wire Emissivity Measurements

6.1 Motivation

As discussed in Ch. 4, we saw that material properties such as melting (or sublimating) temperatures, heat capacity, thermal conductivity, emissivity, etc. play a very important role in properly describing the thermal behavior and limitations of our detectors. Uncertainties in these values yielded uncertainties in the final simulated results. The highest material parameter uncertainty was found in the case of the tungsten emissivity, showing an average uncertainty of around 43.26%.

This is shown with detail in Fig. 6.1. Every curve in this figure represents the emissivity as a function of temperature, reported by a different source [61].

Apart from the expected difference between Gold and Tungsten, there is a large spread of values for Tungsten. This is often related to different Tungsten samples featuring different surface properties (like toughness, rugosity, etc...) and geometries.

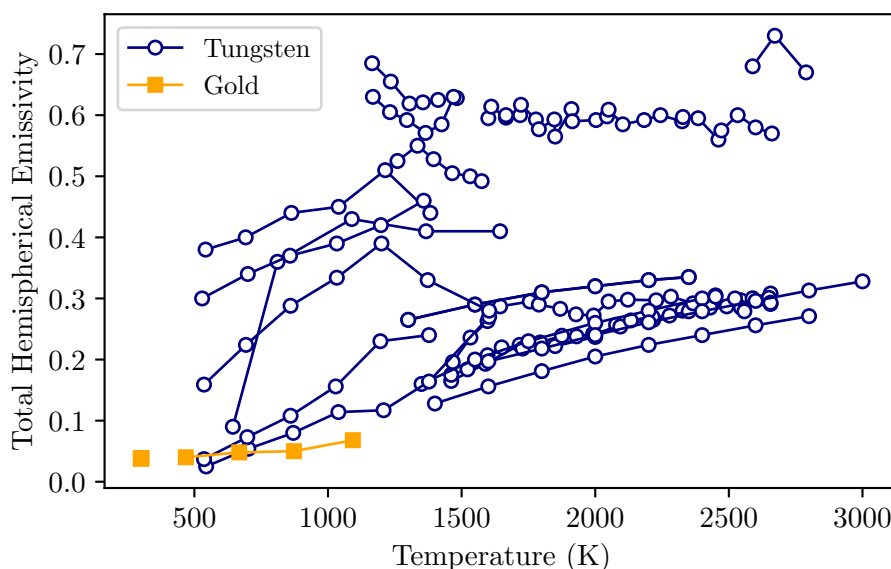


Figure 6.1: Examples of total emissivity measurements for Gold and Tungsten. From [61]

We decided it was necessary to experimentally measure the emissivity of the wires that are being used in the SEM grids, so more accurate thermal limits could be calculated. The results reported in this chapter were presented in IBIC2022 [67].

In general, it must be noted that at CERN, in particular, at LINAC4, wire grid and wire scanner detectors are often (e.g. at LINAC4) made of Gold-coated Tungsten wires¹.

However, as discussed previously, the high temperatures reached during operation can result in the Gold melting/evaporation and consequent removal. The emissivity will then be the one of Tungsten or a combination of Gold and Tungsten, which is difficult to predict.

6.2 Essentials in radiometry

A good starting point for this discussion is introducing the concept of the black body, which is crucial for understanding the concepts of heat radiation and its laws. This concept was first introduced in 1860 by Gustav r. Kirchoff [68]. It describes an idealized physical body that absorbs all incident radiation at all angles of incidence (no reflected energy, no energy transmitted through the body). For this ideal black body, in thermal equilibrium, the body emits all the absorbed energy. In 1900 Max Plank formulated a mathematical relationship to explain the spectral-energy distribution emitted by a black-body [69]:

$$B_0(\lambda, T) = \frac{2hc^2}{\lambda^5} \frac{1}{e^{\frac{hc}{\lambda k_B T}} - 1} \quad (6.1)$$

B refers to the spectral emissive power per unit area, and it is expressed in units of ($W \cdot sr^{-1} \cdot m^{-3}$). h is Planck's constant ($h = 6.62617 \cdot 10^{-34}$ Js) and K_b is Boltzmann's constant ($K_B = 1.38066 \cdot 10^{-23}$ J/K). Plank radiation has a maximum intensity at a wavelength that depends on the temperature of the body, see Fig. 6.2.

At room temperature (300K), a body emits thermal radiation that is mostly infrared. At higher temperatures, the peak of radiation moves towards the visible range, and we can see the body glowing visibly red. The maximum wavelength for a given temperature can be calculated with Wien's displacement law:

$$\lambda_{max} = \frac{0.2898}{T} \quad (6.2)$$

Here λ_{max} is given in (cm). If one is interested in the total power emitted per unit area at a given temperature, Eq. 6.1 can be integrated over all frequencies and solid angles. This is described by Stefan-Boltzmann law, which can be written as:

$$P = \sigma T^4 \quad (6.3)$$

With $\sigma = 5.67044 \cdot 10^{-8}$ ($W m^{-2} K^{-4}$). In practice, only very few objects approach the absorbing properties of an ideal black body. Usually, the treatment of radiation emission from real bodies is done using the parameter called emissivity. It compares the radiation emitted from the real body with the radiation emitted from an ideal black body at the same temperature. This parameter can be defined as follows:

¹This solution is convenient for mounting the wires on the supports, easier with the presence of Gold w.r.t. pure Tungsten

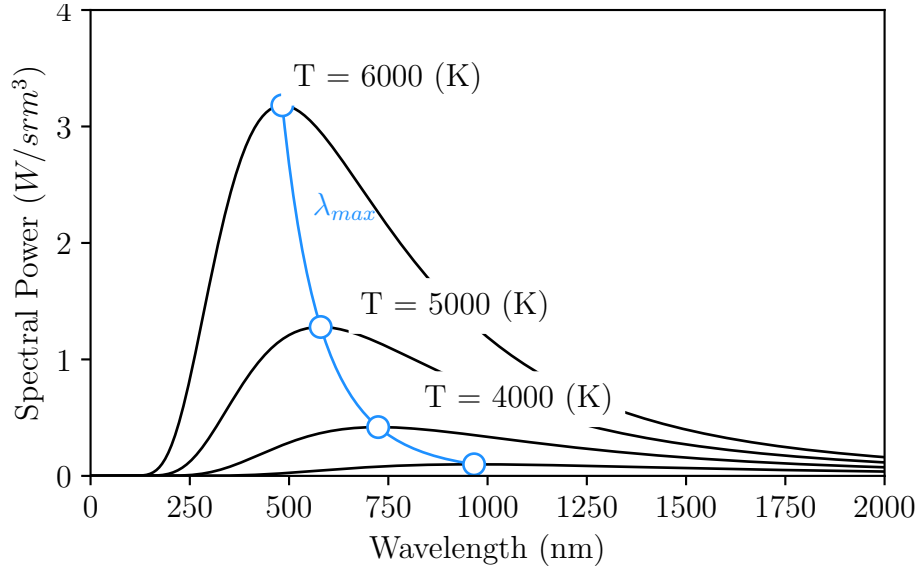


Figure 6.2: Black body spectrum for different temperatures. Blue line, Wien's displacement law.

$$Emissivity (\epsilon) = \frac{\text{Radiant Power}}{\text{Radiant Power Black Body}} \quad (6.4)$$

This parameter takes values between 0 and 1. The closer this parameter is to 1, the closer the body radiates as an ideal black body. The radiation emitted from the surface depends on several parameters (wavelength, temperature, direction), and so does the emissivity ($\epsilon = \epsilon(\lambda, T, \theta, \phi)$). Fig. 6.3 shows a schematic description of the emissivity definitions. Depending on the dependencies considered, different names are given to the different values of emissivity.

- **Directional Monochromatic (or Spectral) Emissivity:** Is the ratio between the spectral radiance of a body and that of the black body for a given direction and wavelength:

$$\epsilon_{\lambda, \theta, \phi}(\lambda, T, \theta, \phi) = \frac{B_{\text{Material}}(\lambda, T, \theta, \phi)}{B_0(\lambda, T)} \quad (6.5)$$

This is the finest description for a given material. B_0 does not depend on the incidence for a black body.

- **Hemispherical Monochromatic (or Spectral) Emissivity:** It is obtained by integrating the directional monochromatic emissivity over all directions of a hemisphere.

$$\epsilon_{\lambda}(\lambda, T) = \frac{1}{\pi} \int_{\phi=0}^{2\pi} \int_{\theta=0}^{\pi/2} \epsilon_{\lambda, \theta, \phi}(\lambda, T, \theta, \phi) \cos\theta \sin\theta d\theta d\phi \quad (6.6)$$

- **Total Directional Emissivity:** The spectral emissivity is integrated over all the spectral length.

$$\epsilon_{\theta, \phi}(T, \theta, \phi) = \frac{\int_{\lambda=0}^{\infty} B(\lambda, T, \theta, \phi) d\lambda}{\int_{\lambda=0}^{\infty} B_0(\lambda, T) d\lambda} \quad (6.7)$$

- **Total Hemispherical Emissivity:** is defined as the integral of the directional total emissivity $\epsilon_{\theta,\phi}$ over all directions of a hemisphere. In terms of total directional emissivity:

$$\epsilon(T) = \frac{1}{\pi} \int_{\phi=0}^{2\pi} \int_{\theta=0}^{\pi/2} \epsilon_{\theta,\phi}(T, \theta, \phi) \cos\theta \sin\phi d\theta d\phi \quad (6.8)$$

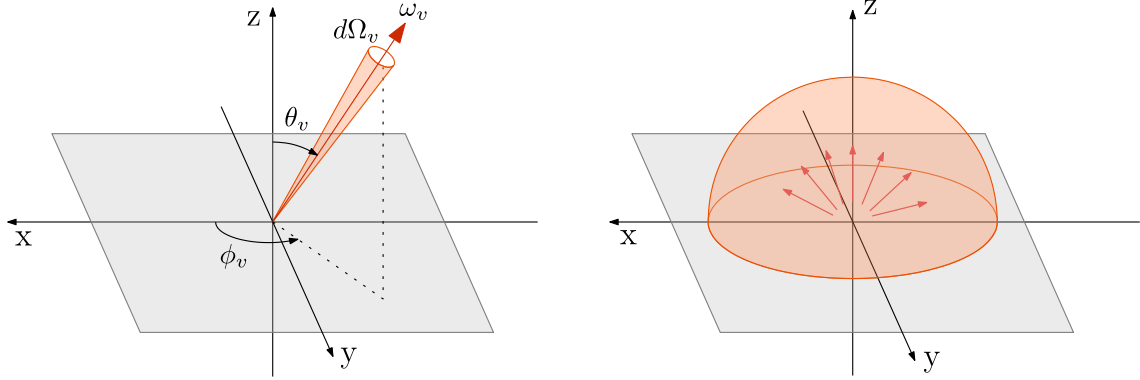


Figure 6.3: Schematic representation of emissivities definitions. Left: Directional Emissivity. Right: Directional emissivity.

Unless specified otherwise, in this document, when talking about material emissivity, we are referring to the total hemispherical emissivity. Measuring this total hemispherical emissivity will be the focus of the following sections.

6.3 Emissivity Measurement Methods

Many methods can be used for measuring the emissivity. They are commonly classified as direct or indirect methods, according to the physical principle of measurements. Direct methods are those where the power radiated from the surface is measured directly and can be also distinguished in calorimetric and radiometric methods. Indirect methods at first measure the reflectivity or transmissivity of the object of interest, assuming it is not opaque. Then the emissivity is calculated from Kirchoff's laws. Reference [70], presents a detailed description of several types of direct radiometric methods, with a great number of examples that measure the emissivity using this technique. Indirect measuring examples can be found in [71], [72], [73].

6.4 Calorimetric Method

In our particular case, we decided to use the calorimetric method, based on studying the energy balance of the sample while bringing it, in steps, at different equilibrium temperatures.

At each step the emissivity, characterizing the radiative losses, is the only unknown and is inferred by solving the energy balance.

The main advantage of this method is that it does not requires sophisticated or expensive equipment. In addition, it can be easily implemented with small sample

sizes. It is a direct and absolute method so it does not require a referenced standard to obtain the absolute emissivity value.

As a drawback, a constant power must be provided to the sample to maintain the temperature. The measurement is usually performed in a steady state, it is time-consuming. As it is important to suppress the energy transfers by convection, the sample must be placed under a vacuum (typically 10^{-5} bar). The measurement of the surface temperature is normally the dominant uncertainty. This method provides information about the total hemispherical emissivity, but not about the radiation wavelength or directionality.

The calorimetric method is based on studying the energy balance of the sample at a certain temperature. This temperature is maintained by providing power electrically by the Jule effect. In this case, the energy balance of the system can be written as:

$$\left(\frac{\partial T}{\partial t}\right)_{tot} = \left(\frac{\partial T}{\partial t}\right)_{Ht} - \left(\frac{\partial T}{\partial t}\right)_{Rd} - \left(\frac{\partial T}{\partial t}\right)_{Con} \quad (6.9)$$

Rd and Cd terms are the radiative and conduction cooling effects, introduced in Ch. 5. The heating term can be expressed as:

$$\left(\frac{\partial T}{\partial t}\right)_{Ht} = \frac{I^2 R(T)}{C_p(T)\rho_v V} \quad (6.10)$$

I refers to the current applied to the wire sample and R is the resistance of that wire at a temperature T . C_p , ρ_v and V are the specific heat, the density and the volume of the wire. At the steady state, the temperature of the system remains constant ($\partial T/\partial t = 0$). In this case, Eq. 6.9 becomes a second-order Boundary Value Problem (BVP):

$$\frac{I^2 R(T)}{C_p(T)\rho_v V} = \frac{S\sigma_{SB}\epsilon(T)(T^4 - T_0^4)}{C_p(T)\rho_v V} + \alpha(T) \left(\frac{\partial^2 T}{\partial x^2}\right) \quad (6.11)$$

Here the temperature depends only on the wire position $T(x)$. With Dirichlet boundary conditions:

$$\begin{cases} T(0) = T_{left} \\ T(L) = T_{right} \end{cases} \quad (6.12)$$

If one is able to properly measure the equilibrium temperature of the wire for a given intensity, and we assume that the other material properties are known accurately, the only unknown term in Eq. 6.11 is the value of the emissivity $\epsilon(T)$.

6.5 Temperature Measurement

The electrical resistance of a wire at a temperature T can be calculated as:

$$R(T) = \frac{\rho_{\Omega}(T)L(T)}{S_f} \quad (6.13)$$

Where S_f is the cross-section of the wire, considered to be constant over the wire length and not depending on temperature. $\rho_{\Omega}(T)$ is the resistivity of the material and $L(T)$ is the length of the sample and are both temperature-dependent magnitudes. For L , as a first approximation, a linear model can be used:

$$\Delta L = \alpha_l (T - T_0) \cdot L_0 \quad (6.14)$$

where α_l is the thermal expansion coefficient. It is difficult to give a mathematical description of the variation of the resistivity with temperature, as it is very much material-dependent. Tabulated values of the electrical resistivity for different materials are well-known and can be found in the literature. Usually they are expressed as the ratio between $R(T)$ or $\rho_\Omega(T)$ and the resistance or resistivity at room temperature ($R_0, \rho_{\Omega 0}$) [74]. Fig. 6.4 shows, as an example, the resistivity of tungsten as a function of the temperature.

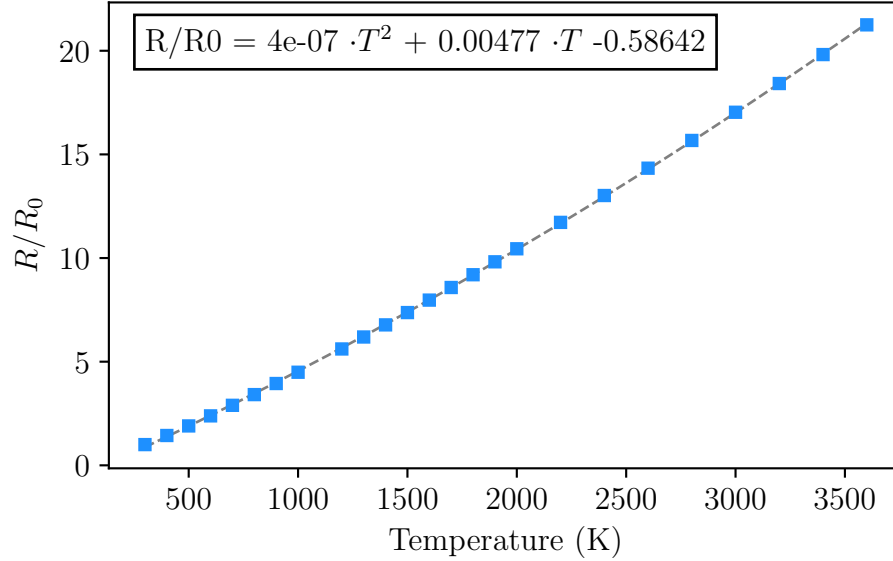


Figure 6.4: Evolution of the $R(T)/R(T_0)$ as a function of the temperature for a tungsten wire. From [74]

To calculate the temperature of the average temperature of the wire material, the ratio R/R_0 was calculated experimentally for a range of applied electrical current intensities. This was then compared to the values found in literature, that relate R/R_0 to temperature. In this way, a relationship between average temperature and wire current intensity can be calculated.

6.6 Numerical Calculation of the Emissivity

To calculate the emissivity of the material, an iterative method was used. The steps for converging to a solution are the following:

1. An initial guess of the emissivity is given as ϵ_i^0 , where the super-index indicates the iteration number).
2. With this value of the emissivity, the BVP is solved and then the average temperature along the wire is calculated (T_{sim}^n).
3. The calculated value of the temperature is compared to the experimentally measured one:

$$e^n = T_{sim}^n - T_{meas} \quad (6.15)$$

If the simulated temperature is higher than the measured one, it means that the cooling should be stronger, that is, the value of the emissivity should be higher. Conversely, if the simulated temperature is smaller than the measured one, the value of the emissivity should be reduced.

4. The value of the emissivity is updated as follows:

$$\epsilon_j^{n+1} = \begin{cases} (\epsilon_j^n + 1)/2, & \text{if } e^n > 0 \\ (\epsilon_j^n)/2, & \text{if } e^n < 0 \end{cases} \quad (6.16)$$

5. This process is repeated until convergence is achieved.

If the initial guess of the emissivity is between 0 and 1, the iterative process always keeps it in this range. The convergence condition is met once $|\epsilon^n - \epsilon^{n+1}| < 10^{-3}$. If such a condition is never met, the iterations stop when at $it_{max} = 50$. A detailed study of the residuals was also performed when the convergence condition was met.

To solve the BVP, the derivatives can be approximated using the corresponding differentiation matrices associated with a set of discrete nodes. In this case, it is a little simpler, compared to Ch. 4, as we are dealing with an ordinary differential equation, not a PDE. For this study, a central difference (CD2) was used to approximate the spatial second derivative. That is:

$$\left. \frac{d^2T}{dx^2} \right|_{x_i} = \frac{T_{i+1} - 2T_i + T_{i-1}}{2\delta_x^2} + \mathcal{O}(\delta_x^2) \quad (6.17)$$

Rewriting this system in a matrix form yields:

$$\begin{bmatrix} 1 & 0 & 0 & 0 & 0 & 0 \\ 1 & -2 & 1 & 0 & 0 & 0 \\ 0 & 1 & -2 & 1 & 0 & 0 \\ 0 & 0 & \ddots & \ddots & \ddots & 0 \\ 0 & 0 & 0 & 1 & -2 & 1 \\ 0 & 0 & 0 & 0 & 0 & 1 \end{bmatrix} \begin{bmatrix} T_0 \\ T_1 \\ T_2 \\ \vdots \\ T_N \\ T_{N+1} \end{bmatrix} = \begin{bmatrix} f_0 \\ f_1 \\ f_2 \\ \vdots \\ f_N \\ f_{N+1} \end{bmatrix} \quad (6.18)$$

Where T_i are the unknowns of the BVP. $f_0 = T_{left}$ and $f_N = T_{right}$. While the rest can be written as:

$$f_i = \delta_x^2 \cdot (A + BT_i^4) \quad (6.19)$$

With $A = -\frac{1}{\alpha}(I^2R + S\epsilon\sigma_{SB}T_0^4)$ and $B = \frac{1}{\alpha}S\sigma_{SB}\epsilon$. Due to the T_i^4 term, this is a nonlinear system of equations. For solving this system of equations Newton's method for nonlinear systems was used [59]. In this case, tolerance of 10^{-8} was considered. After calculating the temperature distribution the average temperature is calculated:

$$T_{sim} = \frac{1}{L} \int_0^L T(x)dx \quad (6.20)$$

This is done so the measured temperature (T_{meas}) can be compared to the simulated one (T_{sim}).

6.7 Experimental Set Up

The experimental setup was designed and put together with the huge assistance of Miguel Martin ², who implemented from scratch the electronics used for this experiment. The setup consisted of: Power Supply, Acquisition system, Vacuum system and Sample. Picture 6.5 shows a picture of full experimental set up. The total cost of the experiment was under 300 CHF as most of the equipment was already available.

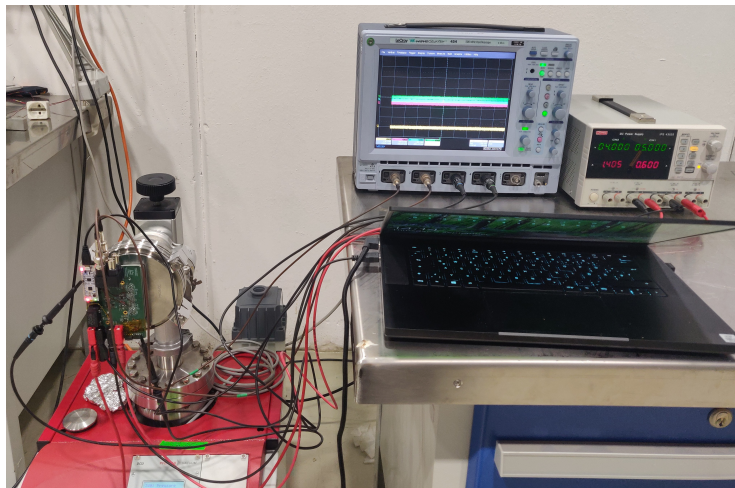


Figure 6.5: Picture of the experimental setup for emissivity measurements.

The system was powered by a lab power supply. On-board DC-DC converters and linear regulators in the acquisition system adapted the input voltage to the levels necessary to power the various analog parts of the circuit. An oscilloscope was sometimes used to monitor intermediate signals in the acquisition system and guarantee accurate measurement results. The measurements were automatized and controlled via a python code. The measured data was also automatically stored and an on-the-fly analysis could be performed to cross-check the quality of the results.

A HiCube300 Eco, was used to create the necessary vacuum (10^{-5} bar) in the vacuum chamber. This pump includes a turbo-pump and a backing pump for achieving high vacuum applications (10^{-7} mbar). A vacuum gauge was available to continuously monitor the vacuum levels.

6.7.1 Acquisition system

The acquisition system consisted of an assembly of two circuit boards: the measuring board and the acquisition board. A schematic representation of the electronic setup is shown in Fig. 6.6. The measuring board had two main objectives: holding the wire with both ends and measuring the current and voltage drop in the wire. Fig. 6.7 shows a 3D design of this board. The wire was fixed on two of the turrets at a set distance. The redundancy on the turret number allowed for measuring wires of different lengths. This board was placed inside the vacuum chamber, and its size and design had to be adapted to its shape.

²miguel.martin.nieto@cern.ch

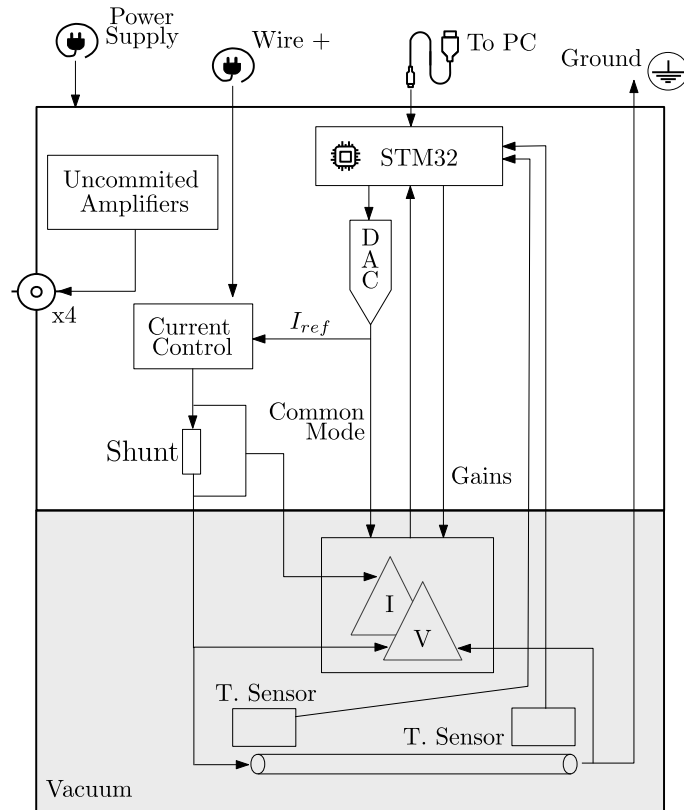


Figure 6.6: Schematic representation of the electronics set up.

The intensity was measured using a shunt resistor, which was placed in the acquisition board outside of the vacuum to facilitate heat dissipation. The voltage drop in the wire was measured directly at the mounting points, ensuring that only the voltage drop developed in the wire is taken into account. The vacuum feed-through connector was installed on the board, to transmit the signals across the vacuum barrier. The range of voltage (0 - 6V) and intensity (0 - 2 A) to be measured was quite broad. To overcome the limited range of the ADCs, different gains are available on the amplifiers. The temperature at the extremes of the wire (T_{left} , T_{right}) is measured by means of two temperature sensors mounted on the turrets.

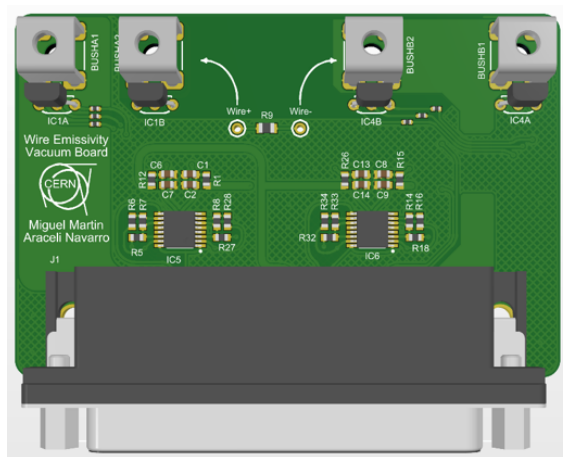


Figure 6.7: 3D design of the Measuring board.

The acquisition board captures and digitizes the measured signals, regulates the current flowing into the wire and configures the measurement board for gain and common-mode offset. Fig. 6.8 shows a 3D design of this board.

The measured current and voltage signals are digitized by the dual differential ADCs built into the micro-controller. A pulse conditioning block adapts the signal from the temperature sensor to the logic levels used by the micro-controller. The current, voltage and temperature signals are sent to a computer at a settable interval (minimum $100\mu s$) via a 1-Mbps USB serial connection. Four uncommitted amplifiers with BNC connectors are available to cross-check various signals with external equipment.

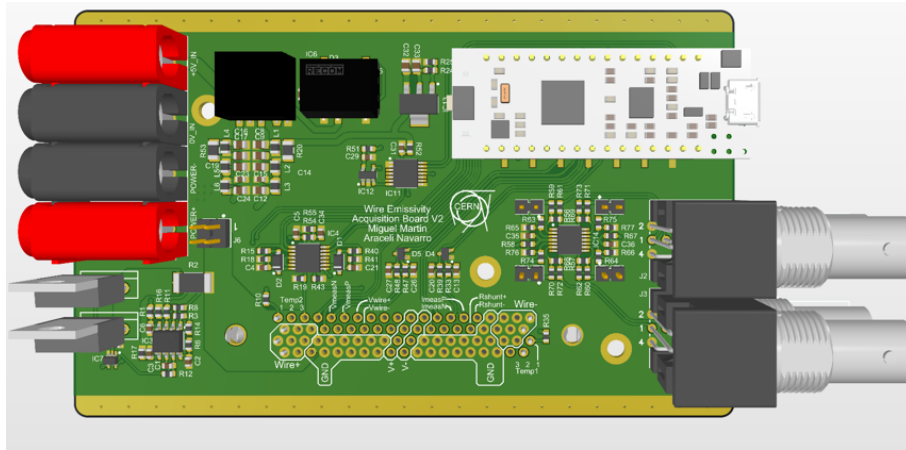


Figure 6.8: 3D design of the acquisition board.

6.8 Acquisition System Calibration

Before proceeding with the measurements, the acquisition boards had to be calibrated. That means one has to make sure that the voltages and currents registered by the data acquisition system are the same as the ones truly going through the wire. To cover the full range of intensity and voltage to be measured different gains were available on the amplifiers. These gains are summarized in table 6.1. A calibration curve had to be calculated for each amplification option.

Name	Amplification	Magnitude
GV0	Voltage	x 0.5
GV1	Voltage	x 1
GV2	Voltage	x 2
GI0	Intensity	x 1
GI1	Intensity	x 2

Table 6.1: Summary of available voltage and amplification options.

The calibration was performed outside of vacuum, by comparing the voltage and the current registered by the acquisition system after the digitalization to an independent measurement taken at the extremities of the wire, before any amplification was performed. This independent measurement was performed using a Keithley 2001

multi-meter for voltage measurements and a FLUKe 289 true RMS multi-meter for the intensity measurements. Fig. 6.9 shows the calibration curves of the acquisition system as a function of the current given to the system. All of the curves show clear linearity, demonstrating the electronics behave as expected. We will refer to the real current and voltage going through the wires as I_{real} and V_{real} , while the current and the voltage registered by the ADC as I_{adc} and V_{adc} . The linear fits for the different curves are:

$$I0 : \quad I_{real} = 0.969 \cdot I_{adc} + 0.0045 \quad (6.21)$$

$$I1 : \quad I_{real} = 0.547 \cdot I_{adc} + 0.0027 \quad (6.22)$$

$$V0 : \quad V_{real} = 2.313 \cdot V_{adc} - 0.0293 \quad (6.23)$$

$$V1 : \quad V_{real} = 1.071 \cdot V_{adc} - 0.0175 \quad (6.24)$$

$$V2 : \quad V_{real} = 0.525 \cdot V_{adc} - 0.0071 \quad (6.25)$$

Note that for convenience these equations are given as the inverse fitted curves in Fig. 6.9. The saturated points were not used for the calculation of these curves. The values of the voltage and the intensity used in the following sections are the real ones, calculated using these calibration curves.

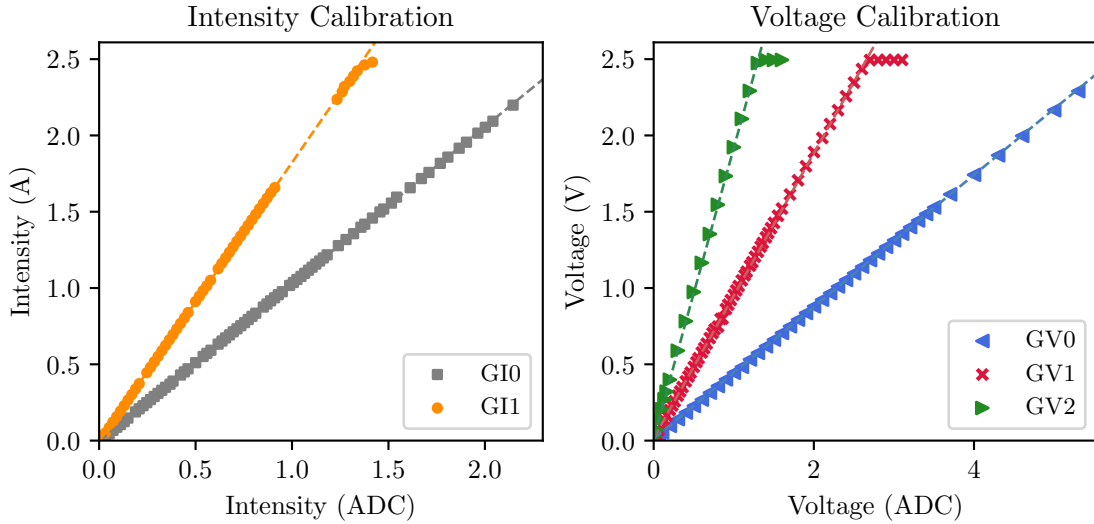


Figure 6.9: Calibration curves for the different amplification ranges. Left: Intensity Calibration. Right: Voltage Calibration. The explicit expression of the fitted curves (dashed lines) is provided in the text.

6.9 Experimental Results

For this analysis, Tungsten wires of two different diameters ($10\mu m$ and $40\mu m$) were measured. Both, with and without gold coating. For each type of wire, four samples were measured in order to compile some statistics.

6.9.1 Steady State Determination and Resistance Measurements

In Fig. 6.10 the raw data (before calibration) for the intensity, voltage and resistance is presented as a function of time. The applied intensity for the three figures on the left was 50 (mA) whereas for the three figures on the right was 190 (mA). The measured intensity remains constant along the measurement time as it is externally provided to the wire. The time it takes the voltage to stabilize reflects the change in the resistance of the wire for the applied intensity. The resistance was calculated from the previous two measurements using Ohm's law.

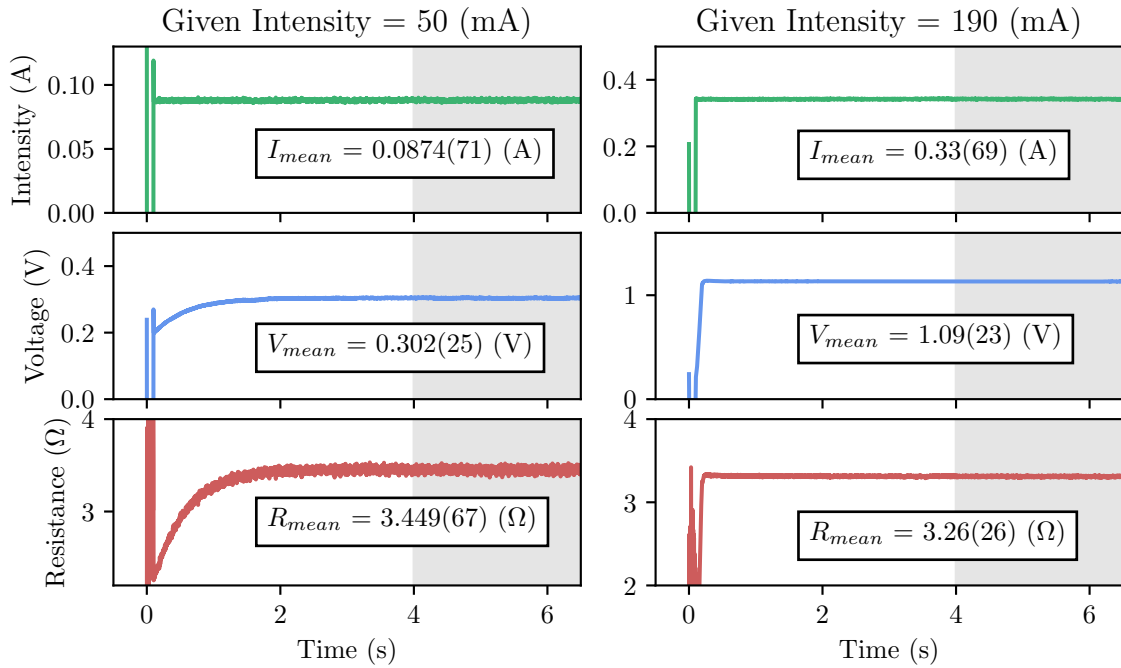


Figure 6.10: Raw data measurements (before calibration) for a 40 μm gold-coated tungsten wire. Intensity, voltage and resistance as a function of time for an applied current of 50 mA (left) and 190 mA (right). The mean values of the different quantities were calculated in the gray area.

We consider the steady state has been reached when the values of the voltage and the resistance remain stable along time ($dV/dt = dR/dt = 0$). This starting point is calculated by evaluating when the derivative of the measurements is smaller than 10^{-2} . The derivative was numerically calculated on a window of the measured data to overcome the measurement noise.

For each applied intensity the steady-state values were calculated and conveniently stored. Fig. 6.11 shows a summary of the intensity, voltage and resistance measured (on the steady state) for the different wires. The error bars in these plots show how much the measurements varied between samples of the same wire type. In these figures, we can observe how different gains needed to be used to cover all the voltage ranges. The 20 μm wires show a resistance ~ 4 times higher than the resistance measured for the 40 μm wires, which is in agreement with Eq. 6.13.

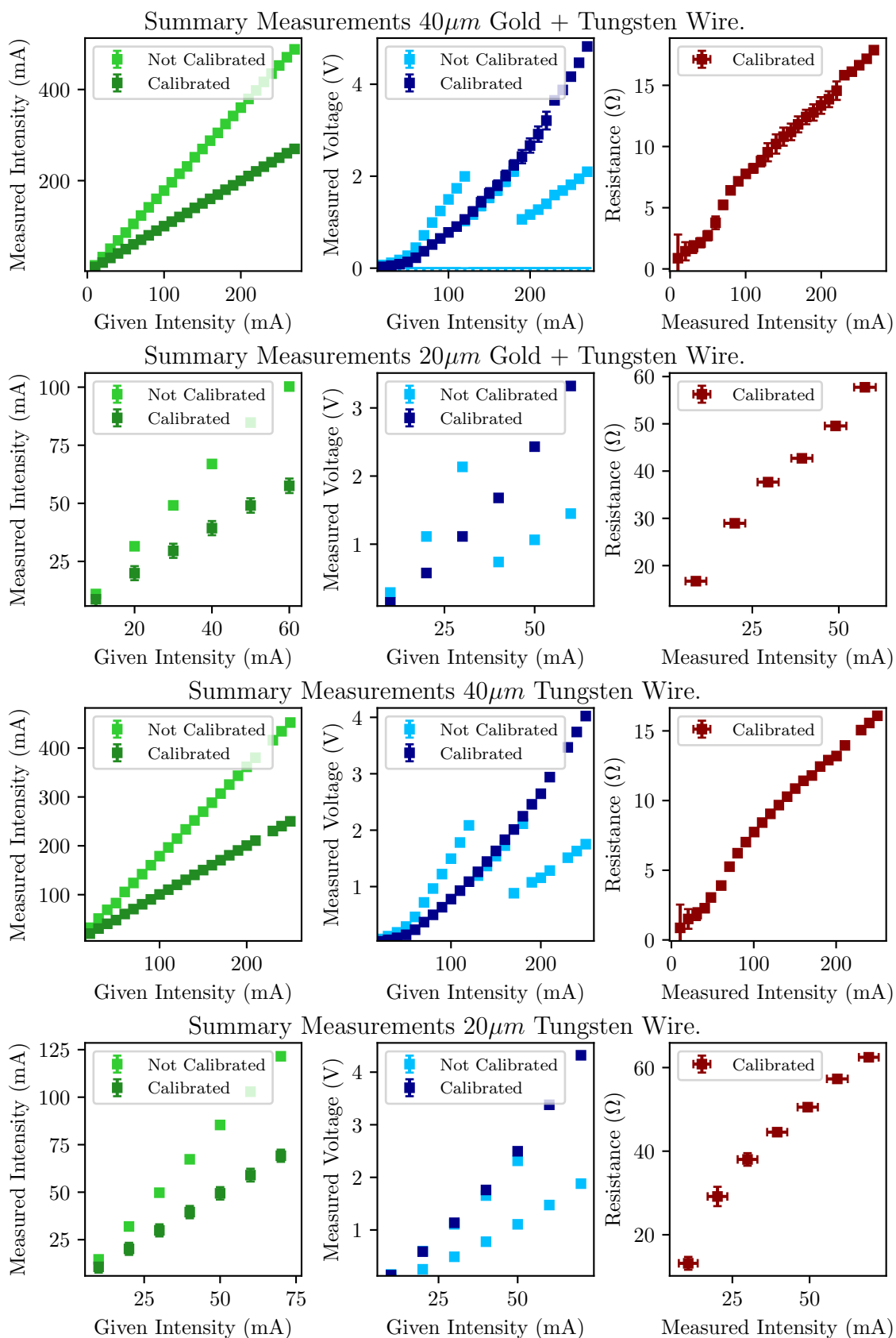


Figure 6.11: Summary of the measured intensity (left), voltage (center) and resistance(right), on the steady state, for the different samples as a function of the applied intensity.

6.9.2 Intensity Temperature Curves

The average temperature for each applied intensity was determined following the procedure explained in Sec. 6.5. First, the value of R_0 (Resistance at ambient temperature) was calculated. Measuring R_0 implies measuring the resistance with no current applied to the wire, which could not be done in reality. To calculate this, the measurement points (R,I) at very low current were extrapolated to zero using a parabolic model: $R(I) = R_0 + A \cdot I^2$. Figure 6.12 shows how the value of R_0 was calculated for the gold-coated tungsten wire.

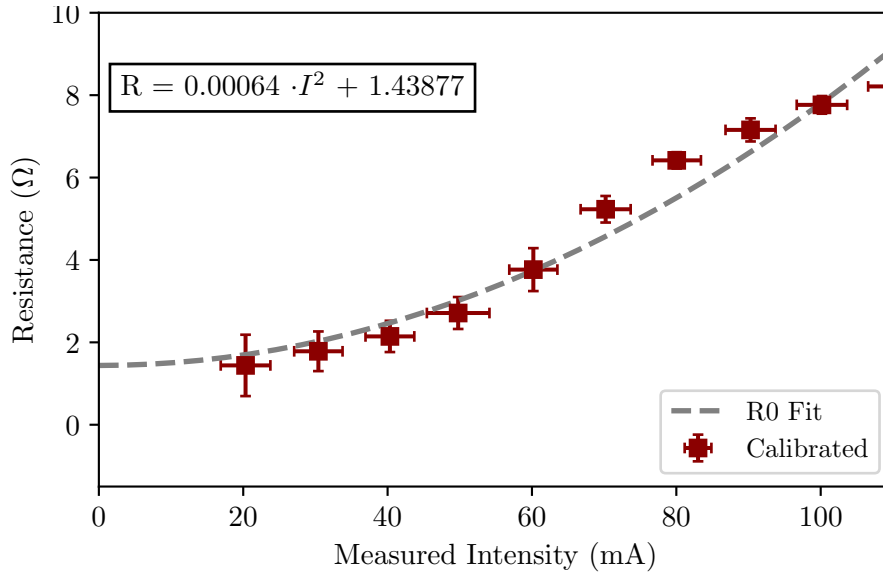


Figure 6.12: Calculation of R_0 for a $40\mu\text{m}$ Tungsten wire. Only the first 8 points were considered for the fitting.

A summary of the calculated values of R_0 for the other wire types can be found in table 6.2. Note that the relative error when calculating R_0 for the $40\mu\text{m}$ wires was smaller than 7%. However, the relative error for the $20\mu\text{m}$ wires bordered 60%. This much bigger error in the case of smaller wires comes from the too-coarse intensity scan. Unfortunately, the time restrictions prevented us from getting a much more accurate measurement.

Composition	Radius (μm)	R_0 (Ω)
AuW	20	10.5(63)
	40	1.438(76)
W	20	11.1(53)
	40	1.562(58)

Table 6.2: Summary of R_0 values for the different wire types.

To calculate the wire temperature as a function of the intensity we compared the values of the measured ratios R/R_0 with the ones one finds in the literature. Fig. 6.13 shows a summary of the average temperatures measured as a function of the measured intensity. This experiment covered a range of average temperatures from room temperature to almost 2500 K, was covered during the experiments. The

big uncertainties when calculating R_0 in the case of the $20\ \mu\text{m}$ wires yielded huge uncertainties in the average temperature calculation. Due to these big uncertainties, we considered these results unable to be used for accurately calculating the emissivity of the material.

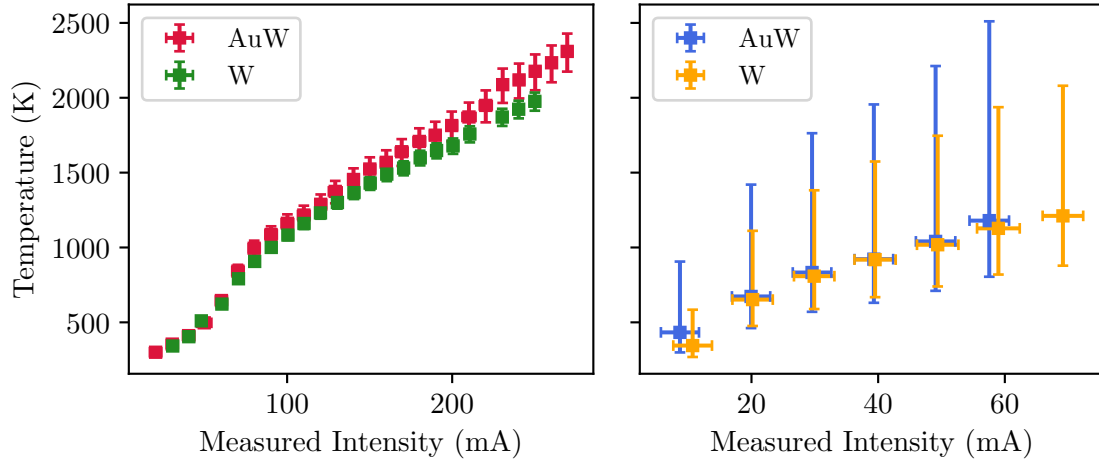


Figure 6.13: For the different types of wires, average temperature as a function of the intensity going through the wires.

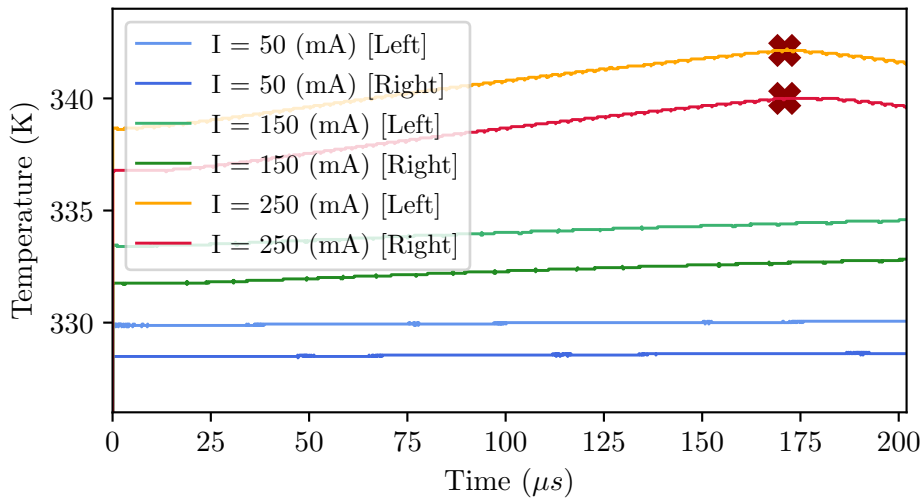


Figure 6.14: Measurement of T_{right} , T_{left} as a function of time for different applied currents. The red crosses indicate the point when intensity stopped is being provided to the wire.

6.9.3 Boundary Condition Measurements

The temperature at the extremes of the wire (T_{left} , T_{right}) was measured by two temperature sensors in direct contact with the turrets holding the wire. As an example of boundary thermal measurements, Fig. 6.14 shows the temperature at the extremes, as a function of time, for several different applied currents. In this figure, we can see an example of how the turrets were cooling down after a measurement

(red and orange curves). In this case, the cross indicates the instant of time when intensity stopped being applied to the wire. The maximum temperature reached by the turrets and the rate of the temperature increase depends on the applied current.

For the measurements, we also took into account the time evolution of T_{left} and T_{right} to calculate the starting point of the steady state. However, in some cases, the measurements were stopped before full equilibrium at the extremes was achieved due to the long time it took for the boundary temperature to stabilize and the small increase rate. Fig. 6.15 shows the equilibrium or quasi-equilibrium values of T_{left} and T_{right} measured as a function of the intensity going through the wire. The boundary temperature seemed to exponentially increase with the current applied. In all the range of measurements, the temperature increase remained smaller than 350 K.

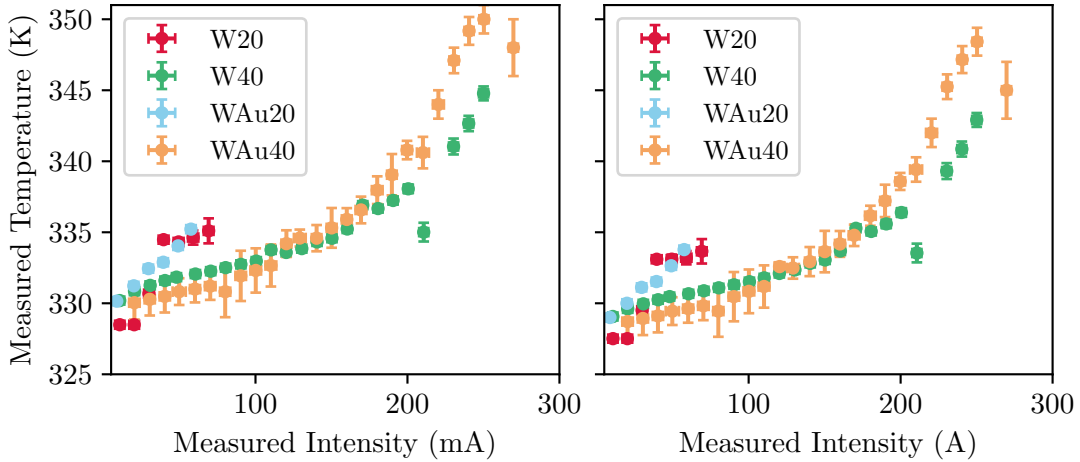


Figure 6.15: Summary of boundary equilibrium temperatures (T_{left} , T_{right}) measured by the thermo-couples at the extremes of the wire for different applied currents

6.9.4 Wire Emissivity

For all the measured (Intensity, Temperature) range of points, the emissivity of the wire was calculated following the procedure indicated in Sec. 6.6. As an intermediate result, Fig. 6.16 shows some examples of the equilibrium thermal profiles along the wire length. From this figure, we can see how the thermal profiles change as the applied intensity increases. At higher intensities (higher temperatures) the thermal profile is almost constant, and one could even simplify the problem by considering there is no conduction cooling in the energy balance [75]. This approximation highly simplifies the numerical study of the problem however for lower average temperatures this is no longer a valid approach.

The emissivity of the material was calculated numerically for all the measured intensity range. It was not possible to determine the value of the emissivity for 20 μm wires due to the high uncertainties in the average temperature values. Fig. 6.17 shows the computed values for the emissivity of the 40 μm wires. For the pure tungsten wires, the numerical method did not converge for temperatures smaller than 500 K. For both gold-coated and pure tungsten wires, the emissivity increased as the temperature increased. The emissivity of the pure tungsten wires was, in

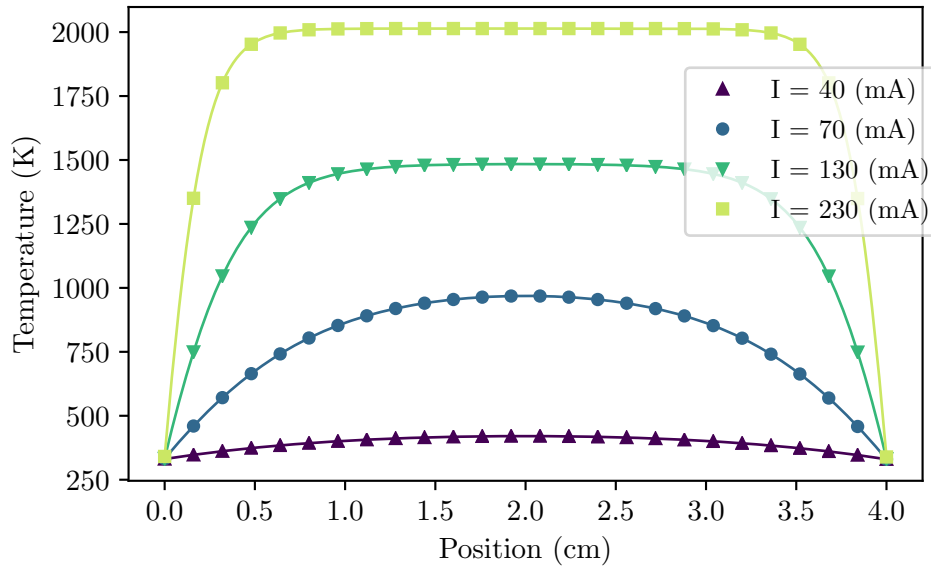


Figure 6.16: Steady state temperature profile calculated for different intensities.

average, larger than the emissivity of the gold-coated tungsten wires, ranging from 0.087(12) up to 0.176(21).

The emissivity values for the gold-coated tungsten wires appear to be consistent with the reported values of the emissivity of gold. In the case of pure tungsten wires, both the slope of measured values agree with some published references. Particularly those reporting values of poor electromagnetic radiators. The average statistical relative error for the measured values (error bars in Fig. 6.17) was of 15.21% in the case of pure tungsten wires and 26.26% for gold-coated tungsten wires.

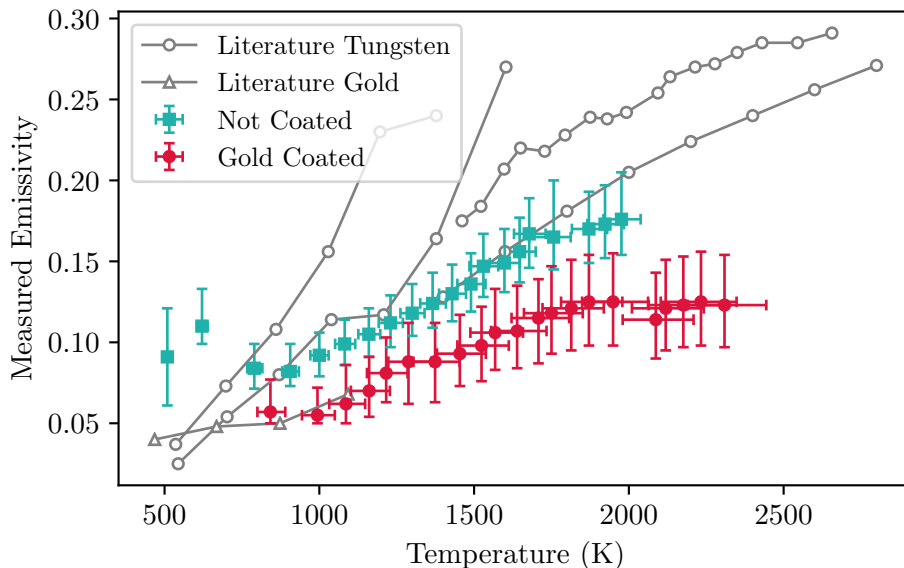


Figure 6.17: Measured emissivity for 40 μm tungsten wires as a function of the temperature.

6.9.5 Convection Effects

Convection cooling is the mechanism where heat is transferred from the hot device by the flow of the fluid surrounding the object. If the experiment had been done in the air, this convective term should have been considered. A very simple way of modeling could be:

$$\left(\frac{\partial T}{\partial t}\right)_{C_{nv}} = \frac{hA(T - T_f)^b}{V \cdot C_p(T) \cdot \rho_v(T)} \quad (6.26)$$

Where A is the area of the object, h is the heat transfer temperature, T_f is the fluid temperature and b is the scaling exponent [76]. The heat transfer coefficient highly depends on the physical properties of the fluid and the experimental conditions.

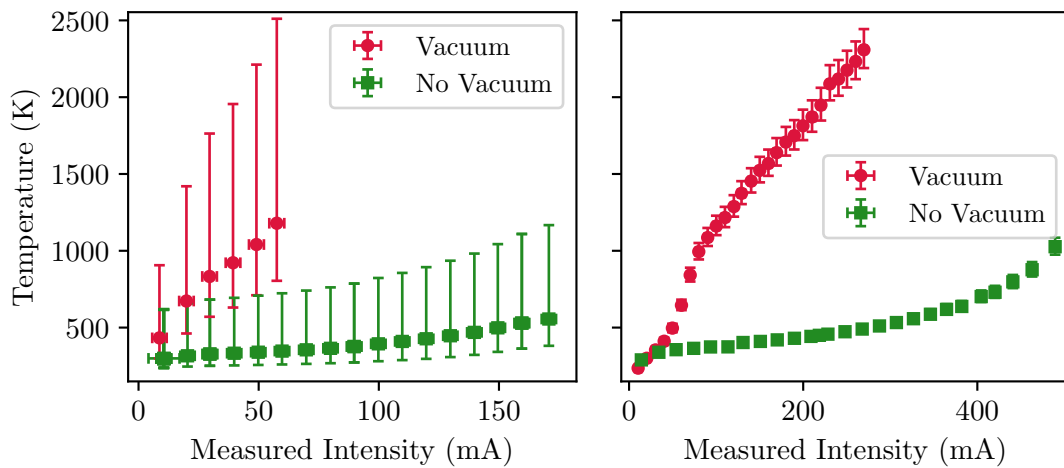


Figure 6.18: Comparison between measurements taken in and out of vacuum conditions. Left: 10 μm wire diameter. Right: 40 μm wire diameter.

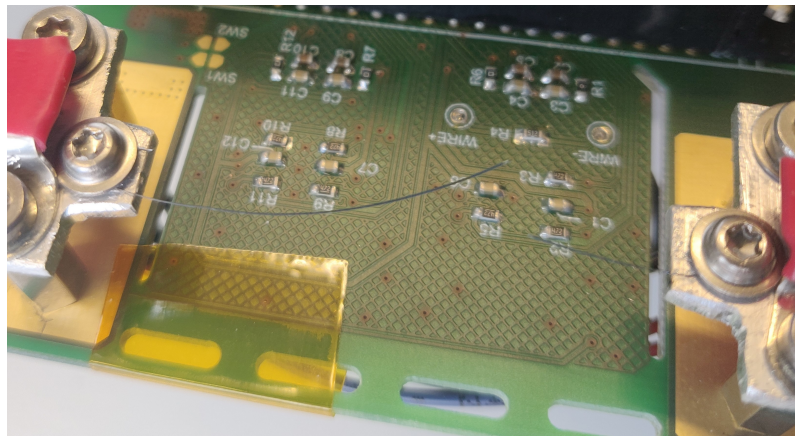


Figure 6.19: Tungsten wire after the measurements. Clear change of color is appreciated.

The values of h, for different conditions, can be found in the literature. However, the uncertainties of this coefficient introduce great uncertainties in our energy

balance equation, difficulting the calculation of the wire emissivity. Also, the temperature range that could be measured with the implemented setup was more limited in non-vacuum conditions.

Fig. 6.18 shows a comparison of the measured average temperatures for vacuum and non-vacuum measurements. From this figure, one can observe that for the same applied current, the maximum temperature reached in vacuum conditions is much higher. To avoid the big uncertainties introduced by the heat transfer coefficient and to be able to cover a larger range of temperatures with the available current, the experiments were performed in vacuum. Another effect that was observed during the measurements in the air was the oxidation of the metallic surface. A clear change of colors was observed in some of the samples (see picture 6.19) when the metallic gray color of tungsten changed to a dark blue color [77].

Chapter 7

H⁰H⁻ Monitor Calibration and Commissioning

This chapter is going to be slightly different from the previous ones. It explains the calibration of the H^0H^- monitors. The results presented in this chapter were presented in IBIC2021 [78]. As briefly explained in the introduction (Ch. 1), the LHC high luminosity program (HL-LHC) [79] calls for the production and acceleration of brighter beams from the injectors [80]. The space charge effects in the PSB represented one of the biggest limitations [81], due to the low energy and high brightness required.

During the Long Shutdown 2 (LS2), the new LINAC4 accelerator was connected to the PSB, providing 160 MeV H^- beam of particles. The increase of injection energy doubles the relativistic factor $\beta\gamma^2$ at the PSB injection, allowing the beam brightness to be doubled. To inject the H^- beam of particles to the PSB, a new charge exchange injection (CEI) system [82] was installed in each ring. This charge exchange injection provides also an improved injection brightness compared to the typical multi-turn injection. The reasons why are far away from the scope of this work, if the reader is interested, some information can be found here [83].

7.1 CEI to CERN PS Booster

The 160 MeV beam from the linac4 transfer line is distributed to the four levels of the PSB by a sequence of a vertical bending magnet. Fig. 7.1 shows a schematic representation of the injection line and injection region. The beam slices are first sequentially deflected vertically, by fixed field iron magnets (BI.DVT30) before being injected into the beam distributor (BI.DIS) [84]. The BI.DIST system, in combination with the BI.DVT40, deflect the beam sequentially into the different apertures of the BI.SMV10, which further deflects the beam to properly inject it into the four booster rings. During the splitting operation, two spur beams are generated, representing the head and the tail of the beam, which are then intercepted by dedicated dumps. These dump blocks are integrated with the septum magnet as internal devices to the BI.SMV magnet tank.

The distributor timing can be adjusted, providing very big flexibility in terms of beam injection to the PSB. Fig. 7.2 shows three examples of Linac4 pulse structures and distributor timings. After the splitting, the beam is injected into the booster rings using a newly installed charge exchange injection system (CEI) which is dis-

cussed in the next section. When in the following sections we refer to beam turns, we are referring to the number of beam micro-pulses injected into the PSB.

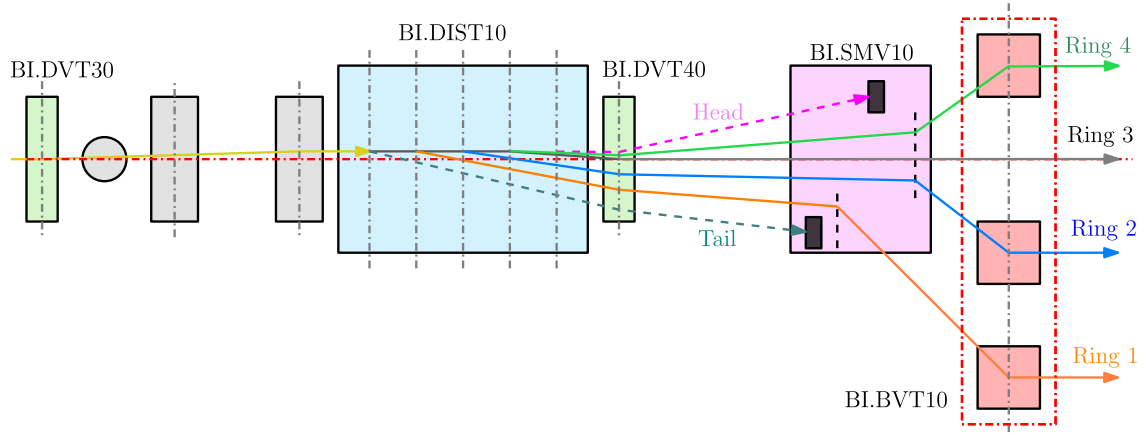


Figure 7.1: Schematic representation of the PSB injection line, featuring the DVTs, DIST and SMV vertical separation scheme.

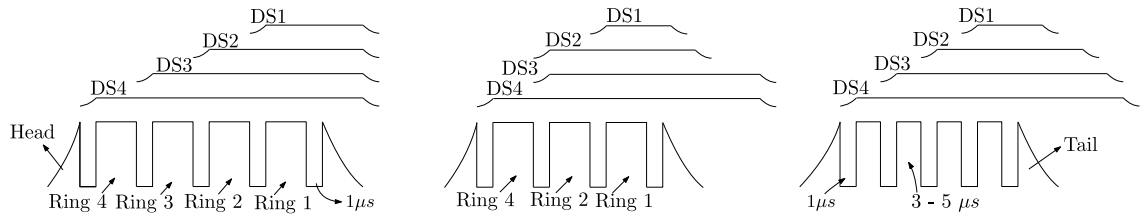


Figure 7.2: Possible Linac4 pulse structures and BI.DIS timing. Left: Standard operation with 65 - 100 μs injected turns per ring. Center: Operation with 0 turns injected in ring 3. Right: 3-5 injected turns per ring.

In general, the charge exchange injection (CEI) is performed by stripping two electrons, using thin stripping foils, from an H^- particle and transforming it into a proton (p^+). The closed orbit of the circulating beam is bumped onto the injection orbit, using a set of chicane magnets located around the stripping foil. The fully stripped p^+ follow the closed orbit of the beam while the partially stripped (H^0) and the unstripped (H^-) particles are dismissed.

Fig. 7.3 shows a schematic representation of the newly installed CEI system at CERN. The new system comprises, for each of the four booster rings, a stripping foil, a set of four pulsed dipole magnets (BSW) [85] and four horizontal kicker magnets (KSW) [86] (Not depicted in Fig. 7.3).

The first magnet (BSW1) acts as a septum, generating a high-field region for the circulating beam and a field-free region for the injected H^- beam. It is followed by three bumper magnets (BSW2-4) that help merge the injected beam with the circulating beam. BSW2 and BSW3 are installed at each side of the foil and are identical magnets. BSW4 has an enlarged horizontal gap to accommodate the unstripped particle beam as well as the unstripped particle monitor.

The stripping foil (about 20 x 20 mm wide) is made of carbon, with a density of around 200 μgcm^{-2} . The choice of material and thickness is driven by the stripping efficiency ($> 99\%$), beam loss and emittance blow up and temperature rise of the

foil [87]. In each of the rings, a set of six foils are available and can be interchanged thanks to a foil charger and handling system.

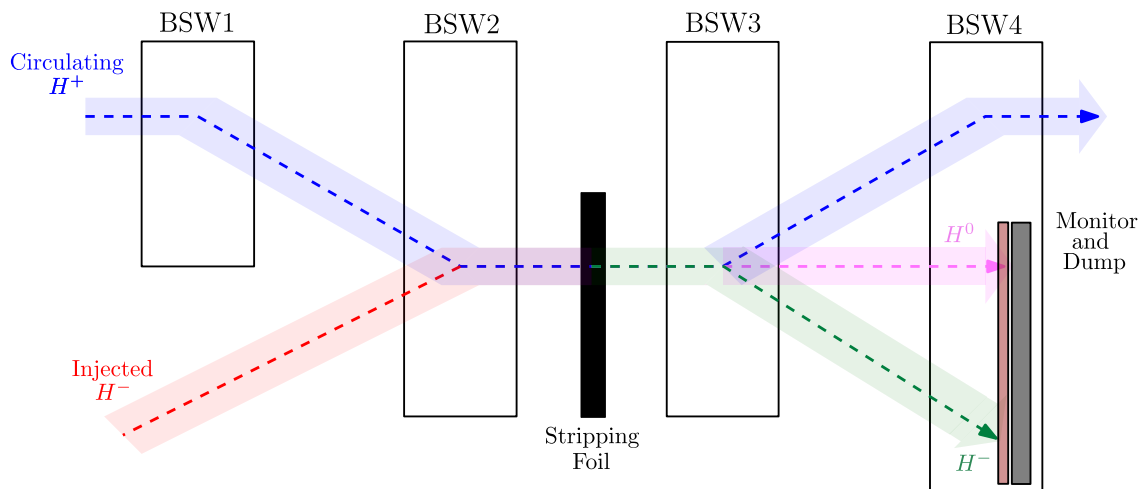


Figure 7.3: Schematic representation of PSB H^- Charge Exchange Injection system.

7.2 H^0H^- Beam Current Monitors and Dump

The injection region geometry and the very limited space that is available preclude extraction of the unstripped or partially stripped ions. For that reason, four internal Ti_6Al_4V dumps (one per ring) were installed downstream of the stripping foil, within the vacuum chamber of the chicane magnet BSW4. Fig. 7.4 shows the mechanical design of the dump (black element in the drawing) and Fig. 7.5 shows the integration of the dump in the booster ring.

The geometry of the dump provides an unobstructed passage for the circulating beam during injection, as well as for the injected proton beam, whilst providing optimal protection of the downstream elements by absorbing a few percent of the unstripped beam during regular operation and the full beam in the event of foil failure

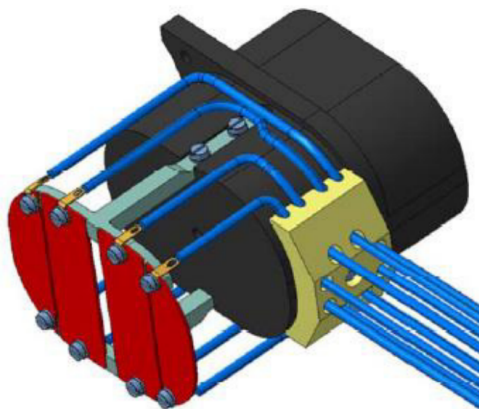


Figure 7.4: Mechanical design of the H^0H^- current monitors (red) and Titanium dump (black).

An intensity measurement of both, the H^0 and H^- beam particles impacting the dump is required to allow an efficient injection setup, monitor the efficiency of the stripping foil and protect the dump in case of a high-intensity beam impact (by providing an interlock signal in case of stripping foil failure). The H^0H^- monitors (represented in red in Fig. 7.4 and Fig. 7.5) are installed 4 cm upstream of the face of the dump. The distance between the dump and the intensity monitors is sufficient to prevent secondary electrons from the dump from interfering with the signals from the monitors.

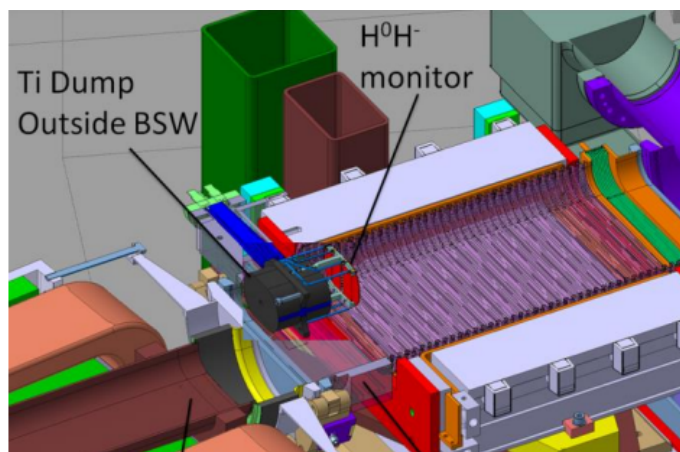


Figure 7.5: Integration of the H^0H^- dump (black) and intensity monitor (red plates) in a PSB ring. The purple element is the BSW4 magnet.

The H^0H^- intensity monitors consist of four titanium plates: two 22 cm wide central plates and two 18 mm wide external plates with around 1 mm separation between the plates. Having four independent plates allows for supplementing the intensity measurements with some beam position information. The two outer plates (with respect to the beam position) are expected to measure H^- particles while the two inner plates are expected to measure the partially stripped H^0 particles.

Titanium was chosen as the detector material for its low Z (i.e. low activation) and moderate conductivity ($2.34 \cdot 10^6 \Omega^{-1}m^{-1}$). This is a good compromise between the high conductivity needed for reading out the deposited charge and the low conductivity required due to the presence of a pulse magnetic field in the BSW4 chamber. The thickness of 1 mm guarantees to stop all the stripped electrons and is compatible with the presence of a vertical B-field.

As shown in Fig. 7.4 and Fig. 7.5), each monitor plate has two read-out cables (represented in blue). This duplication has been implemented only for hardware redundancy: in the case of cable damage, a second one is immediately available. During operation, only one signal cable per plate is connected to the acquisition system.

7.2.1 Expected signal generation

The electric signal generated in the plates allows determining the number of H^0 and H^- particles reaching the particle dump, and thus it determines the stripping inefficiency. As explained in Ch. 3, several effects contribute to the charge formation in the plates. In this particular case, the most relevant processes are, charge deposition (Q_{dep}) and Secondary emission (Q_{se}).

Table 7.1 summarizes various terms contributing to the plate signal generation per incident particle. Table 7.2 shows the expected values of the signal generated in the H^0H^- plates. SEE in this case will diminish the absolute value of the measured signal, and it will be a non-welcomed effect. Luckily the magnetic field of BSW4 is large enough to suppress this SE. More details on this are given in Sec. 7.6.3.

η	μ	BS_p	BS_e	SEY_p	SEY_e
0.997	0.463	0	0.5369	0.0295	0.0779

Table 7.1: Necessary values for predicting current generated in H^0H^- plates.

Q(e/ H^0)		Q(e/ H^-)	
w. SE	w.o. SE	w. SE	w.o. SE
-0.2841	-0.463	-0.627	-0.926

Table 7.2: Expected signal generated in H^0H^- per incident particle.

In normal operation conditions, during injection, the expected number of H^0 particles is around 2% of the total Linac4 pulse. The expected number of H^- particles is very low $\approx 10^{-4}\%$. Stripping foil degradation is tolerated until the beam dump load reaches a safety limit. Currents larger than 10% of the Linac4 beam pulse generate an interlock signal that stops the particle beam at the source.

7.3 Monitor Electronics, Layout and functionalities

The electronics for the H^0H^- intensity monitors are designed to ensure the continuous measurement of the H^0 and H^- particles and to function as an input to the interlock system that protects the H^0H^- dump. For each PSB ring, the electronics for monitoring the 4 plates are embedded into a single VME card. Two main circuits can be found in these cards, the signal monitoring circuit and the interlock circuit.

7.3.1 Signal Monitoring Circuit

This part of the circuit aims for high-sensitivity intensity measurements. A schematic diagram of the electronic circuit can be found in Fig. 7.6. The intensities measured by each plate are fed to a fast amplifier. The amplifier output is connected to an OASIS channel, which gives information on the real-time monitoring of the signal. In parallel, it is also connected to a fast integration system.

To sample the signal every PSB turn (every $1\mu s$), the integration is performed using two alternating fast integrators. The timing logic and system response are shown in Fig. 7.7. The integrator output is given to a fast ADC, which converts the integrated charges to digital samples. The ADC read-out and the discharge of the integrators take around 120 ns for every PSB turn. This limits the length of the beam pulse that can be integrated to a maximum of 780 ns.

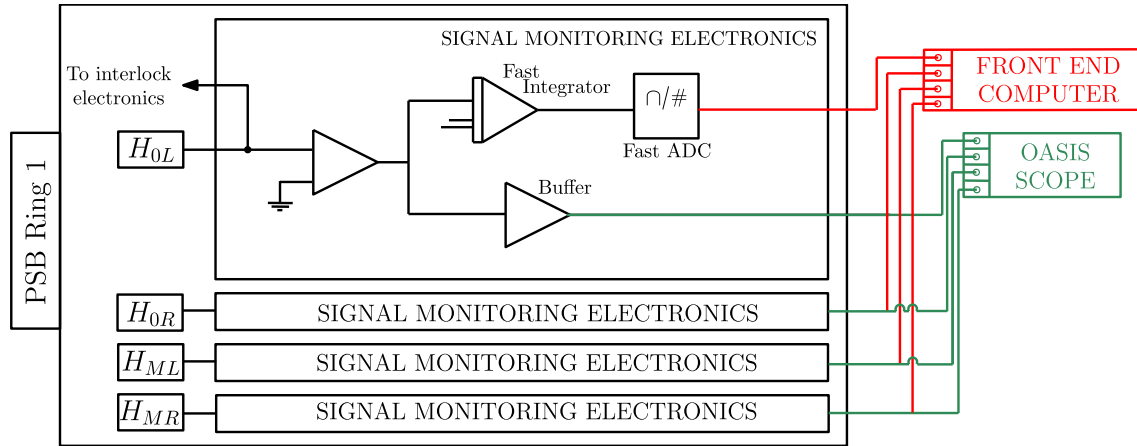


Figure 7.6: Schematic diagram of the signal monitoring electronics.

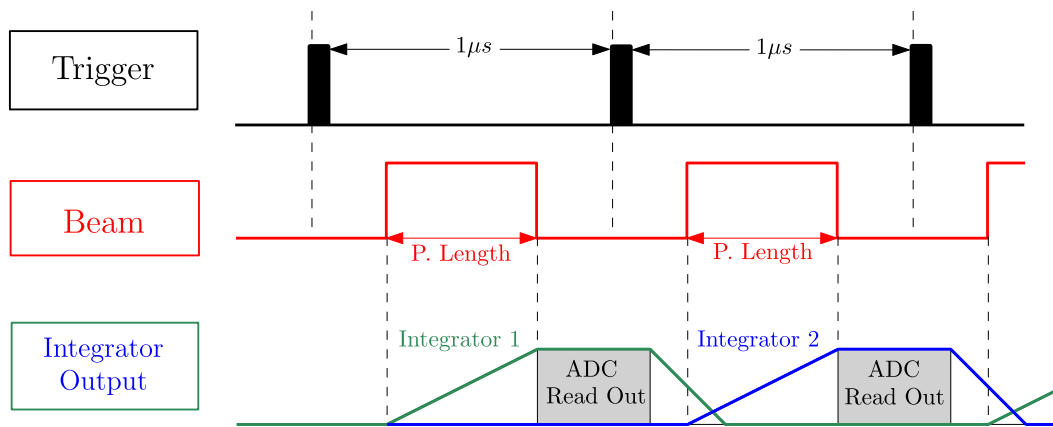


Figure 7.7: Time logic of signal monitoring circuit.

7.4 Interlock Circuit

The objective of the interlock circuit is to generate an interlock signal that will protect the H^0H^- dump. Fig. 7.8 shows the schematic representation of the interlock circuit. In this case, the current coming from each plate is fed to a slow and low-gain amplifier. The outputs from each amplifier serve as parallel input to a slow integrator. The integrator output goes to a comparator, that has the purpose of checking if the total sum is above or below a certain threshold. If the sum is above the threshold, the circuit generates an interlock signal.

The threshold of the comparator can be set via software and was defined after the calibration of the system. If a signal above the threshold is detected in any of the rings, the interlock card sends a FALSE signal to the dedicated CIBU (User System to Beam Interlock System Connection) [88]. The estimated response time between the interlock detection and the beam dumping is around $10\mu s$. After each interlock occurrence, the interlock card keeps the FALSE output until the operator uses the RESET command.

In parallel to the comparator, the analog integrator output is also connected to a slow ADC and to an independent scope connector to allow for different ways of monitoring the interlock electronics.

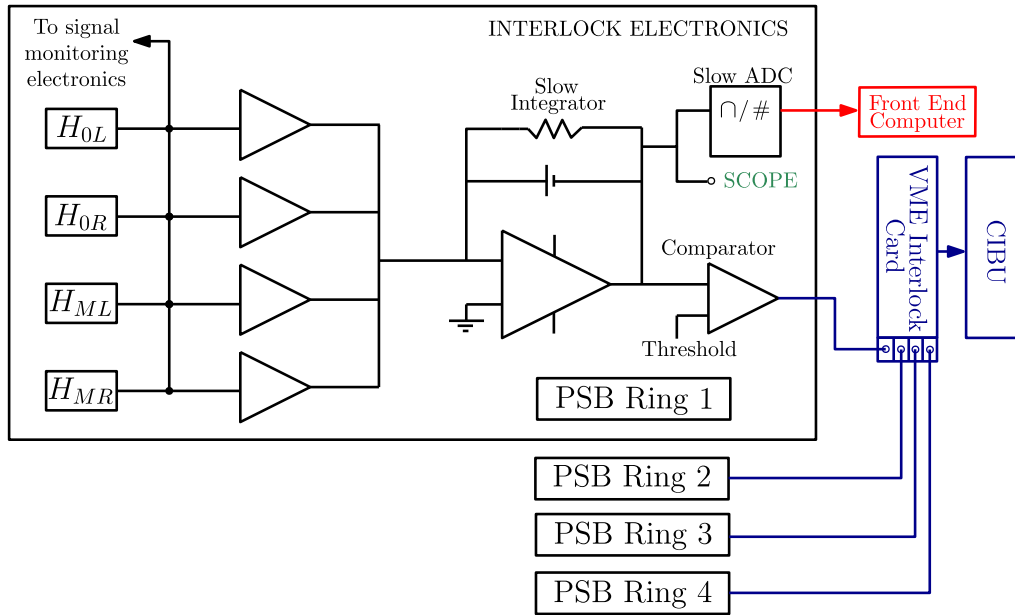


Figure 7.8: Schematic diagram of the electronic circuits for the interlock system.

7.5 Read Out Signals

As aforementioned, several types of signals from the monitors can be accessed. Here we call them: OASIS Signals, Plate Signals and Interlock signals.

7.5.1 OASIS signal

The Oasis Scope Signal, or simply the OASIS signal, shows the analog current measured by the plates after a fast amplification. It allows for real-time monitoring. Fig. 7.9 shows an example of the signals measured with the OASIS scope.

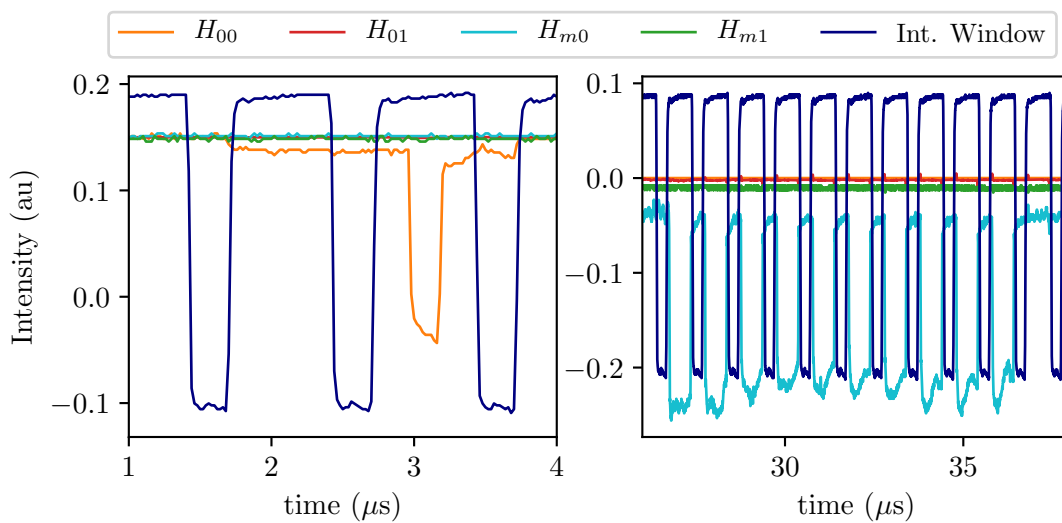


Figure 7.9: Example of OASIS signals. Left: Single turn, pulse length 200 ns, focused on H0L plate. Right: 10 turns, pulse length 620 ns, focused on HML plate.

The figure on the left shows an example of a signal produced by a single bunch injection. On the right, a multiple-turn injection signal is shown. In both these pictures, one can observe the signal measured by the four plates. In both cases, the beam of particles was centered on one plate (left: H0L plate; right: HML plate). Depicted in dark blue, one finds the Integrating window signal. Positive readings of this signal mean that the plate signals are being integrated.

7.5.2 Plate Signal

Fig. 7.10 shows an example of Plate signal. The plate signals refer to the signal registered by each plate after it has been integrated and digitalized. In this figure, different colors indicate different beam conditions. In general, longer beam pulses will result in larger integrated signals (in absolute value) as more charges are being integrated during the same integration window. On the other hand, the larger the number of beam turns, the larger the number of points with integrated charge.

If we look again at Fig. 7.9, one can notice that the Plate signals of the left and right plots would be very different. The left plot would yield a single point with a signal in the plate signal measurement. Whereas the left plot will yield ten points with signal and each one of them with a larger absolute current. The plate signals are systematically stored in the NXCALS database and can be accessed for proper offline data analysis.

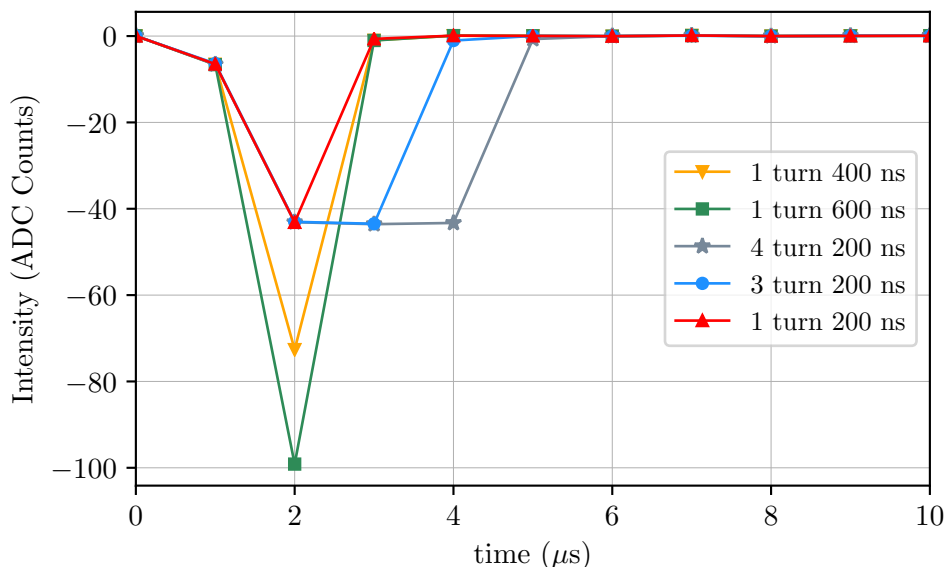


Figure 7.10: Example of Plate signals for different beam conditions.

7.5.3 Interlock Signal

The interlock electronics also had access to an OASIS scope, however, it was rarely used during the measurements. The interlock signal was generally monitored in the front-end computer, after the integrator and ADC. Fig. 7.11 shows some examples of measured interlock signals. Stored in the database is also the signal from the comparator. This is a boolean type signal, indicating whether or not an

interlock was generated. In Fig. 7.11, the red signals correspond to cases where the beam was interlocked due to measured signals surpassing the safe threshold.

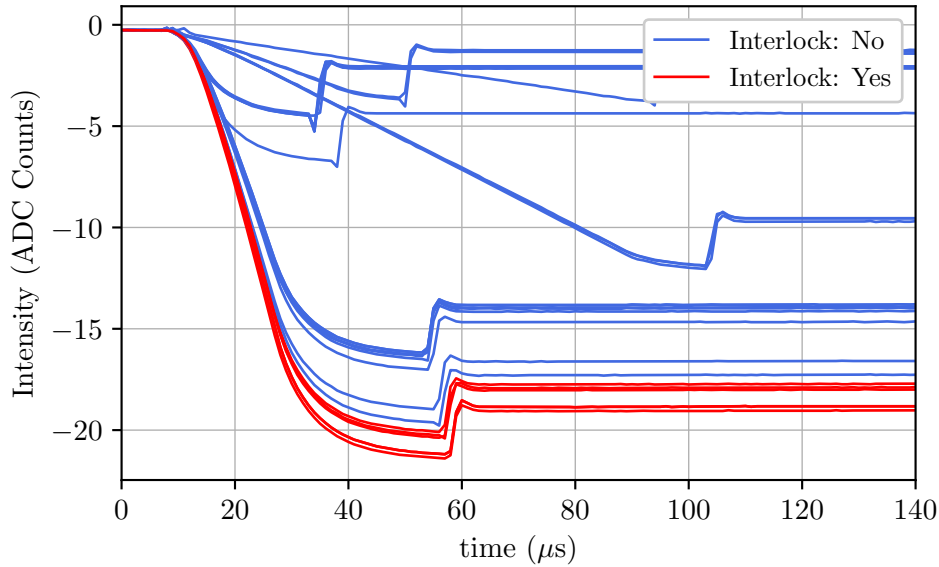


Figure 7.11: Several examples of interlock signals.

7.6 Calibration

7.6.1 Objective and Procedure

The signal generated in the plates is proportional to the number of unstripped particles. However, due to the complicated electronics implementation, the physical meaning of the "number of particles" is lost when reading the signals in front-end computers. It was of great importance to recover this information, to fully exploit the potential of the detectors. For that reason, a calibration campaign was launched.

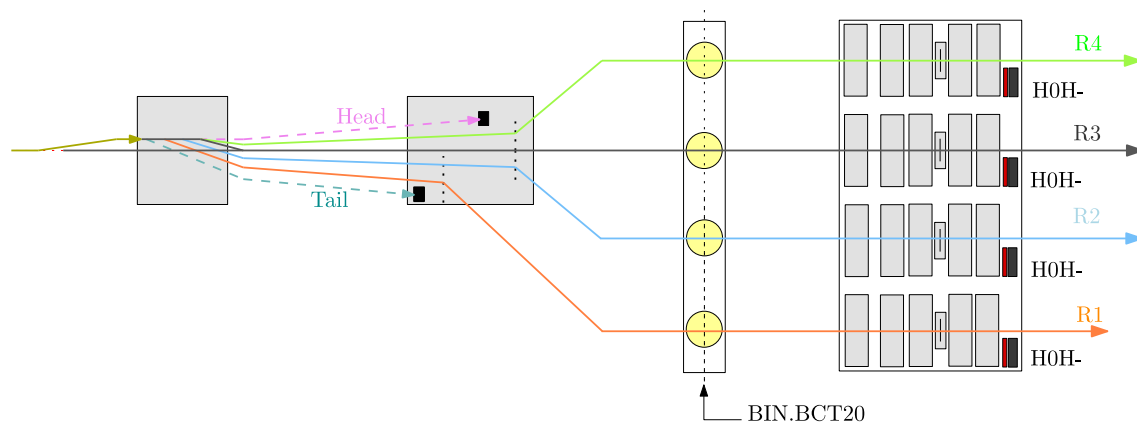


Figure 7.12: Schematic representation of the BCT (in yellow) location on the beam line.

The main objective of this calibration was to obtain a calibration factor (R_{cal}) that correlated the ADC counts (Obtained as an output of the electronics) with the

total number of particles reaching the dump. This calibration factor was calculated for the Plate Signals, and it had to be calculated independently for all the plates in all the booster rings. The calibration was performed with an H^- beam of particles, that is, without stripping foil. In this way, the calculated factor was not dependent on the stripping efficiency of a given foil. Also, the negative nature of the H^- particles facilitated the beam's focusing and guidance. The electronics are optimized for measuring a maximum of 10% of the Linac4 beam intensity. For that reason, a beam of reduced intensity ($I_{beam} \sim 4$ mA) was used for the calibration.

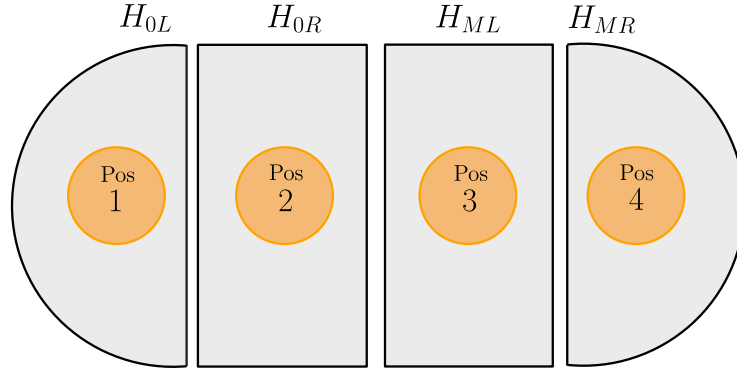


Figure 7.13: Schema of the order followed during the measurements.

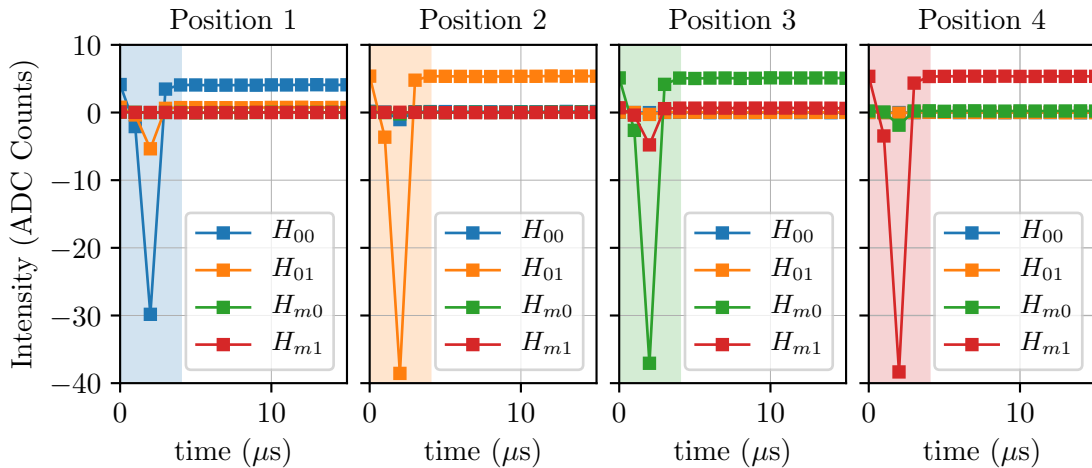


Figure 7.14: Example of measurement taken during a scan in Ring 2. Shaded area, integration window for the total charge calculation.

An independent measurement of the number of particles reaching the dump was measured with a beam current transformer. The BCTs used for the calibration were placed after the distributor, before the charge exchange injection. Fig. 7.12 shows a schematic representation of the BCTs location on the beamline. The calibration measurements were taken on several different days and under different beam conditions. However, the measurement procedure was always the same. The beam of particles was focused individually in each plate, from "left" to "right", thanks to BSW3 and BSW4 and other kicker magnets (see measurement sequence indicated in Fig. 7.13).

The calibration factor was calculated by taking the integral of the plate signal and comparing the results with the total number of charges measured by the BCT

in each case. A mathematical description of this calibration factor can be written as:

$$R_{cal} \left[\frac{Charge}{ADCcounts} \right] = \frac{Signal\ BCT}{Signal\ Plate} \cdot C_f \quad (7.1)$$

Here, C_f stands for correction factor, and it will be covered in the next section. A sample of the plate signal measurements, taken during a scan at Ring2, are shown in Fig. 7.14. In this case, a beam pulse of 200 ns and 1 Booster turn were used for the calibration. From this figure, one can see that the four plates seem to give very similar measurements. To compare the results with the BCT measurements, the integral of this signal along the shaded area was calculated.

7.6.2 Correction Factor

To properly compare the measurements taken with the different plates to the BCT measurements, some corrections must be applied. These corrections are: offset corrections, beam displacement effects and tail/head beam effects.

Background Correction

The plate signal measurements seem to suffer base-line displacements when a non-negligible current is measured. This is corrected by subtracting the average of the measured signal after the beam passage. See Fig. 7.15 for an example of background subtraction. In this example, a 200 ns beam pulse with 4 Booster turns was measured. The beam of particles was focused on the H_{0L} plate. The shaded area indicates the part of the signal that was used for background corrections. If a beam of particles with a very large number of turns was measured, the background window was adapted correspondingly.

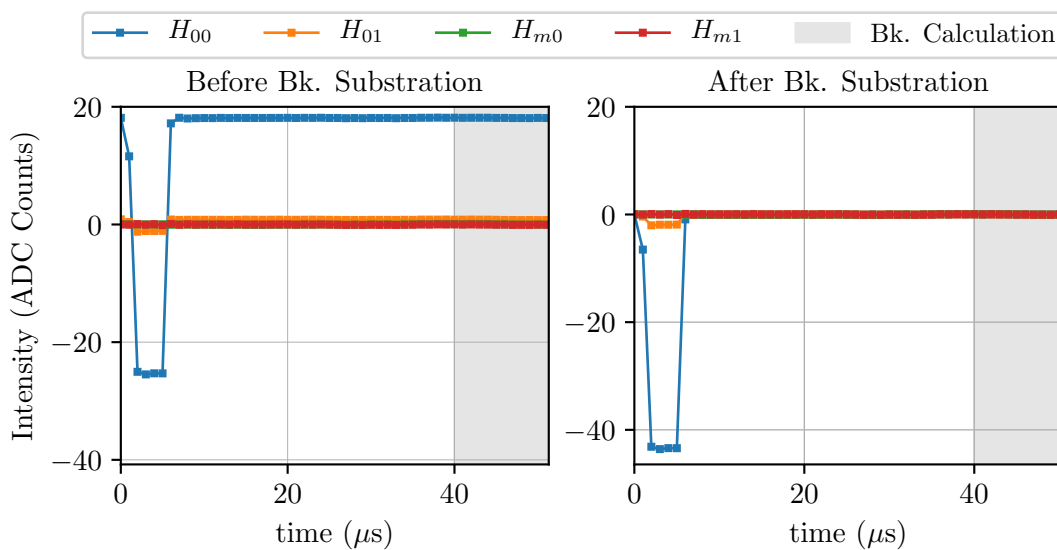


Figure 7.15: Example of background correction. Left: Before correction. Right: After correction

Beam displacement effects

The calibration was done for each plate at a time, by focusing the beam on each of them individually. However, in some cases, we were unable to fully focus the beam on a single plate. See Fig. 7.16 for an example of a not fully centered beam. In this case, the beam was supposedly centered on H0L, however, a small current intensity could be measured on H0R. because the intensity measured by the BCTs is the total intensity of the beam, one can't compare directly the signal measured by a single plate with the BCT signal. First, a correction factor (C_f) was applied:

$$C_f = \prod_m \cdot \frac{H_n}{H_n + H_m} \quad (7.2)$$

With H_n being the calculated integral on plate n, and H_m the calculated signal on adjacent plates. This might be an overly complicated way of compactly writing a mathematical expression for the C_f . As an example, one could calculate the C_f of Fig. 7.16 as follows:

$$C_f = \frac{H_{0L}}{H_{0L} + H_{0R}} = \frac{-181.033}{-181.033 - 7.930} = 0.958 \quad (7.3)$$

It is important to note that for the two central plates one might need to calculate a correction factor for the two adjacent plates.

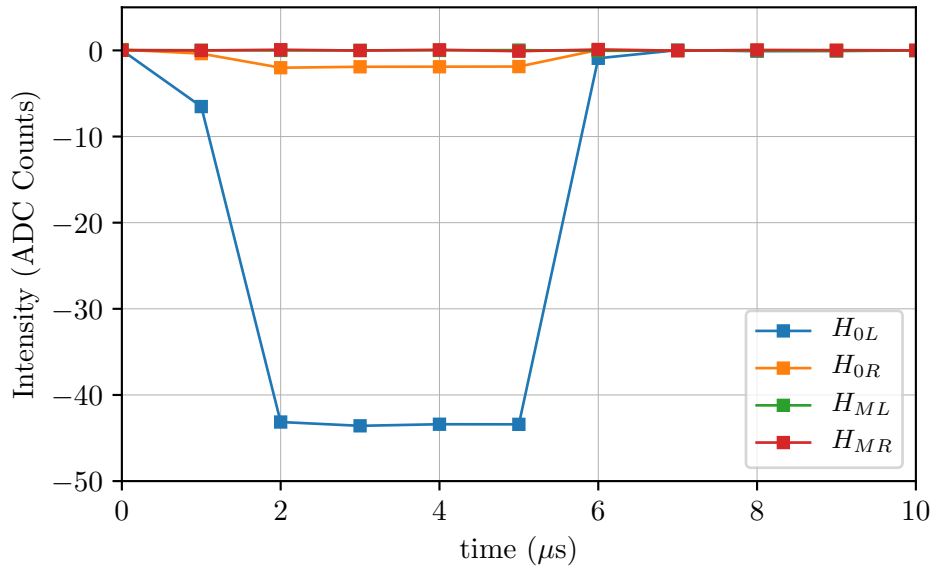


Figure 7.16: Example of beam displacement effect, for a 4 turn, 200 ns beam.

Tail/Head Beam Effects

In ideal conditions, the bunched beam of particles has a rectangular current profile in the longitudinal space [89]. However, being the world not ideal, we could observe some variations from this rectangular shape. We will call the head of the beam those particles that arrive before the particle bunch and the tail of the beam those particles arriving after the expected bunch.

Fig. 7.17 shows an example of intensity measurement taken with BCT20 at Ring3. The BCT signal that we use for calculating the calibration factor corresponds to the integral inside the orange window of this signal. From this figure, one can see that the beam head is outside the assigned integration area.

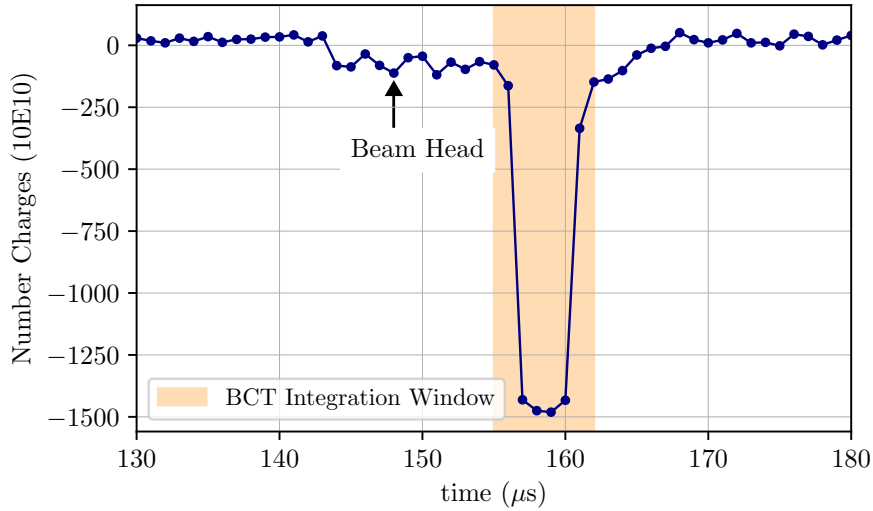


Figure 7.17: Example of BCT measurements, number of charges with time.

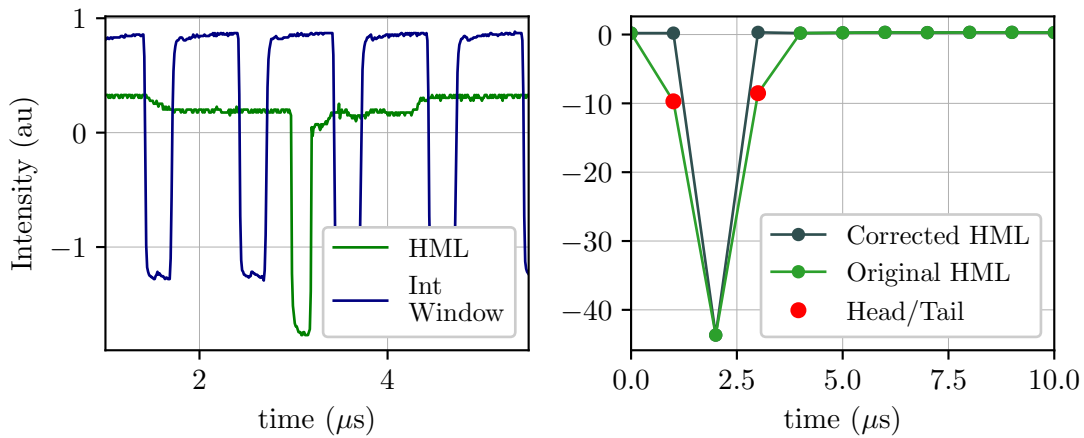


Figure 7.18: OASIS (left) and Plate signal (right) for a measurement particle beam centered in HML plate. Non-negligible head/tail effects.

To visualize the head-tail effects on the H^0H^- monitors we need to look at the OASIS signal. Fig. 7.18 shows an example of OASIS signal measured by the plates (left) and its corresponding Plate Signal (right). In the OASIS signal, one can easily identify the beam signal as well as the head and tail of the beam. In Sec. 7.5.1 we explained that whenever the integration window signal was positive, the signals measured by the plates were being integrated. This means that, in the digitalized plate signal, the points immediately before and after the beam pulse correspond to the integral of the beam head and tail (indicated in red in Fig. 7.18 right.). Before calculating the integral of the Plate signal, and compare it to the BCT, it is

necessary to correct these points. In Fig. 7.18 (right) one can observe the results of this correction in the plate signal. This effect was particularly important in Ring4.

7.6.3 Results

200 ns, 1 Injected turn

The calibration was performed with different beam conditions, different pulse lengths (from 200 ns - 700 ns) and a different number of booster-injected turns (1 turn - 4 turns). The measurements of beam intensity remained very stable during all the measurements, with an intensity variation of 2%. Fig. 7.19 shows the measured beam intensity in the different rings during the measurements of a 1 turn, 200 ns beam pulse.

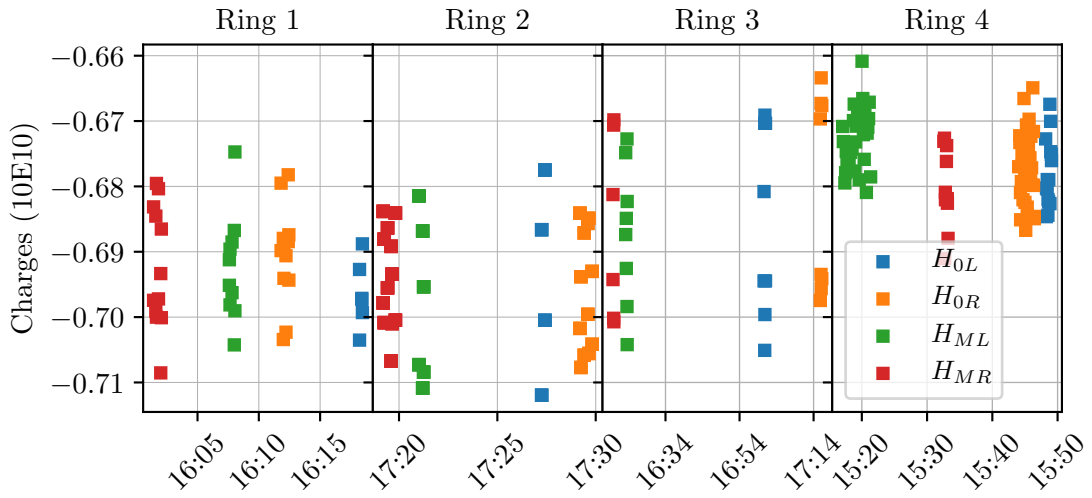


Figure 7.19: Number of charges measured by BCTs during the plate signal calibration. For 1 injected beam turn and 200 ns beam pulse. Different colors indicate the different plates the beam was focused on.

Table 7.3 shows a summary of the calibration factor results for 1 turn, 200 ns particle beam. From these results, one can observe that all the integrated plate signals are negative, and around -43.617(10) ADC counts. With H0R plate in Ring 2 being the only outlier. Unfortunately, due to a lack of time, this measurement could not be repeated. The correction factor (C_f), which accounted for beam displacement effects, are all well above 80%, indicating that the beam was properly centered in the calibration plate. All the calibration factors in this case, agree around a value of $R = 1.521(24) \cdot 10^8$ (Charges/ADC count), with H0R in Ring2 again as an outlier.

Beam Pulse Length and Number of Injected turns

Because the calibration factor is calculated by normalizing the signal in the plate with the BCT signal, a change in the beam pulse length or the injected number of turns should not affect the value of the calibration factor. This assumption was carefully cross-checked. Fig. 7.20 left, shows the charges measured by the BCT for different beam pulse lengths (from 200 ns to 700 ns), and a constant 1 injected turn.

In this figure, one can observe four groups of points. A longer beam pulse implies a larger number of beam charges in each pulse, and thus a larger negative signal.

		H_{0R}	H_{0L}	H_{MR}	H_{MR}
Ring 1	Int	-43.215(90)	-43.932(69)	-43.763(42)	-43.675(29)
	C_f	0.952(1)	0.998(2)	0.957(1)	1.0
	R	1.534(10)	1.568(15)	1.514(17)	1.585(20)
Ring 2	Int	-33.588(31)	-43.925(28)	-42.368(16)	-43.748(51)
	C_f	0.844(3)	0.971(2)	0.892(4)	0.954(3)
	R	1.745(38)	1.539(20)	1.470(24)	1.514(15)
Ring 3	Int	-43.955(15)	-23.42(74) ⁽¹⁾	-43.814(80)	-44.190(16)
	C_f	0.9508(2)	0.535(16) ⁽¹⁾	0.9677(7)	1.0
	R	1.482(29)	1.565(31) ⁽¹⁾	1.517(22)	1.552(29)
Ring 4	Int	-43.367(50)	-43.638(48)	-	-43.429(32)
	C_f	0.932(1)	0.967(1)	-	0.955(1)
	R	1.459(8)	1.502(1)	-	1.497(13)

Table 7.3: Summary of calibration factor results for 1 turn, 200 ns particle beams. The row Int refers to the integral of the plate signal, with units of ADC counts. ¹ was calibrated with the particle beam centered in between H_{0R} and H_{0L} , thus the 0.535 calibration factor.

Similarly, the BCT measurements for a 200 ns beam pulse length and various injection turns are shown in Fig. 7.20 right. Also, in this case, a larger number of injected turns induces a larger negative signal. This tendency was also observed in the Plate signals, however, differences in the pulse length - measured intensity slope (or number of turns - measured intensity slope) between the BCT and the Plate signal measurements, yielded a non-negligible linear dependency of the calibration factor with these properties. Fig. 7.21 shows the calibration measured calibration factor as a function of beam pulse length (left) and number of injected turns (right).

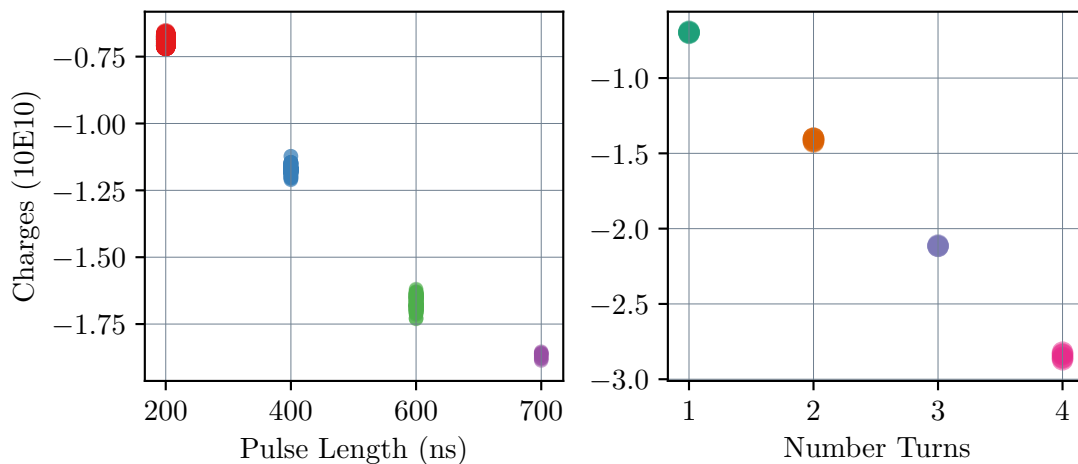


Figure 7.20: Number of charges measured by the BCT during Ring1 calibration. Left: for 1 injected beam turn, different beam pulse lengths. Right: For a 200 ns beam pulse length, a different number of turns was injected.

The issue was attributed to mismatches with the integration windows. The

maximum length of the integration window for the plate signal is around 650 ns. If the pulse length is longer than that, part of the pulse is not integrated, resulting in a larger calibration factor. In normal operations, beam pulse lengths should not be larger than 600 ns. A clear physical explanation for the linear dependency of R_{cal} with the number of turns was not found. Nevertheless, the relative error induced due to this linearity is smaller than 1.5%, so it was not considered to be a critical source of error.

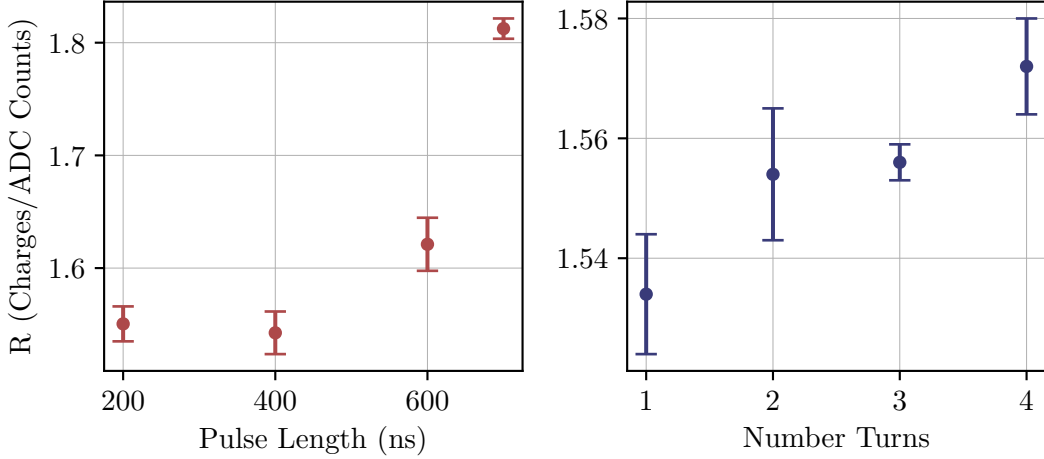


Figure 7.21: Comparison of calibration factors calculated for different beam conditions. Left: for 1 injected beam turn, different beam pulse lengths. Right: For a 200 ns beam pulse length, a different number of turns was injected.

Effects of BSW4 magnetic field

As indicated in Sec. 7.1, the H^0H^- monitors are placed inside BSW4 magnetic field, e.e. they are exposed to a constant magnetic field of ~ 0.18 T. During calibration, BSW4 was able to be turned on and off at will. This allowed us to study the effects this magnetic field had on the intensity measurements. Without the magnetic field of BSW4, the beam could not be focused on the HMR, HML plates.

The intensity of the magnetic field is enough to suppress the SE produced during the interaction of the particle beam and the plate surface. As explained in Ch. 2, SE will provide a positive contribution to the total current. This means, that if there is secondary emission, a smaller signal (in absolute value) is registered by the plates. A smaller signal in the plates implies a larger calibration factor, as the BCT measurement will remain the same independently of the BSW4 state.

This effect can be observed in Fig. 7.22, where the comparison of the calibration factors calculated with and without BSW4's magnetic field is shown. The average calibration factor with magnetic field is $R_{cal} = 1.51(2)$ whereas the calibration factor without magnetic field is $R_{cal} = 1.91(2)$. This is a 26.49% difference between the values. From table 7.2 we can observe, that the predicted values for the charge formation in the plates, with and without SE, differ a 32.28%, which is consistent with the measured results. In normal operation conditions, the magnetic field of BSW4 is always present.

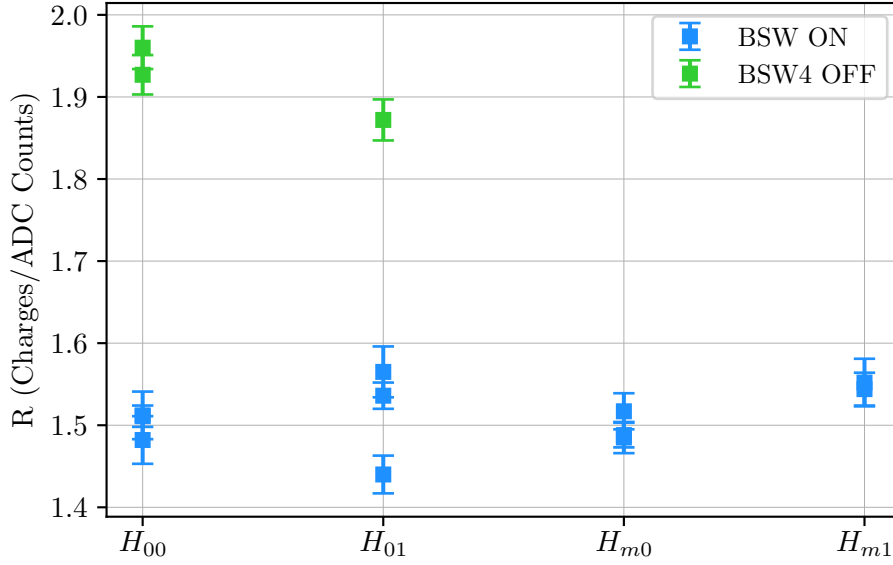


Figure 7.22: Comparison calibration factor with and without BSW4 magnetic field.

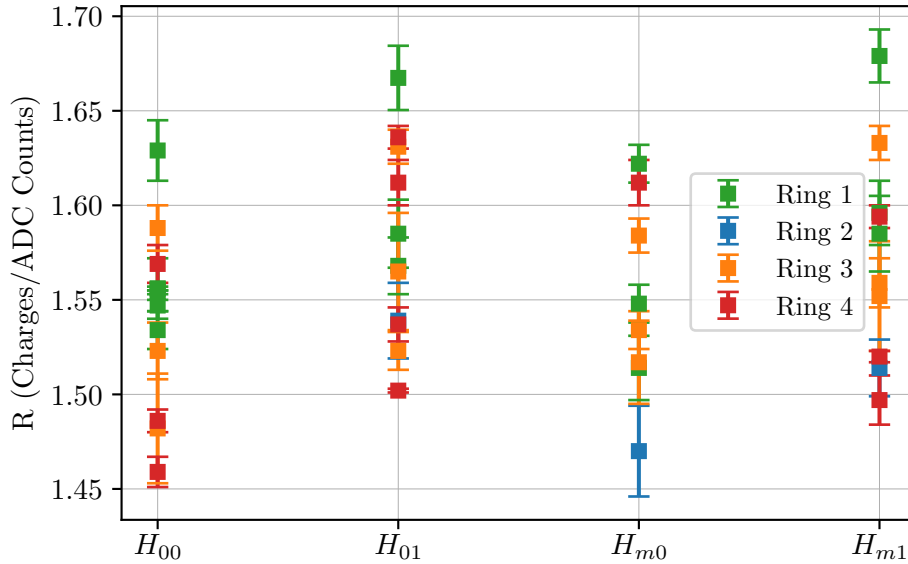


Figure 7.23: Summary of the calibration factor measurements.

Results Summary

Fig. 7.23 shows the summary of the calibration factor measurements. It comprises the measurements taken in all the plates, all the rings, and different beam conditions. From this figure, one can observe that all the measurements seem to agree on a calibration factor of:

$$R_{cal} = 1.56 \pm 0.033 \cdot 10^8 \left(\frac{\text{Charges}}{\text{ADCcounts}} \right) \quad (7.4)$$

With a confidence error smaller than 3.5%. This calibration factor was included in the software specifications of the H^0H^- monitors so that currently the total number of unstripped particles is continuously available. After the detailed calibration,

the monitors became operational. They have continuously been used since April 2021, and have proven to be a really valuable part of the machine operation.

7.7 Stripping Inefficiency Calculations

Once calibrated, these detectors could be used to monitor changes in the stripping inefficiency. On April 2021, a systematic set of measurements was performed to observe the behavior of different types of stripping foils under different beam conditions. Six stripping foils were installed in the loader or Ring3 to observe their behavior under different beam conditions. Table 7.4 shows the characteristics of the different foils tested during the measurements.

Foil Number	Type	Weight	Description
1-4	XCF-200	200 mu g cm2	Arc evaporated amorphous Carbon
2-5	MLG-250	240 mu g cm2	Multilayer Graphene
3-6	GSI-200	200 mu g cm2	Arc evaporated amorphous Carbon

Table 7.4: Characteristics of the measured stripping foils.

Fig. 7.24 shows the values of the stripping inefficiencies as a function of time, calculated with the H^0H^- monitors. The stripping inefficiency was calculated every microsecond. However, for the sake of visualization, only some of those points have been depicted.

The stripping foils in the loader are assigned a number. In Fig. 7.24 the black line represents the stripping foil number, meaning which stripping foil was inserted at each time. The abrupt changes in this line indicate a change in the stripping foil. One can observe that changes on the stripping foil are very much aligned with the changes on the measured stripping inefficiency.

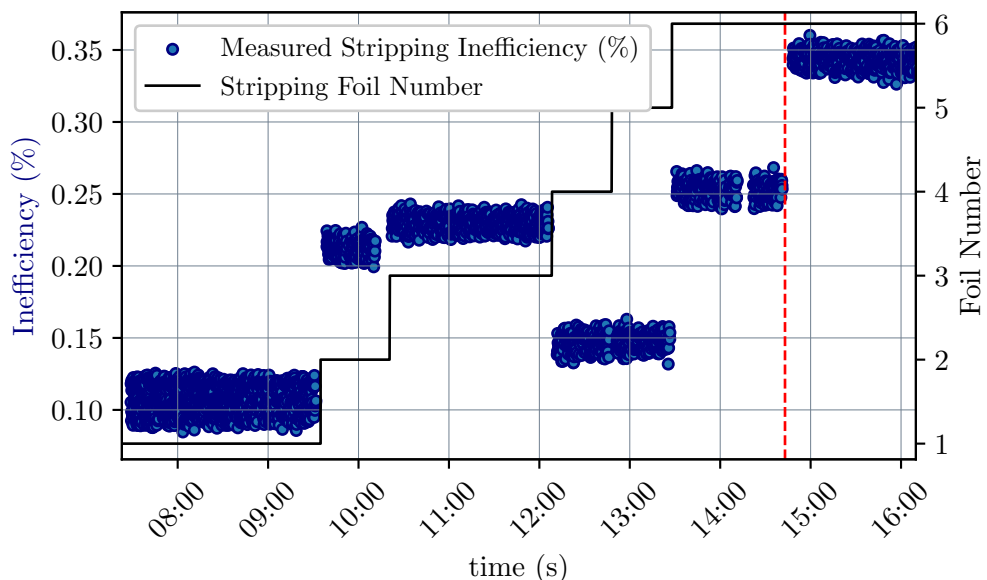


Figure 7.24: Calculated stripping inefficiency during stripping foil tests.

Fig. 7.26, shows a histogram projection of these inefficiency measurements. The measured stripping inefficiencies are very small, of the order of 0.2%. Even in this

situation of a low current measurement regime, the measurement uncertainties are small enough to distinguish between foils.

Another very interesting feature that could be observed during these tests was the stripping inefficiency increase during foil degradation. A stress test was performed on Foil 6. The foil was continuously monitored while the beam intensity (bema number of turns) was steadily increased to determine whether the foil could resist the beam conditions.

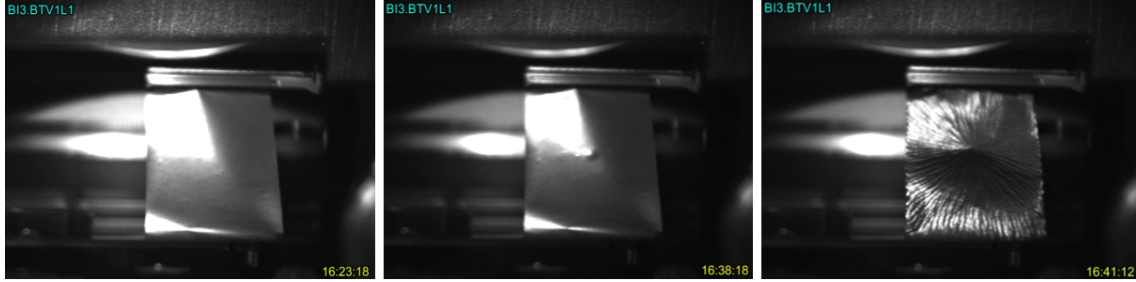


Figure 7.25: Stripping foil pictures during degradation studies.

In picture 7.25 one can observe a picture of the foil at three different stages of the test. The first picture was taken at the beginning of the measurements, and no clear deformation can be observed. The central picture was taken when the injected number of turns was 120. In this case, a small local deformation starts being visible. When 130 beam turns were injected, a sudden deformation occurred, as can be seen in the picture on the right.

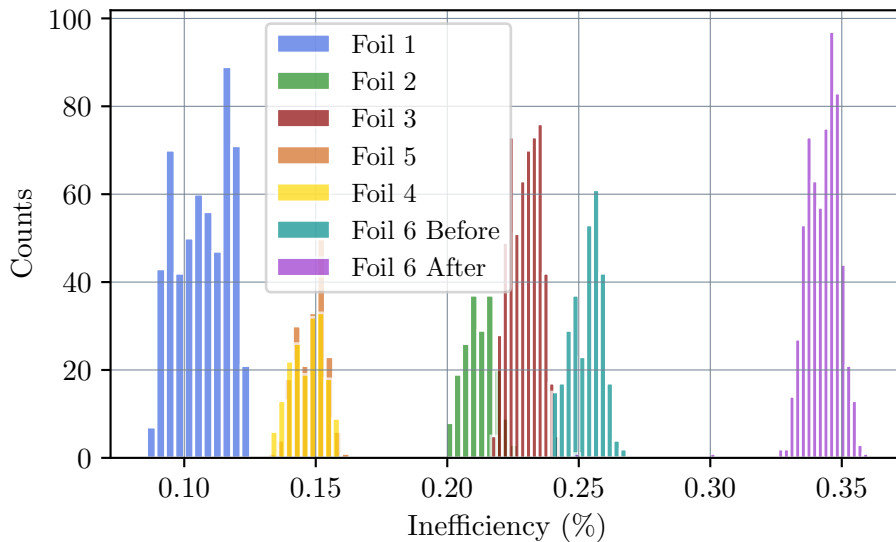


Figure 7.26: Histogram representation of the calculated stripping inefficiencies during stripping foil tests.

This big deformation could also be observed in the stripping inefficiencies measurements. The red dotted line in Fig. 7.24 indicates the exact time when this deformation occurred. The change in the stripping inefficiency is obvious and it can more clearly be observed in 7.26 with the before and after histograms. The quantitative values of the stripping foil inefficiencies were subjected to some uncertainties in the measurements, such as beam positioning conditions, possible non-registered

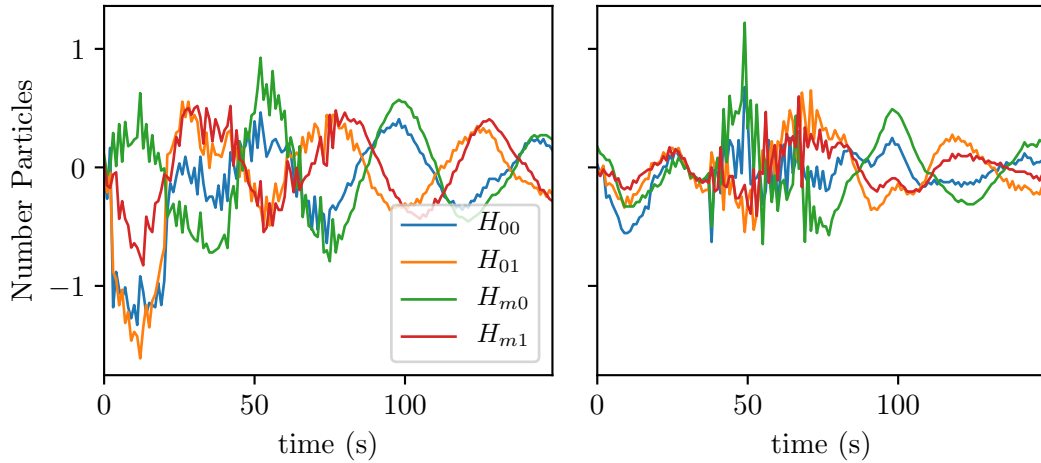


Figure 7.27: Plate signals measured during normal operating conditions. Left: With beam injection. Right: No beam injection.

beam losses, uncertainties in BCT measurements, etc. So the quantitative values of the stripping inefficiency should be taken with a grain of salt. Nevertheless, the relative differences between the registered stripping inefficiencies are clear, proving the high sensitivity of the stripping inefficiency measurements.

7.8 Noise Problems

One of the biggest challenges faced by the H^0H^- current monitor after the calibration was related to electronic interferences. Due to the controlled environments in which the calibration process was carried out, the little impact of noise in the signals could be seen.

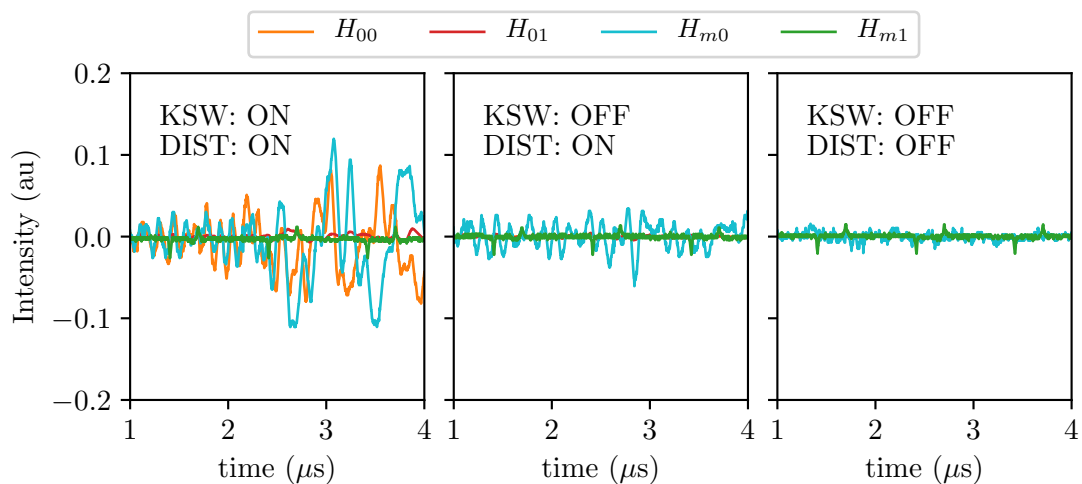


Figure 7.28: Effects of KSW and Distributor in electrical noise signals. Background measurements, no beam. Left: KSW on, Distributor On. Center: KSW off, Distributor Off in the current ring but on in other rings. Right: KSW off, Distributor Off in all rings.

However, during normal operation, a clear electronic noise was observed. Fig. 7.27 shows some examples of Plate signal readouts taken in normal operating conditions. From this figure, one can already see that the noise signals are not negligible. In addition, since the calibration of these detectors in March 2021, several non-physical interlock signals have been reported. These interlocks were attributed to the integration of electronic noise. To avoid these fake interlock signals, it became crucial to minimize the electric noise in our system. Two types of noise were identified, a high-frequency noise and a low-frequency noise.

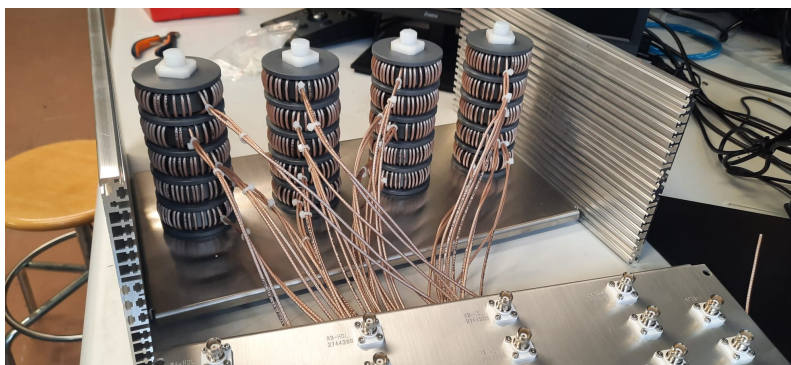


Figure 7.29: Picture of the ferrites installation for noise mitigation before H^0H^- VEME card.

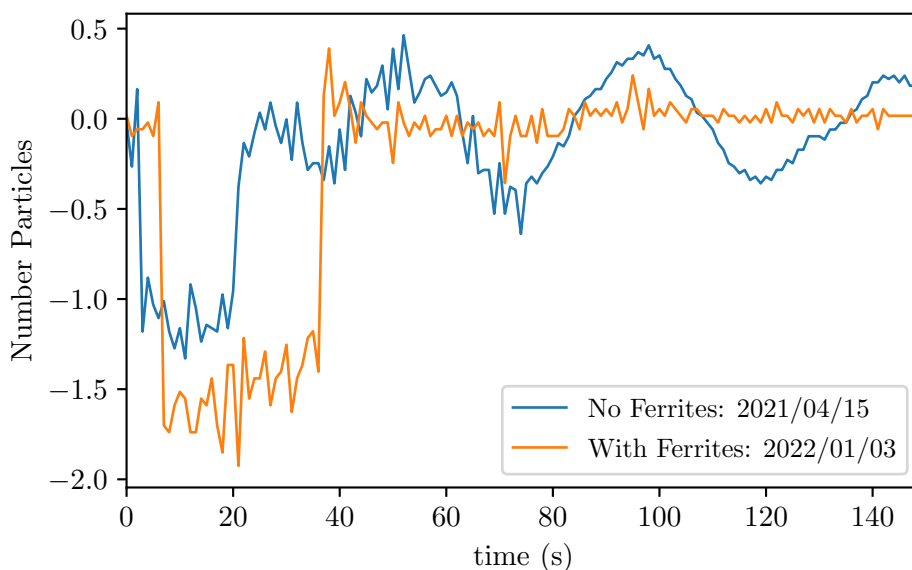


Figure 7.30: Effects of the ferrite installation on the H^0H^- signals.

The high-frequency noise is related to the decaying current of the KSW magnets and the distributor. Fig. 7.28 shows the effects these two devices have on the plate signal, where measurements with no beam were taken. It was also observed, that KSWs and distributors of a certain ring were affecting the measurements in other rings. Unfortunately, during normal operation, these devices will always be working, and there is little one can do to improve the generated noise.

As far as the low-frequency noise is concerned, the origins of the noise are quite unclear. However, thorough investigations were performed to minimize this noise.

Ferrites [90] were installed at the arrival of the H^0H^- beam current monitor signals from the tunnel, just before the VME input. Fig. 7.29 shows a picture of the installed ferrites. The installation of these devices improved the noise-signal ratio, as can be seen in Fig. 7.30. In this figure, the beam conditions for the measurements before and after the ferrite installation were quite different, so the beam signals cannot be directly compared. However, the effects of noise mitigation thanks to the installation of these devices are obvious.

Chapter 8

SEM Grid Testing at GSI

In June 2022 a dedicated set of measurements were performed in GSI (Darmstadt, Germany) for the commissioning of two SEM grid prototypes. The design and production of the SEM Grids were performed by the company PROACTIVE R&D [91]. In this chapter, we shall discuss the motivation of the experiment and the experimental details and conditions. This is followed by a summary of the most relevant results. Part of these results have been already presented in LINAC2022 [92] and in IBIC2022 [93].

8.1 The FAIR project and UNILAC

The GSI Helmholtz Centre for Heavy Ion Research is a heavy ion research center in Darmstadt, Germany. The main focus of the GSI research program is the basic investigation in the field of nuclear physics and atomic physics [94]. Fig. 8.1 shows a schematic representation of the GSI accelerator complex. GSI is unique among research facilities worldwide in that it can generate positively charged ions of many different naturally occurring elements, from protons to uranium.

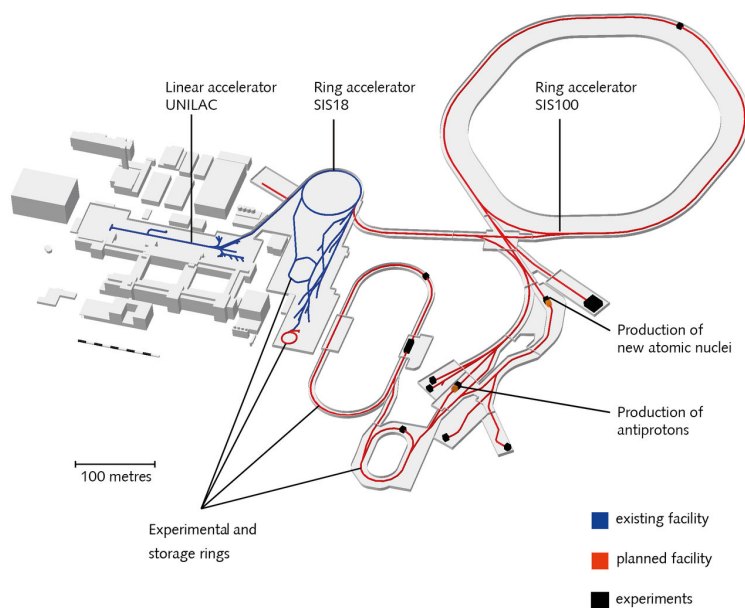


Figure 8.1: Layout of the GSI + FAIR accelerator facility.

The process begins at the linear accelerator UNILAC (The UNiversal Linac ACcelerator), where the different types of ions are produced. Fig. 8.2 shows a more detailed schematic representation of GSI's UNILAC accelerator. Two of the ion sources are placed at the beginning of the LINAC and one is placed in the middle. After the extraction from the source, the dc-beam is bunched and pre-accelerated by the RFQ, and then accelerated along the Inter-Digital (IH) cavities up to 1.4 MeV/u.

In some cases, before the next accelerator step, the ions are passed through a gaseous medium to strip them off the outer electrons and thus augment the ion charge state of the beam. The final energy of 11.4 MeV/u is achieved using five Alvarez-Type cavities [95]. A unique feature of the UNILAC is that some of the Alvarez-Cavities can be operated without acceleration, hence also energies of 3.6, 4.8, 5.9 and 8.6 MeV/u can be provided.

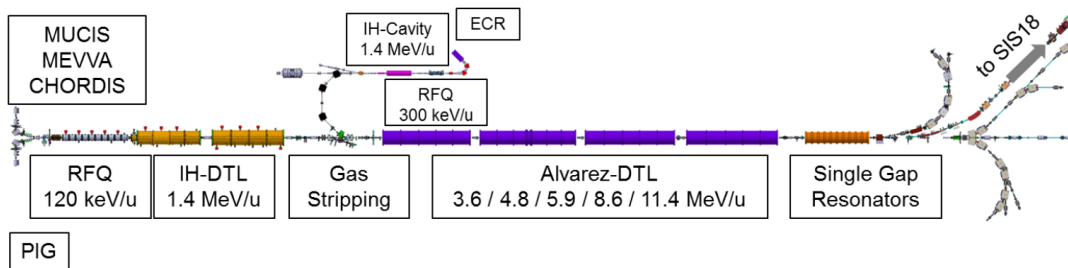


Figure 8.2: Schematic representation of UNILAC accelerator.

After the UNILAC, the beam can be directed to the experimental Hall (EH) or injected to the transfer line (TK), which can provide an additional stripping foil and charge state separation of heavier ions for the future injection to the heavy ion synchrotron SIS18. SIS18 is a versatile synchrotron, with a circumference of 216 m. In SIS18 the ions are accelerated to adjustable energy whose peak value depends on the mass-to-charge ratio of the particle beam.

To accommodate the demand for higher beam energy and intensity for more advanced physics experiments, the international Facility for Antiproton and Ion Research (FAIR) is currently being constructed at GSI [96]. FAIR will include three linear accelerators: UNILAC, a superconducting cw-Linac [97] and the new proton Linac (pLinac) [98]. The UNILAC and pLinac will be the main injectors of SIS18, which will in turn be an injector for SIS100, the central accelerator component of FAIR. It is planned for the pLinac to deliver a current up to 70 mA with a macro-pulse length of 35 μ s (at max. 4 Hz) and a typical bunch length of 100 ps. The design energy is 68 MeV. Special care has to be taken for the design of the diagnostics for this accelerator due to the challenging beam conditions. The overall diagnostics concept and layout of pLinac have been described in various reports, e.g. [99].

8.2 Motivation and Experimental Conditions

To measure the transverse beam profile in the future pLinac, the traditional SEM grid design of GSI (64 wires with 2.0 mm spacing) had to be modified. For that, a new set of grids for the pLinac were designed by PROACTIVE R&D company

in collaboration with GSI. To test the two newly designed SEM grid Prototypes two measuring campaigns were performed. In the first campaign, a low-intensity proton beam was used to prove the correct function of the Grid in connection with the POLAND + CSA electronics [100]. In the second campaign, which took place in June 2022, a high-intensity Argon beam was used to mimic the pLinac beam conditions.

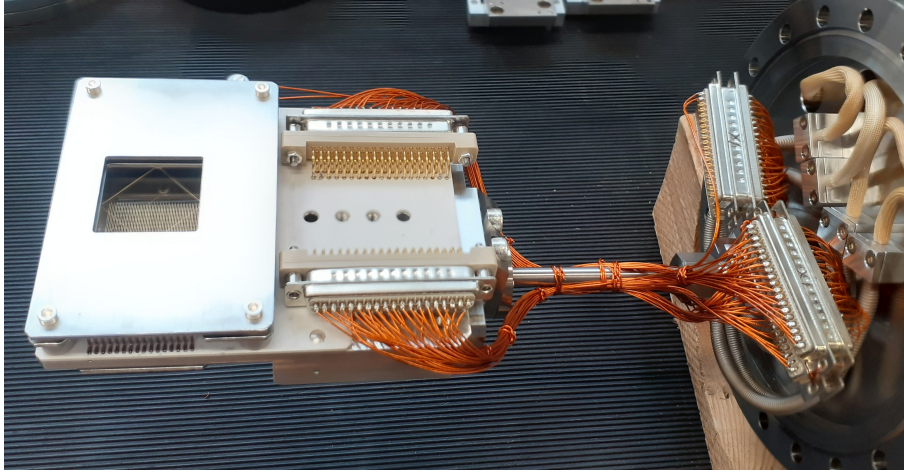


Figure 8.3: SEM grid by PROACTIVE R&D.

Two SEM grid prototypes were tested. Fig. 8.3 shows a picture of one of the SEM grids tested during these measurements. Both SEM Grids had 64 wires, with a wire spacing of 0.5 mm. The active area is $32 \times 32 \text{ mm}^2$. The only difference between the SEM grid prototypes was the wire material. One grid had $100 \mu\text{m}$ gold-tungsten wires (we will call it Grid1). The other grid had $100 \mu\text{m}$ pure tungsten wires (we will call it Grid2).

Besides the high resolution and compact design, special care was taken for the implementation of the diamond-shaped cleaning electrode. These electrodes are kept to a positive potential to enhance secondary emission and prevent the emitted SE from being captured by neighboring wires. The electric field distribution and the optimal potential required were studied in detail as shown in [101]. Moreover, a specially designed stretching system is used PROACTIVE grids to keep the wires under tension during irradiation.

Ion	Energy (MeV/u)	Intensity (mA)	Pulse Length (μs)	Rep Rate (Hz)
Ar^{10+}	8.6	0.04 - 1.5	40 - 200	1

Table 8.1: Summary of beam conditions for measurements.

The main objective of this second experimental campaign was to check the wire stretching system, the effect of the voltage on the cleaning electrodes and to measure the upper limit of acceptable energy deposition on the detector. In parallel to the measurements, simulations for wire heating were done with the pyTT code, predicting the wire temperature at the various measurements.

The experiments were performed in the UNILAC Experimental Hall, at the X2 experimental Line. Table 8.1 summarizes the beam conditions used during this

experimental campaign. The beam current could be measured using a BCT placed upstream of the SEM grid and a faraday cup placed downstream of the grid. An independent measurement of the beam profile could also be measured by using a GSI SEM grid installed upstream of the beam pipe. The Proactive SEM grid was connected to the POLAND + CSA electronics. The data of the measurements could be visualized in real-time and they were also stored for offline analysis. Data storage of the other devices used during these measurements was not available, those measurements rely on the data taken on the fly.

8.3 Experimental Results

8.3.1 Bias Voltage Studies

This part of the measurements focused on testing the effects of the voltage on the diaman-shaped cleaning electrodes for different beam conditions. Following the formula introduced in 2, one can calculate the expected signal to be generated on the wires. Specifically this would be:

$$Q\left(\frac{e}{Ar^{10+}}\right) = 18\eta - 8\mu + 18SEY_p(2 - \eta + BS_p) + 8SEY_e(2 - \mu + BS_e) \quad (8.1)$$

The parameters necessary to complete this expression are summarized in table 8.2. Note that in this case, both η and μ are 1.0. This means that both the protons and the electrons of the Argon ion deposit their full charge in the material. The range of argon in Tungsten is $11.8 \mu m$, which is much smaller than the thickness of the wires ($100 \mu m$). The secondary emission yields and backscattering probabilities given in table 8.2 were calculated without considering any electric field.

η	μ	SEY_p	SEY_e	BS_p	BS_e	$Q(e/Ar)$
1.0	1.0	14.91	$8.608 \cdot 10^{-6}$	0.0	0.0	278.38

Table 8.2: Summary of parameters necessary for calculating charge generation in a wire(Tungsten, $\phi = 100 \mu m$) by a particle beam (Ar^{10+} ion at 8.6 MeV/uma). These parameters were calculated with Geant4.

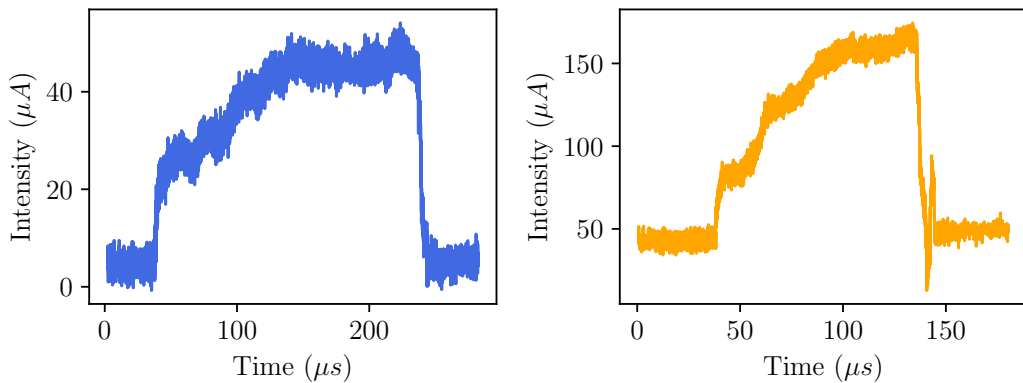


Figure 8.4: Intensity as a function of time, measured by the BCT, during one beam pulse. For two different beam conditions, $40 \mu s$ (left) and $150 \mu s$ (right).

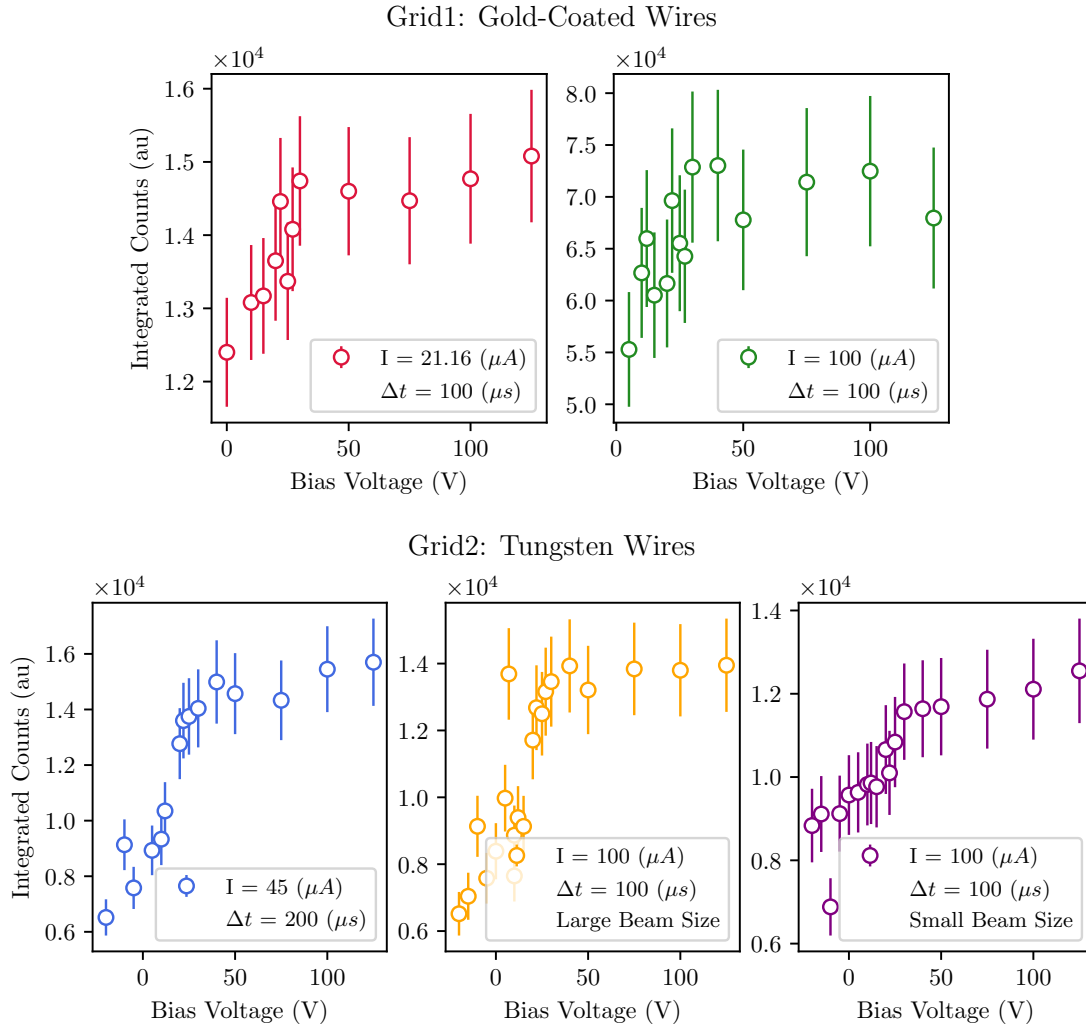


Figure 8.5: Integral of the signal registered by the SEM grids as a function of the applied bias voltage. Top figures: Gold-Coated Tungsten Wires. Bottom Figures: SEM grid with pure tungsten wires.

The electric field generated by the bias plates slightly affects these parameters. A sufficiently high positive voltage could slightly enhance the SEY. However, it is not straightforward to give a quantitative value of that change [102] [103]. The applied voltage also helps reduce the SE crosstalk. This means it will prevent SE emitted from one wire to deposit their charge in another wire. A clear positive signal will be generated in the wires due to their interaction with the Argon beam. We expect this signal to be enhanced when a positive bias is applied to the electrodes and to be reduced when a negative bias is applied to them.

A relative error of 10% was considered in all the points. This error is due to fluctuations in the beam intensity during the measurements. The intensity of the beam was not constant along the beam pulse, this can be observed in Fig. 8.4 where the intensity of the beam measured by the BCT is shown, for two different beam pulse lengths. Moreover, shot-by-shot intensity fluctuations were also observed.

Fig. 8.5 shows the measured integrated number of particles as a function of the bias current applied for different beam conditions. In all the different cases, we can observe how the total signal increases until reaching saturation for bias voltages

above ~ 40 V. For negative bias voltages the signal diminishes. This signal was also expected to saturate for negative values. However, this could not be observed during the measurements for the applied voltages.

8.3.2 Profile Measurement and Time Studies

The effects of the bias voltage can also be observed in the measurements of the transverse beam profile. Fig. 8.6 shows, for different bias voltages, the transverse profile of the beam. Lighter colors indicate larger bias voltages. With these measurements, we confirm our previous statement, higher bias voltages induce an overall higher signal along the wires. Compared to the previously installed SEM grids at GSI, the SEM grids manufactured by PROACTIVE provide a much larger resolution. A comparison between the measurements taken by the GSI grid and the PROACTIVE grid is shown in Fig. 8.7. Due to the differences in the data acquisition systems, to compare these measurements normalization of the intensity and an offset correction had to be applied.

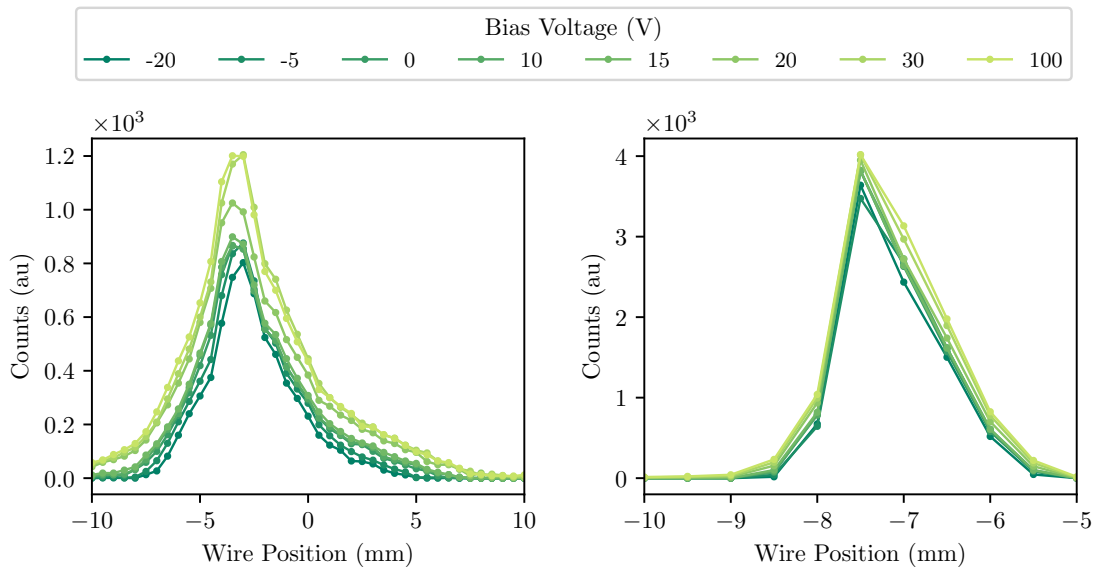


Figure 8.6: Effect of Bias voltage on transverse beam profile measurements. Both profiles were measured with Grid2. Left: $\Delta t = 200 \mu s$, $I = 45 \mu A$. Right: $\Delta t = 100 \mu s$, $I = 100 \mu A$.

In the case of the PROACTIVE grid, the POLAND+CSA electronics [100] allowed for measurements of the transverse beam profile as a function of time. The time resolution could be varied between 100 ns and 86 s per time slice. For these measurements, a time resolution of $5 \mu s$ per time slice was used. Fig. 8.8 shows a measurement of the beam profile as a function of time. This measurement was taken with Grid1, with an applied bias voltage of 100 V. In this figure, one can observe that the signal registered by each wire increases during the beam passage, it reaches a maximum at the end of the beam pulse. This effect is more clear when looking at the projection of Fig. 8.8 onto the time axis. This projection is shown in Fig. 8.9 along with the projections for two other beam conditions.

Fig. 8.9 shows the total number of counts, registered by the wires as a function of time. In this how the three signals increase until reaching a maximum and then

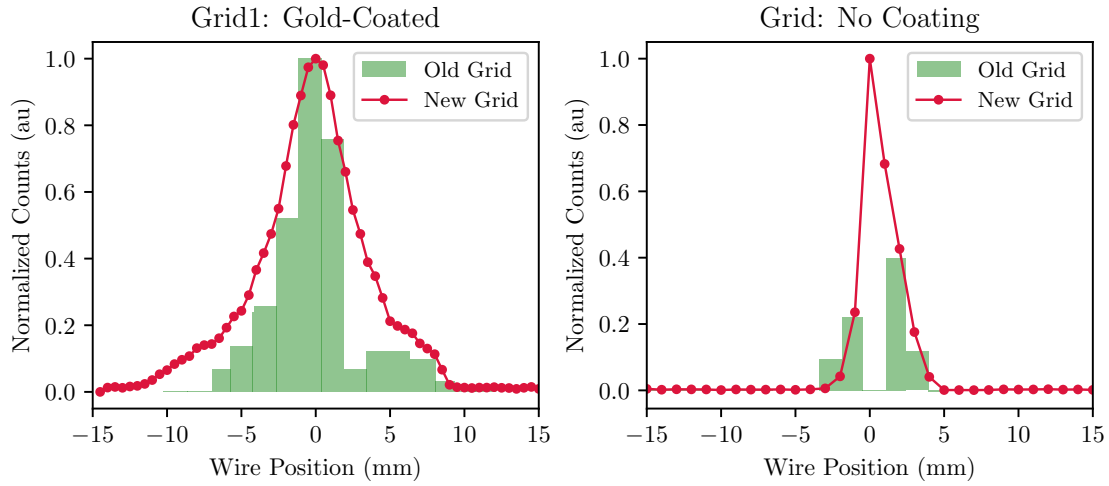


Figure 8.7: Comparison of transverse beam profile measured by GSI grid and PROACTIVE Grid. In both cases, $\Delta t = 100 \mu s$ and $I = 100 \mu A$. A bias voltage of 40 V was applied to the PROACTIVE grids.

decrease exponentially. The maximum of the curves gives us information on the beam pulse length. The time dependency of the $100 \mu s$ and $200 \mu s$ particle beam, shows a very clear agreement. The signal for the $100 \mu s$ particle beam shows a very linear increase whereas the $200 \mu s$ shows a slight logarithmical increase. This could suggest a possible signal saturation in the latter case. The big discrepancies on the $40 \mu s$ curve suggest that a different time slice resolution was used. However, no record of that number was available in the stored data.

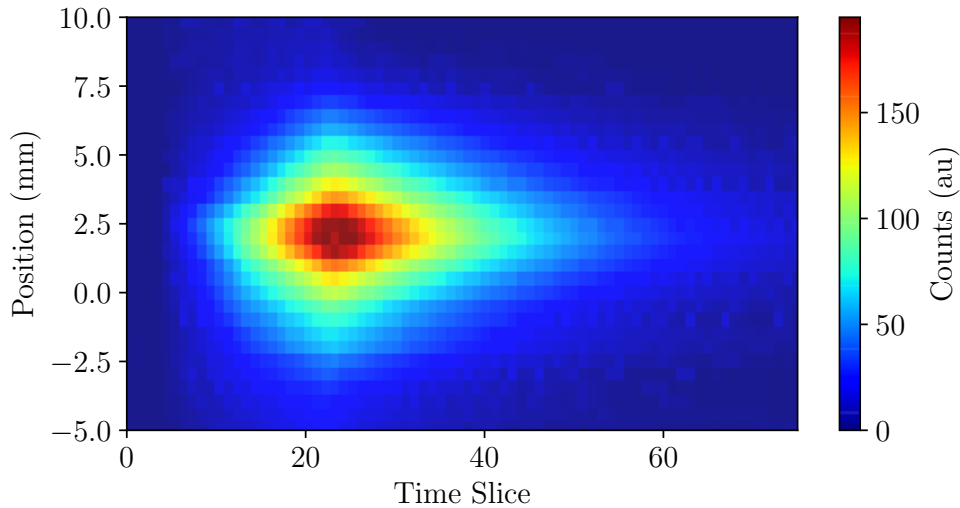


Figure 8.8: Time dependent transverse beam profile. Each time slice has a record of $5 \mu s$. The beam pulse length and intensity were $\Delta t = 100 \mu s$.

By default, the transverse beam profile was calculated using the total integral of the signal over time. However, one can also study the intra-pulse transverse beam profile evolution. To illustrate this we use a measurement taken by Grid 2, for a beam of $I = 100 \text{ mA}$ and $\Delta t = 100 \mu s$. Fig. 8.10 (Top) shows the transverse

beam profile measured at different instants of time. The highest intensity profile is registered at slice 22, which corresponded to the ending point of the beam pulse. The red curve shows the total integral of the signal as a function of time. For visualization purposes, this curve has been reduced by a factor 8.

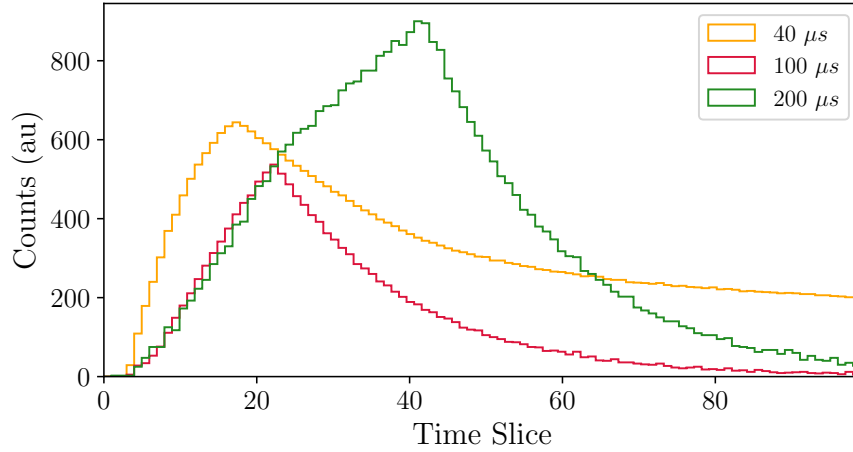


Figure 8.9: Integral of the total number of counts measured by all the grid wires as a function of time. For three different beam conditions. Measured with Grid1, bias voltage 100 V.

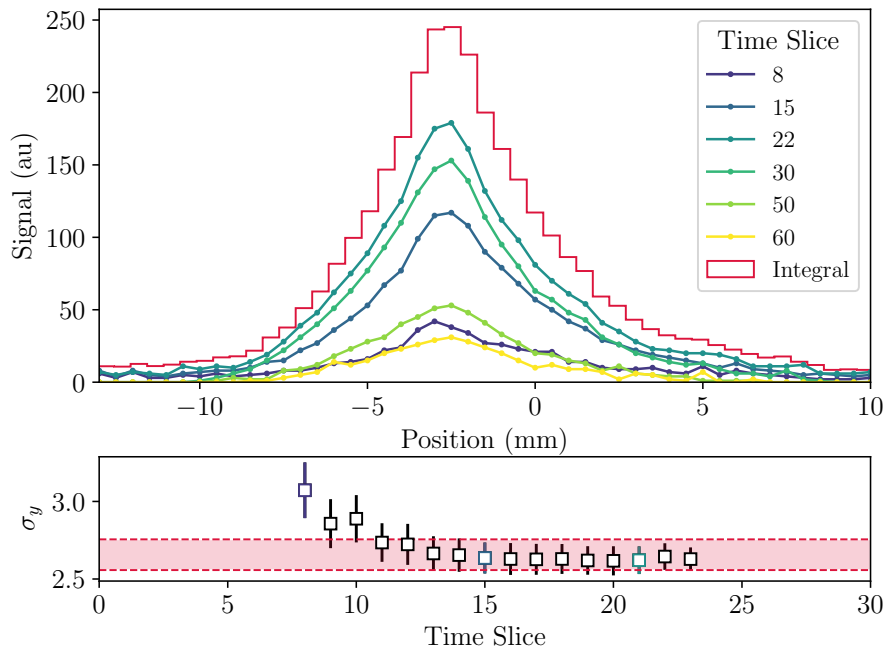


Figure 8.10: Top: Transverse beam profile at different instants of time. Each color represents a time slice. Each time slice has a record of $5 \mu s$. In red the total integral of the counts along the time is represented. Bottom: Vertical beam size as a function of time. Calculated by gaussian approximation of the beam to each time slice. In red, σ_y of the beam is calculated in the integral beam profile.

If one assumes a gaussian approximation, the σ of the beam can be obtained. Fig. 8.10 (bottom) shows the evolution of the fitted σ to the experimental data as a

function of time. The uncertainties in these values are solely due to the uncertainties in the parameter fitting. These results show that measured the σ of the beam is larger at an earlier time and then it stabilizes. This could be due to real intra-pulse beam size differences or simply because the registered signal is not strong enough for doing a proper Gaussian fitting. The fitted σ for the integral measurement (represented as a red stripe) matches very well the calculated values of the σ at the core of the beam pulse.

8.3.3 Thermal Studies

To prove the suitability of the SEM grids to the demanding conditions of the future pLinac, a systematic set of measurements was performed. Both grid prototypes were irradiated in the regular UNILAC 'grid protection mode', with a beam intensity of $I = 500\mu A$ and a beam pulse length of $40\mu s$. From this safe condition, the intensity of the beam was gradually increased while measurements of the beam profile were taken. In parallel to the measurements, simulations for wire heating were done with the pyTT code, predicting the wire temperature at the various beam conditions.

It is important to remember that the pyTT code is currently optimized for thin target detector measurements. This means the range of the incident particles is much larger than the thickness of the material, so the beam only deposits a small part of its energy in the detector and this energy deposition is constant along the detector length. In this case, the wires are thick compared to the range of 8.6 MeV/u Argon ions in tungsten (Wire thickness = $100\mu m$, particle range = $11.9\mu m$). This has two major consequences:

- We need to find an equivalent energy deposition as the program will consider a constant energy deposition along the detector. For these simulations, two extreme cases were considered. The energy deposition can be overestimated assuming the maximum energy is deposited along the whole length, or it can be underestimated assuming the maximum energy is spread along the whole length. The real value will lie in between this two. A more in-depth study should be performed if a more accurate value is needed.
- An extra contribution of conduction cooling is possible along the beam direction. This might make the simulated cooling slower than the real one. In reality, the thermal equilibrium might be reached earlier than predicted in the simulations.

Grid 1, Gold-Coated Tungsten Wires

An initial assessment of the beam size was performed with the upstream SEM grid, this measurement is shown in Fig. 8.11. A gaussian approximation of the beam yielded a beam size of $\sigma_x = 3.19(26)$ mm and $\sigma_y = 1.694(16)$ mm. In this case, we can observe a big difference between the maximum intensity registered by the horizontal (~ 3.80 au) and the vertical (~ 12.86 au) measurements. The particle distribution in the horizontal plane seemed to be more planar than gaussian. This might suggest that the density of particles in the horizontal plane was not as high as the one in the vertical plane.

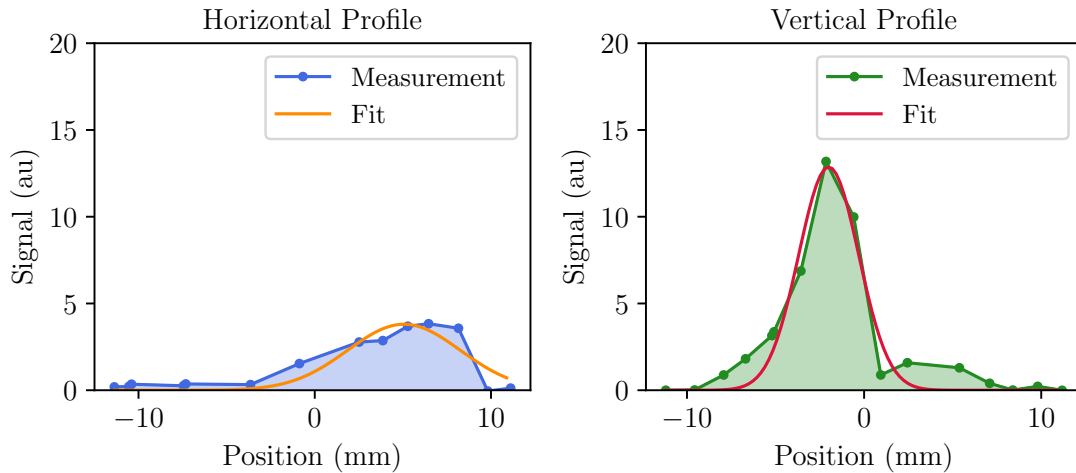


Figure 8.11: Beam profile measured with GSI SEM grid with, Gaussian fit for beam size determination.

The beam pulse length was kept constant at $40 \mu s$, with a repetition rate of 1 Hz. The beam intensity was gradually increased, from 0.5 - 1.5 mA. Fig. 8.12 (left) shows the simulated temperature evolution of the detector as a function of time. For three of these beam intensities. The figure on the right shows in more detail the predicted maximum temperature for the different beam intensities. The big uncertainties in the simulated results come from the uncertainties in the energy deposition in the detector material.

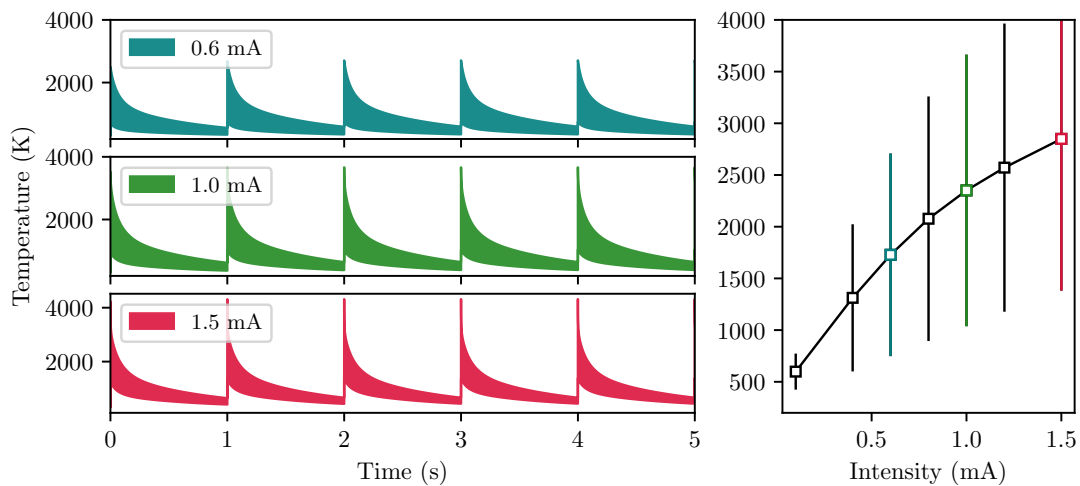


Figure 8.12: Left Plots: Evolution of the maximum temperature reached by a gold-coated tungsten wire for 5 beam shots. Right: Maximum temperature reached for different beam intensities.

These results predicted that the wire would be able to sustain all the applied beam intensities, although beam intensities larger than 1.5 mA approach dangerous territory. The melting point of gold is $\sim 1400K$. From the simulation results, we concluded that, for beam intensities ≥ 0.6 mA, the gold should have evaporated from the surface.

The beam profile was measured for four different beam intensities. The results of these measurements are shown in Fig. 8.13. Grid1 was able to measure the beam profile for all the given beam intensities without any problem. There are also no visual effects of wire heating (thermionic emission) or wire damage in the measurements. Indeed, after the measurements were performed the grid was extracted from the accelerator for a visual inspection. The SEM grid was intact, including the gold coating in the central wires.

This proves that the simulations were overestimating the beam heating in the wire. This overestimation might come from two factors: the gaussian approximation of the horizontal beam profile. And an overestimation in the energy deposition along the wire length.

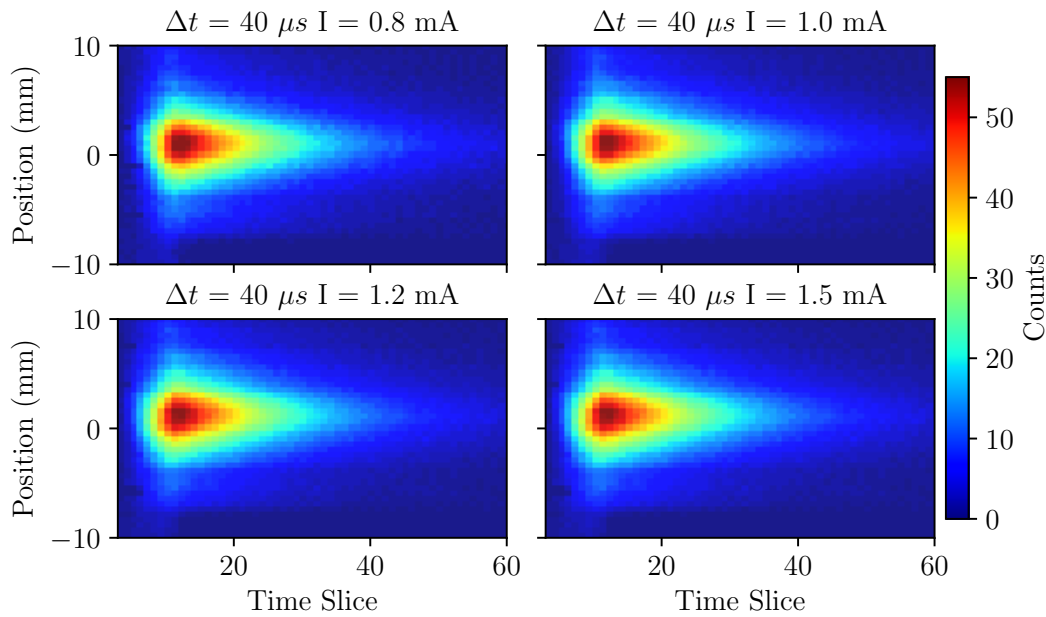


Figure 8.13: Signal measured by the different wires as a function of time. For four different beam intensities.

Grid 2, Pure Tungsten Wires

For testing the second grid, we made sure that Gaussian approximation of the beam was accurate for both the horizontal and the vertical planes. Fig. 8.14 shows the beam profile measured with the GSI grid for this second set of measurements. In this case, $\sigma_x = 2.052(37)$ mm and $\sigma_y = 1.587(91)$ mm. The beam pulse length was also $40 \mu s$ and the repetition rate was 1 Hz. The beam intensity varied from 0.5 - 1.5 mA.

The maximum temperature evolution as a function of time for different intensities is shown in Fig. 8.15. Due to the smaller beam size, the maximum predicted temperatures are larger than the ones predicted in the previous case. If the overestimation of the energy deposition is considered, the simulation predicted a wire breakage for beam intensities ≥ 0.6 mA. Even in the average case, the simulations predicted the wire would break in the case of 1.5 mA beam intensity.

Fig. 8.16 shows the experimental measurements of the beam profile for the different intensities. For a beam pulse length of $40 \mu s$ the grid seemed to resist the beam load very well, even for a 1.5 mA beam current. The simulations are

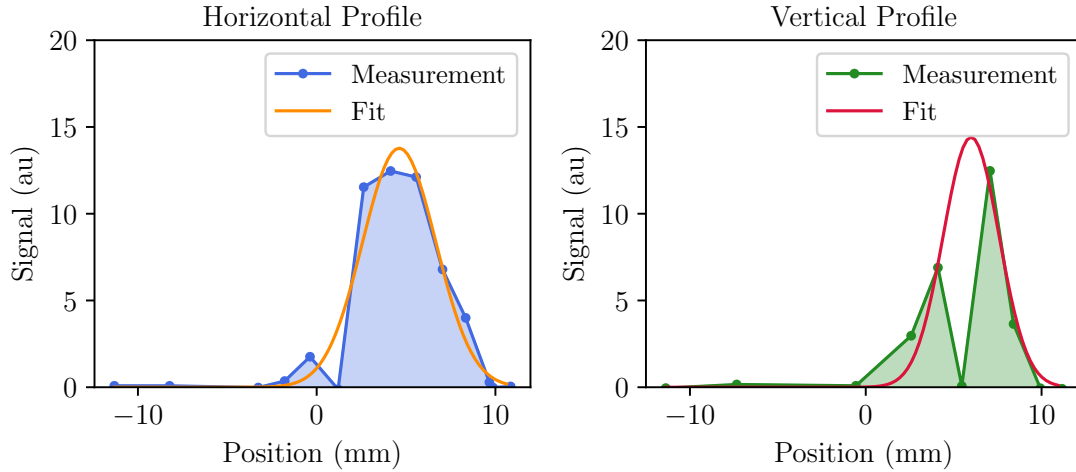


Figure 8.14: BeamProfile measured with GSI SEM grid for the second study with Gaussian fit for beam size determination.

again overestimating the wire’s maximum temperature. Because we really wanted to cross-check the power limit of the grid we went one step further and increased the beam pulse length to up $70 \mu s$. This increases the number of particles reaching the detector by a factor 1.7 (comparing it to the $\Delta t = 40 \mu s$ case).

Fig. 8.16 also shows the results of the measurements taken for this longer pulse, for three different instants of time. First, we can observe a wire current that extends much longer than the beam pulse length. This was followed by a wire breakage, which in this figure is represented by the lack of signal in the wire. A visual exploration of the grid after the experiment confirmed the wire was broken.

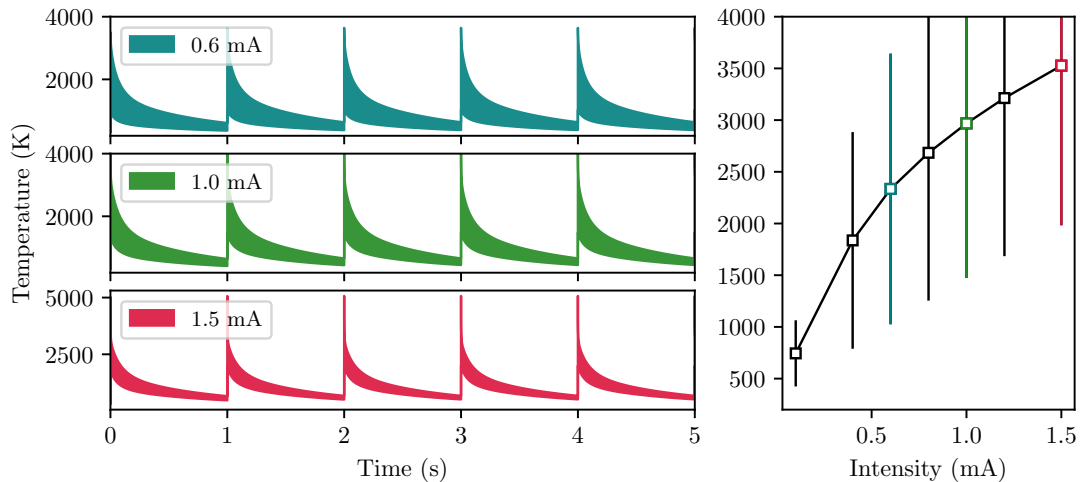


Figure 8.15: Left Plots: Evolution of the maximum temperature reached by a pure tungsten wire for 5 beam shots. Right: Maximum temperature reached for different beam intensities.

Fig. 8.17 shows a projection of the current, registered by different wires, as a function of time. When the beam pulse length was $\Delta t = 40 \mu s$, the expected time distribution is observed. The signal increases until the end of the beam pulse and then it decreases exponentially. For a $\Delta t = 70 \mu s$, the two wires that were

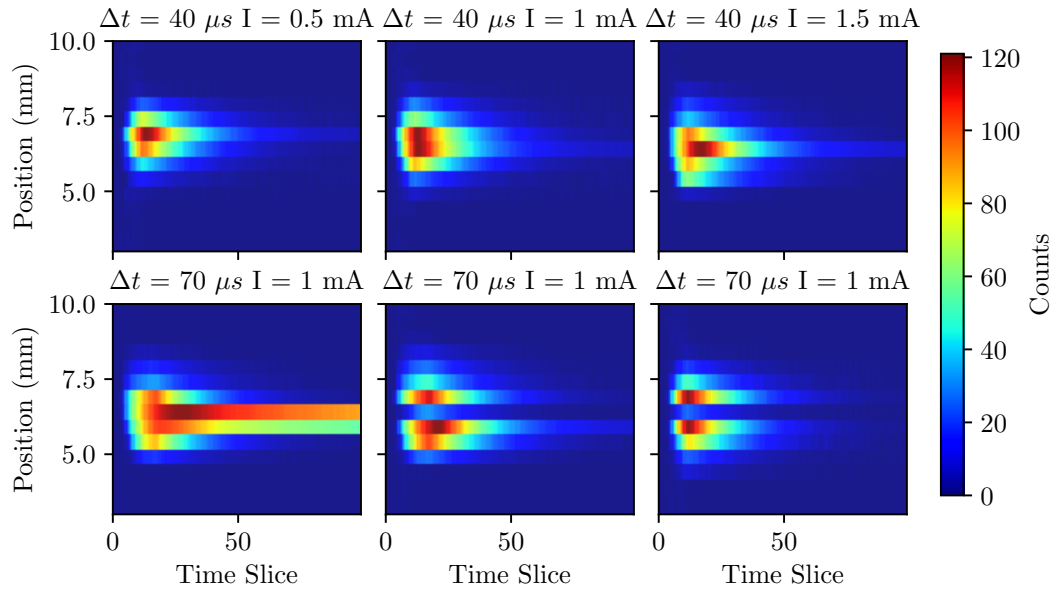


Figure 8.16: Fancy beam profile as time measurement for study 2

measuring the central part of the beam show a different time distribution. The signal increases until the end of the beam but it does not decrease exponentially. This could be explained by the presence of thermionic emission electrons. These thermionic electrons, because they are negative charges leaving the detector material, could affect the registered current, making it larger than it should for a small period of time.

The analysis performed at LINAC4 to obtain the temperature from the thermionic current measurement (Shown in Ch. 5, Sec. 5.1) could not be performed for these measurements. In this case, it is not straightforward to disentangle the current generated from thermionic emission from the one coming from the capacitive discharge.

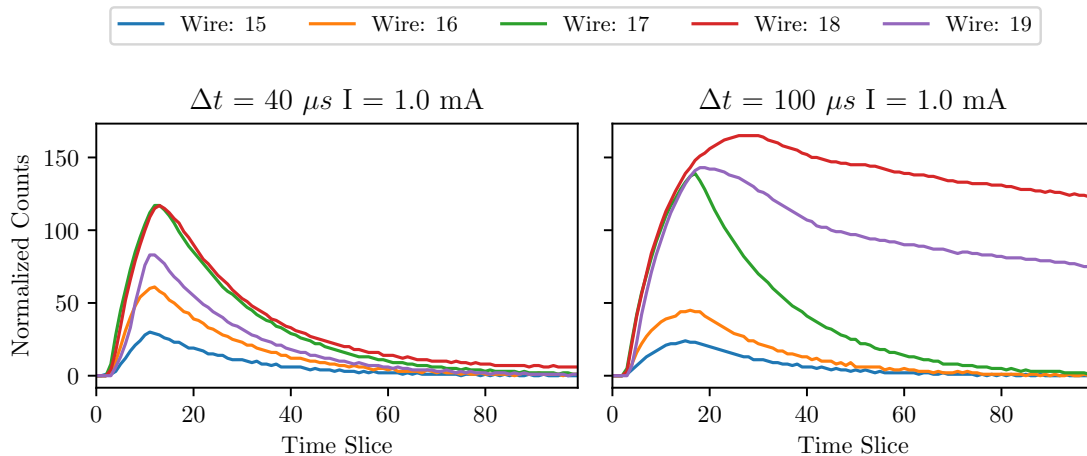


Figure 8.17: Current registered by the different wires in the pure tungsten grid as a function of time. For two different beam pulse lengths.

Conclusions

Beam diagnostics and instrumentation are essential constituents of any particle accelerator. Without adequate diagnostics, one would be blindly operating an accelerator and it would be impossible to assess problems and improve performance. In this work, we have mainly talked about thin target detectors like SEM grids, Wire Scanners and Foils. As was explained in Ch. 2, during measurements, the beam of particles deposits some energy in the detectors. Depending on the beam conditions, the thermal shock suffered by the detectors can be very severe. This might affect the measured currents (Thermionic Emission), or in some cases permanently damage the detectors. As could be seen from the examples in Ch. 4 with examples of the SPS and the LINAC4.

The main objective of this thesis was to implement a simulation tool to model the thermal evolution of thin target detectors. For a variety of beam conditions and detector materials. The research conducted by M. Sapinski in 2012 [49] served as a starting point for this work. He implemented a code to simulate the thermal evolution of fast wire scanners in the context of the SPS accelerator. For this thesis, we sought to extend that concept to also be able to simulate SEM grid detectors, and slow wire scanners and to include a 2D case to simulate thin foil detectors.

This required diving deeper into the formal aspects of the problem and understanding how this problem could be numerically solved in an efficient and easy-to-implement manner. To solve the non-linear PDE that expresses our heat equation, the theory of finite differences has been used. Three different schemes (FTCS, BTCS, Crank-Nicolson) have been implemented and can be used at the user's convenience. As detailedly explained in Sec. 4.6, it can currently simulate a variety of conditions. These include different types of particle beams, with different energies, intensities, pulse lengths, and particle types. It accepts different types of detectors with various materials and geometries. This has been implemented in a modular way to make it very simple to add new simulation conditions to the already existing ones.

The code needed to be accessible to a wide range of users without requiring them to be familiar with the programming or modeling complexities that lay beneath it. For that reason, a lot of effort was put into creating an intuitive and easy-to-use user-friendly interface. We have named the code PyTT. It is currently fully functional and ready to use. It is publically available at [60]. A summary of the models behind this code was already presented and published in IBIC 2020 [62]. A more detailed Journal outlining the project's current state is currently being written.

The thermal model relies on a big variety of parameters. A thorough investigation was conducted to determine how much the different parameters affected the simulation results (Sec. 4.7). On the one hand, we saw how uncertainties in the beam size significantly impacted the simulation results, especially for small beam sizes (< 1 mm). On the other hand, we saw how uncertainties in material prop-

erties highly affected the results. These properties can be found in the literature, and the uncertainty of such values is material-dependent. For Tungsten, we found that the emissivity property was the source of the highest uncertainty, reaching a 43.26% uncertainty. For Graphite, a much higher uncertainty of 22.71% was found in its thermal conductivity.

Once the PyTT code was implemented, we wanted to crosscheck that the results were a correct description of reality (Ch. 5). First, we made a comparison between the results obtained with the PyTT code and those obtained with Ansys, a highly used and benchmarked commercially available software. A LINAC4-like beam of particles was considered as the heating source and studies were performed for thin Tungsten wires and Graphite foils. From this study, we observed that the PyTT code was giving systematically higher maximum temperature results, showing a maximum discrepancy of 11.2% for a temperature of 1356 K. Ansys also presented a much faster cooling at higher temperatures and a slower cooling at lower temperatures. One big difference between both codes was the simulation time. PyTT averaged much shorter simulation times than Ansys. It was very difficult to properly understand the discrepancies between these two codes as the numerical methods employed by Ansys are not publicly available.

We also wanted to compare the thermal simulations with experimental measurements (Sec. 5.1). However, no dedicated setup could be installed in any of the CERN machines. The information available was the intensity registered by the SEM Grids and wire scanners along the LINAC4 accelerator. So we went ahead and used thermionic emission to indirectly measure the thermal evolution. Due to the close relationship between the thermionic current and the temperature, by comparing the simulated current and the experimentally measured one, we could judge the reliability of our thermal simulation results.

For the experimental planning, we selected the beam conditions that would yield a measurable thermionic current. We were restricted in our choice of detector and timing due to the potentially destructive nature of this experiment. During the experiment, the beam intensity was kept constant to 17.30(17) mA while the beam pulse length was systematically increased from 50 μs up to 450 μs . Two different beam size conditions were measured. Firstly, a larger beam ($\sigma_x = 1.02(5)$ mm and $\sigma_y = 1.76(2)$ mm) centered on the grid was measured. Although thermionic emission was not seen in this case, the moment when two wires were glued together could be measured quite clearly.

Secondly, a smaller beam of particles ($\sigma_x = 0.59(17)$ mm $\sigma_y = 3.23(54)$ mm) was measured. In this case, thermionic emission was observable in various wires for a pulse length of ~ 450 μs . This measurement was reproduced as close as possible with the PyTT code. The maximum relative error between simulated and measured results is found to be around 30 %, and it is found at the very end of the beam shot. Even then, the average relative error along the whole pulse is 6.3(25)%. A systematic study of the simulation uncertainties was performed for this experiment. Big uncertainties were found, mainly in the thermionic current regime. The biggest contributor to the simulation's uncertainty came from uncertainties in the beam size ($\xi_x = 28.81\%$).

PyTT has been already used for a variety of applications, both at CERN and in other facilities. These applications include beam power limit calculations for SEM grids and Wire Scanners at CERN LINAC4, fast wire scanners and thin foils

(BTVs) at CERN SPS and Hi-RadMat. It has also been used in other facilities such as DESY (Germany), ISIS (UK) and GSI (Germany) for SEM grid simulations. In this work, we only presented the beam power limits calculations at LINAC4, SPS (Ch. 5) and GSI (Ch. 8) as they were the most extensive and time-consuming studies performed.

In CERN, in particular, at LINAC4, SEM grid detectors are made of gold-coated tungsten wires. To obtain accurate results on the thermal limit calculations it was important to reduce the simulation uncertainties brought by the uncertainties in the Emissivity of Tungsten (Ch. 6). An experimental setup was designed and implemented to measure the total directional emissivity of thin wires. This was done using the calorimetric method. The two biggest challenges of this experiment were: Firstly, the implementation of a set of electronics to both control the wire heating and acquire the measured data. And secondly, the implementation of the data analysis tools and the numerical methods to extract the value of the emissivity from the measured data.

The emissivity of 40 μm Tungsten wires (both with gold-coating and without) was measured. The emissivity of the pure tungsten wires was, on average, larger than the emissivity of the gold-coated tungsten wires, ranging from 0.087(12) up to 0.176(21). The emissivity values for the gold-coated tungsten wires appear to be consistent with the reported values of the emissivity of gold. In the case of pure tungsten wires, the measured values agree with some published references. Particularly those reporting values of poor electromagnetic radiators. The average statistical relative error for the measured values was 15.21% in the case of pure tungsten wires and 26.26% for gold-coated tungsten wires. All these results were summarized and published in [67].

The main focus of this work has been on the thermal simulations and all their implications. However, there have also been other, more practical things done that are directly relevant to CERN operation. A thorough understanding of the signal production in SEM grids and Write scanners was crucial to assist in a range of tests carried out with these detectors, mainly in the LINAC4 context. An example of these measurements is the profile and current measurements for the LBE run presented in Sec. 3.3.

Another example of how this work was useful for CERN operation is presented in Ch. 7 with the calibration of the H^0H^- monitors. To inject the H^- beam of particles to the PSB a new CEI system was installed at CERN. An intensity measurement of both, the unstripped H^0 and H^- beam particles is required to allow an efficient injection setup, monitor the efficiency of the stripping foil and protect the dump in case of a high-intensity beam impact (by providing an interlock signal in case of stripping foil failure). The H^0H^- were installed and fully calibrated during the realization of this thesis.

This calibration implied understanding thoroughly the electronics, the acquisition system and the different signals available from these monitors. This calibration was performed by comparing the current measured the H^0H^- with the current measured by an independent BCT. This calibration had to be performed for all the current monitor plates, for all the rings and a variety of beam conditions. This process was challenging, time-consuming and it was done in collaboration with the ABT group. The calibration process yielded an absolute calibration factor of $1.560(33)\cdot 10^8$ Charges/ADC count. This value was slightly dependent on the beam pulse length

and number of turns, but this discrepancy was associated with mismatches in the BCT and H^0H^- measurements. Since this calibration took place, these monitors have been extensively used. They can measure stripping inefficiencies of $\sim 0.1\%$. The calibration process and results were summarised and published in [78].

In June 2022 a dedicated set of measurements were performed in GSI (Darmstadt, Germany) for the commissioning of two SEM grid prototypes, designed by PROACTIVE. All the knowledge gained during this thesis served to assist with the measurements. For this experiment, an Ar^{10+} beam of particles was used. With a beam energy of 8.6 MeV/u and a repetition rate of 1 Hz. We could confirm the improvement in the beam profile resolution measurable with the PROACTIVE grids and the correct functioning of the vias voltage. In parallel to the measurements, simulations for wire heating were done with the PyTT code, predicting the wire temperature at the various measurements. However, in this case, the thermal simulations were inconclusive due to the big uncertainties in the beam energy deposition. Part of these studies were published and presented in [92] and [93]. The studies on the thermal properties are still undergoing.

The types of detectors and operational principles covered in this work are nothing new. They have been extensively used in particle accelerators for decades but even nowadays, they are being used and installed in the most recent and cutting-edge machines in the world of accelerator physics. This research moves us one step closer to fully understanding these detectors, allowing us to fully exploit their potential. All the goals and objectives proposed for this thesis have been achieved. Additional research to the original planning was conducted to address the issues and difficulties that arose along the way.

Unfortunately, time is limited, and even if the objectives were covered, there are always some points that merit further investigation. For example, it would be interesting to compare the PyTT code results to a wider range of cases. Different beam conditions, energy ranges, different detector materials and machines. It would be of particular interest to crosscheck the PyTT simulations with Heavier Ions machines.

The emissivity measurement performed during this work, despite having a relatively straightforward setup, is very powerful and could be easily exploited further. Many more wire types could be measured. Wires of different materials, such as graphite wires (for measuring conductivity properties) or the currently popular carbon nanotube wires. As far as the H^0H^- monitors are concerned, they are currently fully operational and they are being used extensively. However, they are currently facing electronic interference problems. A lot of work is currently being done to solve this issue.

This work has brought us one step ahead in the good direction, and it will hopefully assist all the others who will follow in further exploring this long-standing but extremely challenging topic.

Bibliography

- [1] *Cern Official Website*. URL: <https://www.home.cern/>.
- [2] Cern Physics Program. URL: <https://home.cern/science/physics>.
- [3] *Cern Document Server*. URL: <https://cds.cern.ch/record/2684277>.
- [4] H Damerau et al. *LHC Injectors Upgrade, Technical Design Report*. 2014. DOI: [10.17181/CERN.7NHR.6HGC](https://doi.org/10.17181/CERN.7NHR.6HGC). URL: <https://cds.cern.ch/record/1976692>.
- [5] D.A. Fink et al. “ H^- extraction systems for CERN’s Linac4 H^- ion source”. In: *Nuclear Instruments and Methods in Physics Research Section A: Accelerators, Spectrometers, Detectors and Associated Equipment* 904 (2018), pp. 179–187. ISSN: 0168-9002. DOI: <https://doi.org/10.1016/j.nima.2018.07.046>. URL: <https://www.sciencedirect.com/science/article/pii/S0168900218308817>.
- [6] L Arnaudon et al. *Linac4 Technical Design Report*. Tech. rep. revised version submitted on 2006-12-14 09:00:40. Geneva: CERN, 2006. URL: <https://cds.cern.ch/record/1004186>.
- [7] M Hori and K Hanke. “Spatial and temporal profile monitor with nanosecond resolution for CERN’s Linac4”. In: *Journal of Instrumentation* 7.04 (Apr. 2012), pp. C04005–C04005. DOI: [10.1088/1748-0221/7/04/c04005](https://doi.org/10.1088/1748-0221/7/04/c04005). URL: <https://doi.org/10.1088/1748-0221/7/04/c04005>.
- [8] Helmut Wiedemann. *Particle accelerator physics*. Springer Nature, 2015.
- [9] Donald A Edwards and Michael J Syphers. *An introduction to the physics of high energy accelerators*. John Wiley & Sons, 2008.
- [10] WT Weng and SR Mane. “Fundamentals of particle beam dynamics and phase space”. In: *AIP Conference Proceedings*. Vol. 249. 1. American Institute of Physics. 1992, pp. 3–45.
- [11] George William Hill. “On the part of the motion of the lunar perigee which is a function of the mean motions of the sun and moon”. In: *Acta mathematica* 8.1 (1886), pp. 1–36.
- [12] Helmut Wiedemann. *Particle accelerator physics*. Springer Nature, 2015.
- [13] Y. Papaphilippou. *Transverse Motion*. Presented at US Particle Accelerator School. 2008. URL: <https://yannis.web.cern.ch/teaching/transverse.pdf>.
- [14] Jean Buon. *Beam phase space and emittance*. Tech. rep. Paris-11 Univ., 1992.
- [15] Elvin Harms Mike Syphers. *Fundamentals of Accelerator Physics and Technology*. Winter US Particle Accelerator School. 2018. URL: <https://uspas.fnal.gov/materials/180DU/Fund/index.html>.

- [16] Peter Strehl. *Beam instrumentation and diagnostics*. Vol. 120. Springer, 2006.
- [17] Peter Forck. “Beam Instrumentation and Diagnostics”. In: *arXiv preprint arXiv:2009.10411* (2020). URL: https://indico.cern.ch/event/569714/contributions/2303731/attachments/1415057/2166101/juas_script.pdf.
- [18] *Proceedings of the 2018 course on beam instrumentation for particle accelerators, Tuusula, Finland, 2–15 June 2018. CAS Beam Instrumentation, 2–15 June 2018, Tuusula, Finland*. CERN. Geneva: CERN, 2020. URL: <http://cds.cern.ch/record/2625174>.
- [19] Enrico Bravin. *Transverse Beam Profiles*. Tech. rep. 37 pages, 53 figures. May 2020. arXiv: 2005.07400. URL: <http://cds.cern.ch/record/2723980>.
- [20] Glenn F Knoll. *Radiation detection and measurement*. John Wiley & Sons, 2010.
- [21] Robley Duglison Evans and RD Evans. *The atomic nucleus*. Vol. 582. McGraw-Hill New York, 1955.
- [22] Stefaan Tavernier. *Experimental techniques in nuclear and particle physics*. Springer Nature, 2010.
- [23] Simon Eidelman et al. “Review of particle physics”. In: *Physics letters B* 592.1-4 (2004), pp. 1–5.
- [24] International Commission on Radiation Units and Measurements. “Stopping powers and ranges for protons and alpha particles”. In: 26.ICRU–49 (1993).
- [25] Prof. Teresa Montaruli. *High Energy Astrophysics Lectures*. Physics 801: Instrumentations and Methods in Astroparticle Physics. URL: https://user-web.icecube.wisc.edu/~tmontaruli/801/Exercise4_801.pdf.
- [26] NIST. *National Institute of Standards and Technology*. Physical Meas. Laboratory. URL: <https://www.nist.gov/>.
- [27] RM Sternheimer et al. “Density effect for the ionization loss of charged particles in various substances”. In: *Atomic Data and Nuclear Data Tables* 30.2 (1984), pp. 261–271.
- [28] Donald E Groom and SR Klein. “Passage of particles through matter”. In: *The European Physical Journal C-Particles and Fields* 15.1 (2000), pp. 163–173.
- [29] Martin J Berger and Stephen M Seltzer. *Tables of energy losses and ranges of electrons and positrons*. Tech. rep. 1964.
- [30] Geant4 Tutorial. *Bremsstrahlung*. 2006. URL: <https://lappweb.in2p3.fr/~maire/tutorials/bremsstrahlung.pdf>.
- [31] EA Kuraev et al. “Coulomb correction to the screening angle of the Moliere multiple scattering theory”. In: (2012).
- [32] Saunderson Goudsmit and JL Saunderson. “Multiple scattering of electrons”. In: *Physical review* 57.1 (1940), p. 24.
- [33] Virgil L Highland. “Some practical remarks on multiple scattering”. In: *Nuclear Instruments and Methods* 129.2 (1975), pp. 497–499.

- [34] Roger F Dashen. “Theory of electron backscattering”. In: *Physical Review* 134.4A (1964), A1025.
- [35] Ervin B Podgoršak et al. *Radiation physics for medical physicists*. Vol. 1. Springer, 2006.
- [36] Yung-Su Tsai. “Pair production and bremsstrahlung of charged leptons”. In: *Reviews of Modern Physics* 46.4 (1974), p. 815.
- [37] L Austin and H Starke. “Ueber die Reflexion der Kathodenstrahlen und eine damit verbundene neue Erscheinung secundärer Emission”. In: *Annalen der Physik* 314.10 (1902), pp. 271–292.
- [38] C Bouchard and JD Carette. “The surface potential barrier in secondary emission from semiconductors”. In: *Surface Science* 100.1 (1980), pp. 251–268.
- [39] W Doliński et al. “Angular Distributions of Secondary Electrons Emitted from the Polycrystalline Silver”. In: *Acta Physica Polonica A* 81.2 (1992), pp. 211–222.
- [40] D Hasselkamp et al. “Ion-induced secondary electron spectra from clean metal surfaces”. In: *Nuclear Instruments and Methods in Physics Research B* 18.1 (1986), pp. 561–565.
- [41] Li HM et al. “On the energy distribution of secondary electrons emitted from metals”. In: *Journal of Surface Analysis* 15.2 (2008), pp. 186–194.
- [42] EJ Sternglass. “Theory of secondary electron emission by high-speed ions”. In: *Physical Review* 108.1 (1957), p. 1.
- [43] R.E. Kirby and F.K. King. “Secondary electron emission yields from PEP-II accelerator materials”. In: *Nuclear Instruments and Methods in Physics Research Section A: Accelerators, Spectrometers, Detectors and Associated Equipment* 469.1 (2001), pp. 1–12. ISSN: 0168-9002. DOI: [https://doi.org/10.1016/S0168-9002\(01\)00704-5](https://doi.org/10.1016/S0168-9002(01)00704-5).
- [44] EJ Sternglass. “Theory of secondary electron emission by high-speed ions”. In: *Physical Review* 108.1 (1957), p. 1.
- [45] Bruno Rossi. “High-energy particles”. In: (1952).
- [46] OW Richardson. *(Thermionic) Emission From Hot Bodies*. Watchmaker Publishing, 2003.
- [47] *Geant4 Official Website*, URL: <https://geant4.web.cern.ch/>.
- [48] et. al. A. Navarro. *First results of transverse profile measurements from the LBE run*. LIU Beam Dynamics Coordination meeting. 2019. URL: <https://indico.cern.ch/event/835600/>.
- [49] M Sapinski. “Beam interaction with thin materials: heat deposition, cooling phenomena and damage limits”. In: *Conf. Proc.* Vol. 1204151. CERN-ATS-2012-155. 2012, WECP04.
- [50] Federico Roncarolo et al. “Cavity mode related wire breaking of the SPS wire scanners and loss measurements of wire materials”. In: *Proceedings of the 2003 Particle Accelerator Conference*. Vol. 4. IEEE. 2003, pp. 2470–2472.

- [51] Ephraim M Sparrow and Robert D Cess. *Radiation Heat Transfer: Augmented Edition*. Routledge, 2018.
- [52] BC Lough et al. “Numerical calculation of thermionic cooling efficiency in a double-barrier semiconductor heterostructure”. In: *Physica E: Low-dimensional Systems and Nanostructures* 11.2-3 (2001), pp. 287–291.
- [53] *Heat of Sublimation*. 2021. URL: <https://chem.libretexts.org/@go/page/1939>.
- [54] Upper Limits For and In Gasses. *MUC-0186 Upper Limits for Sublimation Losses from Hot Carbon Targets in Vacuum*. URL: <https://citeseerx.ist.psu.edu/viewdoc/summary?doi=10.1.1.2.9715>.
- [55] Arieh Iserles. *A first course in the numerical analysis of differential equations*. 44. Cambridge university press, 2009.
- [56] Randall J LeVeque. *Finite difference methods for ordinary and partial differential equations: steady-state and time-dependent problems*. SIAM, 2007.
- [57] Keith W Morton and David Francis Mayers. *Numerical solution of partial differential equations: an introduction*. Cambridge university press, 2005.
- [58] Robert E Funderlic. “Scientific Computing: An Introduction with Parallel Computing”. In: *American Scientist* 82.4 (1994), pp. 390–391.
- [59] A. Meseguer. *Fundamentals of Numerical Mathematics for Physicists and Engineers*. Wiley, 2020. ISBN: 9781119425670. URL: <https://books.google.ch/books?id=9JbiDwAAQBAJ>.
- [60] A. Navarro. *PyTT*. Git Hub. URL: <https://github.com/navarrof/PyTT.git>.
- [61] Y.S. Touloukian et al. *Thermophysical Properties of Matter - The TPRC Data Series. Volume 3. Thermal Conductivity - Nonmetallic Liquids and Gases*. Defense Technical Information Center, 1970.
- [62] Araceli Navarro Fernandez et al. “Development of a Thermal Response Model for Wire Grid Profile Monitors and Benchmarking to CERN LINAC4 Experiments”. In: (2020), TUPP35. 4 p. DOI: [10.18429/JACoW-IBIC2020-TUPP35](https://doi.org/10.18429/JACoW-IBIC2020-TUPP35).
- [63] A. Bhatia. “Principles and Methods of Temperature Measurement”. In: *Continuing Education and Development, Inc.* Course No: E02-012 (). URL: <https://www.cedengineering.com/userfiles/Principles%20and%20Methods%20of%20Temperature%20Measurement-R1.pdf>.
- [64] ANSYS Engineering Analysis System. URL: <https://www.ansys.com/>.
- [65] ANSYS Mechanical. *APDL Command Reference ANSYS*. Inc. Southpointe 2600 ANSYS Drive Canonsburg.
- [66] Jose Luis Sirvent Blasco. “Beam secondary shower acquisition design for the CERN high accuracy wire scanner”. In: (2019).
- [67] F. Roncarolo A. Navarro M. Martin. “Experimental investigation of Gold Coated Tungsten Wires emissivity for applications in particle accelerators.” In: *IBIC 2022* (2022).

- [68] Gustav Kirchhoff. “I. On the relation between the radiating and absorbing powers of different bodies for light and heat”. In: *The London, Edinburgh, and Dublin Philosophical Magazine and Journal of Science* 20.130 (1860), pp. 1–21.
- [69] Max Planck. “The theory of heat radiation”. In: *Entropie* 144.190 (1900), p. 164.
- [70] M Honner and P Honnerová. “Survey of emissivity measurement by radiometric methods”. In: *Applied Optics* 54.4 (2015), pp. 669–683.
- [71] Chengxi Zhu et al. “An accurate instrument for emissivity measurements by direct and indirect methods”. In: *Measurement Science and Technology* 31.4 (2020), p. 044007.
- [72] Tomas Kralik et al. “Method for measurement of emissivity and absorptivity of highly reflective surfaces from 20 K to room temperatures”. In: *Metrologia* 53.2 (2016), p. 743.
- [73] Irina Vishnevetsky et al. “Method for accurate measurement of infrared emissivity for opaque low-reflectance materials”. In: *Applied Optics* 58.17 (2019), pp. 4599–4609.
- [74] David R Lide. *CRC handbook of chemistry and physics*. Vol. 85. CRC press, 2004.
- [75] Charles De Izarra and Jean-Michel Gitton. “Calibration and temperature profile of a tungsten filament lamp”. In: *European Journal of Physics* 31.4 (2010), p. 933.
- [76] Rad Sadri et al. “A facile, bio-based, novel approach for synthesis of covalently functionalized graphene nanoplatelet nano-coolants toward improved thermo-physical and heat transfer properties”. In: *Journal of colloid and interface science* 509 (2018), pp. 140–152.
- [77] Matthias Weil and Wolf-Dieter Schubert. “The beautiful colours of tungsten oxides”. In: *International Tungsten Industry Association: London, UK* (2013), pp. 1–9.
- [78] Araceli Navarro Fernandez et al. “PSB H^0H^- Monitor Calibration and Commissioning. PSB H0 - H^- MONITOR CALIBRATION AND COMMISSIONING”. In: *JACoW IBIC 2021* (2021), 429–433. 5 p. DOI: [10.18429/JACoW-IBIC2021-WEPP24](https://doi.org/10.18429/JACoW-IBIC2021-WEPP24).
- [79] *High Luminosity LHC Project*. URL: <https://hilumilhc.web.cern.ch>.
- [80] Julie Coupard et al. *LHC Injectors Upgrade, Technical Design Report*. Tech. rep. 2016.
- [81] Karlheinz Schindl. “Space charge”. In: (2006). DOI: [10.5170/CERN-2006-002.305](https://doi.org/10.5170/CERN-2006-002.305). URL: <https://cds.cern.ch/record/941316>.
- [82] Vadim Georgievich Dudnikov. “Charge exchange injection into accelerators and storage rings”. In: *Physics-Uspekhi* 62.4 (2019), p. 405.
- [83] WT Weng and SR Mane. “Fundamentals of particle beam dynamics and phase space”. In: *AIP Conference Proceedings*. Vol. 249. 1. American Institute of Physics. 1992, pp. 3–45.

- [84] J Borburgh et al. “Septa and Distributor Developments for H- Injection into the Booster from LINAC4”. In: (2008), 4 p. URL: <https://cds.cern.ch/record/1123691>.
- [85] Bruno Balhan et al. “Design and Construction of the CERN PS Booster Charge Exchange Injection Chicane Bumpers”. In: (2018), WEPMF082. 3 p. DOI: [10.18429/JACoW-IPAC2018-WEPMF082](https://cds.cern.ch/record/2663368). URL: <https://cds.cern.ch/record/2663368>.
- [86] Luis Feliciano et al. “A New Hardware Design for PSB Kicker Magnets (KSW) for the 35 mm Transverse Painting in the Horizontal Plane”. In: (2015), THPF086. 3 p. URL: <https://cds.cern.ch/record/2141898>.
- [87] CAS - CERN Accelerator School: Beam Injection, Extraction and Transfer: Erice, Italy 10 - 19 Mar 2017. CAS - CERN Accelerator School: Beam Injection, Extraction and Transfer. CERN. Geneva: CERN, 2018. DOI: [10.23730/CYRSP-2018-005](https://cds.cern.ch/record/2646489). URL: <https://cds.cern.ch/record/2646489>.
- [88] Sigrid Wagner. “LHC Machine Protection System: Method for Balancing Machine Safety and Beam Availability”. Presented 2010. 2010. URL: <https://cds.cern.ch/record/1349317>.
- [89] Victor Smaluk et al. “Combined effect of chromaticity and feedback on transverse head-tail instability”. In: *Physical Review Accelerators and Beams* 24.5 (2021), p. 054401.
- [90] Altium Designer. “How Do Ferrite Beads Work and How Do You Choose the Right One?” In: (2022). URL: <https://resources.altium.com/p/how-do-ferrite-beads-work-and-how-do-you-choose-right-one>.
- [91] Proactive R and D. URL: <https://proactiverd.com/>.
- [92] Thomas Sieber et al. “Design and Test of Beam diagnostics equipment for the FAIR proton LINAC.” In: *LINAC 2022 Proceedings* ().
- [93] Juan Herranz et al. “Secondary electron emission (SEM) grid for the FAIR Proton LINAC”. In: *IBIC 2022, Krakow, Poland* ().
- [94] GSI Helmholtzzentrum für Schwerionenforschung. URL: https://www.gsi.de/en/researchaccelerators/research_an_overview.
- [95] Manuel Heilmann et al. “FINAL DESIGN OF THE FOS ALVAREZ-CAVITY FOR THE UPGRADED UNILAC”. In: 2018.
- [96] O.K. Kester. “Status of the FAIR facility”. In: *Proceedings IPAC 2013, Shanghai China* 1085-1089.TUXB101 (May 2013).
- [97] Maksym Miski-Oglu et al. “Beam Commissioning of the Demonstrator Setup for the Superconducting Continuous Wave HIM/GSI-Linac”. In: (2019). Ed. by Mark Boland et al., MOZZPLM1. DOI: [10.18429/JACoW-IPAC2019-MOZZPLM1](https://cds.cern.ch/record/2646489).
- [98] Ulrich Ratzinger et al. “A 70-MeV Proton Linac for the FAIR Facility Based on CH - Cavities”. In: 2006.
- [99] Thomas Sieber et al. “Beam Diagnostics Layout for the FAIR Proton Linac”. In: *27th International Linear Accelerator Conference*. 2014, THPP063.

- [100] M. Witthaus. “SEM-GRID Prototype Electronics using Charge-Frequency-Converters”. In: *Proceedings DIPAC 2011, Hamburg, Germany* MOPD55 ().
- [101] Thomas Sieber et al. “Beam Diagnostics for Commissioning and Operation of the FAIR Proton Linac”. In: *JACoW IPAC2021* (2021), MOPAB315. DOI: [10.18429/JACoW-IPAC2021-MOPAB315](https://doi.org/10.18429/JACoW-IPAC2021-MOPAB315).
- [102] J. R. Dennison. “Evolution of the Electron Yield Curves of Insulators as a Function of Impinging Electron Fluence and Energy”. In: *IEEE Transactions on Plasma Science* 34.5 (2006).
- [103] A Shih et al. “Secondary electron emission studies”. In: *Applied surface science* 111 (1997), pp. 251–258.